



UNIVERSITÀ  
DEGLI STUDI  
DI PADOVA

UNIVERSITÉ DE LIÈGE – UNIVERSITÀ DEGLI STUDI DI PADOVA

Faculté des Sciences Appliquées – Dipartimento di Ingegneria Industriale DII

Tesi di Laurea Magistrale in Ingegneria dei Materiali

# FABRICATION AND CHARACTERIZATION OF LOW-ALLOYED TOOL STEEL OBTAINED BY SELECTIVE LASER MELTING

*Relatrici : Prof.ssa Anne Mertens (Université de Liège)*

*Prof.ssa Irene Calliari (Università di Padova)*

***Laureanda: ELENA FILIPPI***

Anno accademico: 2021/2022



# ***ABSTRACT***

## *English version*

The present work explores the capability of fabricating low-alloyed metal parts through the layer-by-layer Selective Laser Melting (SLM) technique. The alloy used was AISI S2, which is a carbide-free tool steel made of 0,49%wt of Carbon. Such kind of steels are not popular as for Additive Manufacturing process due to their unpromising welding properties. However, obtained results demonstrated the feasibility of printing fully dense, defects-free with good surface quality low-alloy steels. A process map containing the optimum set of parameters for the realisation of the S2 metal parts will be presented. Later, the printed pieces were subject to microstructural investigation under their as-build and heat-treated conditions. The outcomes showed a epitaxial grain growth strongly influenced by the scan strategy. Moreover, the outermost top layer consisted of supersaturated martensite which was characterized in order to gain information about the prior microstructure which was present. Whereas the rest of the cross-sections of the as-built samples were found to have bands of tempered martensite at various degrees of tempering. The cause was related to the complex thermal history of the SLM process. In order to achieve all the results several unique techniques have been used such as reverse Differential Thermal Analysis, post-processing heat treatment and nanoindentation. The latter were used in less common ways to obtain a deeper knowledge of the microstructure of S2 metal parts printed through SLM technique, showing promising results.

## *French version*

Le travail présenté explore la possibilité de fabriquer des pièces métalliques faiblement alliées en utilisant la technique d'impression 3D "Selective Laser Melting" (SLM) couche par couche. L'alliage utilisé est l'AISI S2, un acier à outils sans carbure composé de 0,49% en poids masse de carbone. Ce type d'acier n'est pas populaire pour le processus de fabrication additive en raison de ses propriétés de soudabilité peu prometteuses. Cependant, les résultats obtenus ont démontré la possibilité d'imprimer efficacement des aciers faiblement alliés entièrement denses, sans défauts et avec une bonne qualité de surface. Une carte de processus contenant l'ensemble des paramètres optimaux pour la production de pièces métalliques de S2 sera présentée. Par la suite, les pièces imprimées ont été soumises à une étude microstructurale de la microstructure dans leurs conditions de fabrication et de post-traitement thermique. Les résultats sur la section transversale ont montré une croissance épitaxiale des grains fortement influencée par la stratégie de balayage d'impression. De plus, il a été constaté que la couche supérieure la plus externe était constituée de martensite sursaturée, qui a été

caractérisée afin d'obtenir des informations sur la microstructure antérieure qui était présente. Tandis que le reste des sections transversales des échantillons tels qu'ils ont été construits imprimés présentait des bandes de martensite trempée à différents degrés de trempe. La cause de ce phénomène a été attribuée à l'histoire thermique complexe du processus SLM. Afin d'obtenir tous ces résultats, plusieurs techniques uniques ont été utilisées, comme l'analyse thermique différentielle inverse, le traitement thermique post-processing et la nanoindentation. Ces dernières ont été utilisées de manière moins courante pour obtenir une connaissance plus approfondie de la microstructure des pièces métalliques S2 imprimées par la technique SLM, montrant des résultats prometteurs.

#### *Italian version*

Il lavoro presentato indaga la capacità di fabbricare parti metalliche basso legate attraverso la tecnica di stampa 3D “Selective Laser Melting” (SLM) strato per strato. La lega utilizzata è AISI S2, un acciaio per utensili privo di carburi e con il 0,49% in peso di carbonio. Questo tipo di acciai non è molto diffuso tra i processi di fabbricazione additiva a causa delle loro poco promettenti proprietà di saldabilità. Tuttavia, i risultati ottenuti hanno dimostrato la possibilità di stampare efficientemente acciai basso-legati completamente densi, privi di difetti e con una buona qualità superficiale. Verrà presentata una mappa del processo contenente l'insieme dei parametri ottimali per la realizzazione delle parti in metallo S2. Successivamente, i pezzi stampati sono stati sottoposti a un'indagine microstrutturale sia nelle condizioni di costruzione sia in quelle di post-trattamento termico. I risultati sulla sezione trasversale hanno mostrato una crescita epitassiale dei grani fortemente influenzata dalla strategia di scansione utilizzata. Inoltre, è stato riscontrato che lo strato superiore più esterno era costituito da martensite super satura, che è stata successivamente caratterizzata per ottenere informazioni sulla microstruttura primordiale presente. Per quanto concerne la restante parte delle sezioni trasversali dei campioni stampati, sono state rilevate bande di martensite temprata a vari gradi di tempra. La causa di questo fenomeno è stata ricollegata alla complessa storia termica del processo SLM. Per ottenere tutti i risultati sono state utilizzate diverse tecniche uniche nel loro genere, come l'analisi termica differenziale inversa, il trattamento termico post-lavorazione e la nanoindentazione. Queste ultime sono state utilizzate in modi poco comuni per ottenere una conoscenza più approfondita della microstruttura delle parti in metallo S2 stampate con la tecnica SLM, mostrando risultati promettenti.

# ***ACKNOWLEDGMENTS***

First of all, my acknowledgements go to Prof. Anne Mertens and Dr. Jérôme Tchoufang Tchuindjang for supervising my work and for advising me while writing my thesis. I would also thank Prof. Irene Calliari for giving me the opportunity to reach this Erasmus destination and to the University of Liège for welcoming me from the very first day.

I am grateful to all the team of the MMS (Metallic Material Science) department: Rosine Pirson, Olivier Dedry, Jocelyn Delahaye, Herrim Seidou and Sylvie Salieri. I have felt as part of the teams since the beginning, thank you for all the kindness and patience for my broken French. In particular, a special acknowledge is addressed to Enrico Saggionetto for supervising all the steps of my work, for guiding me every day and most of all for passing me through his passion for his job.

I am infinitely thankful to my family, mamma, papà e Simone, for their support and for their continuous belief in me, not only in the last months but throughout all my life path. Since I was a child you showed me how to follow the bigger vision while having always my feet on the ground. You taught me the importance of appreciating everything I was given to and how to never give up because every effort will one day come back to me. Thanks to my zii and cugine as well for their support, for being always ready to remind me how to enjoy life at its fullest and to be there for any kind of need.

A huge thanks goes to my best friends Anna, Anna, Matilde and Vittoria who had taken my hand through every small step of my life, giving me the strength to undertake any new challenge. You have always been there for an advice, for a chat, for some singing or dancing and most important for very big laughs. Thanks to all my friends from the metropole of Montebelluna for never failing making me feel as welcomed back home. A big thanks to my friends from Padua as well who have stood by me after each one of my breakdowns during the exams and who made me enjoy even the most boring classes. Thanks also to Abi who has been not only my flatmate and personal animal-catcher but my companion during all the early morning rides with the beloved 48 to Sart-Tilman and in all the challenges of completing our thesis projects.

Thanks to my friends and flatmates all around the world with whom I shared the most unforgettable experiences starting from the ricottine and the biblio-mensa team. Thank you Liège and Aveiro for being my second homes now.

Above all I would like to thank the Erasmus program which has brought me in contact

with the greatest people. It has made me discover cultures, languages, individual stories and has made me go through so many different priceless experiences and challenges that have shaped who I am now. And for this I can only be beyond grateful.

# TABLE OF CONTENTS

1. INTRODUCTION .....	1
2. STATE OF THE ART .....	3
2.1 Additive Manufacturing (AM).....	3
2.1.1 Selective Laser Melting .....	6
2.2.1.1 Process mechanism .....	8
2.2.1.2 Influence of process parameters and defects .....	10
2.2.1.3 Post-processing Thermal Treatments .....	16
2.2 Materials involved in AM processes .....	19
2.2.1 Low-alloy Steel .....	22
2.3 Microstructural characterization.....	23
3. MATERIALS AND EXPERIMENTAL METHODS.....	29
3.1 Original Powders .....	29
3.2 Samples fabrication .....	29
3.2.1 SLM Machine.....	29
3.2.2 Parameters for the realization of the samples.....	31
3.3 Microstructural Characterization .....	33
3.3.1 Samples preparation .....	33
3.3.2 Optical Microscope (OM) and Stream Analysis Software .....	35
3.3.3 Scanning Electron Microscope (SEM) .....	36
3.4 Profilometer Analysis.....	38
3.5 Thermo-Physical Analysis .....	38
3.5.1 Density Measurements with the Pycnometer .....	38
3.5.2 Differential thermal Analysis (DTA).....	39
3.6 Hardness Tests.....	41
3.6.1 Macrohardness Test.....	41
3.6.2 Nanohardness Test .....	42
4. RESULTS .....	44
4.1 Pycnometer density evaluation .....	44
4.2 Surface Characterization .....	45
4.3 Cross-section overviews.....	48
4.3.1 Internal Defects Analysis.....	51
4.3.2 Layer Characterization .....	58
4.3.3 Microstructure of as-built samples .....	60
4.3.4 Microstructure of heat-treated samples .....	67
4.3.5 Hardness analysis.....	72
4.4 Summary of the results.....	74
5. DISCUSSION .....	77
5.1 Determination of the Process Map.....	77
5.2 Microstructure evolution during the SLM process.....	81
5.2.1 Solidification sequence .....	82
5.2.2 Effect of in-situ thermal cycle .....	86

6. CONCLUSIONS ..... 89

7. FUTURE PERSPECTIVES ..... 91

8. REFERENCES..... 92

9. ANNEX..... 96



# List of Figures

Figure 1: Schematic illustration of an AM powder bed system [19].....	5
Figure 2: Schematic illustration of an AM powder feed system [20].....	5
Figure 3: Schematically illustration of an AM wire feed system [21]. ....	6
Figure 4: Advantages of SLM technology over conventional methods for biomedical device manufacturing [26]. ....	8
Figure 5: SLM schematic working principle [23]. ....	9
Figure 6: SLM schematic working procedure inside the sealed chamber [27]. ....	10
Figure 7: Graphical representation of SLM process parameters [30].....	11
Figure 8: a “Cross-hatching” scanning strategy (the rotation of the scanning direction by 90°). b The rotation of the scanning direction by 67° [30]. ....	12
Figure 9: illustrative examples of SLM typical defects. a) Keyhole porosity b) Lack of fusion c) Cracks d) Gas porosities. ....	13
Figure 10: Schematic representation of balling effect in SLM technology [30]. ....	15
Figure 11: Formation mechanism of spattering and graphical representation of the three types of spatters [25]. ....	16
Figure 12: SLM prints surface morphology before (A) and after (B) annealing [11]. ....	18
Figure 13: Schematic illustration of gas atomization process for metal powder manufacturing [37]. ....	20
Figure 14: Low alloy steel powders produced by different atomization processes: (a) gas atomization, (b) water atomization [39]. ....	21
Figure 15: Correlation between Temperature gradient (G), Solidification rate (R) and the microstructure [51]. ....	24
Figure 16: Molten pool morphologies and corresponding microstructural SEM images of SLM low-alloy steel samples grown with different $E_d$ s: (a,d) $E_d=284 \text{ J/mm}^2$ ; (b,e) $E_d=71 \text{ J/mm}^2$ ; (c,f) $E_d=29 \text{ J/mm}^2$ [50].	25
Figure 17: Microstructures of SLM low-alloy steel samples grow with different $E_d$ s: (a) $E_d =142 \text{ J/mm}^2$ ; (b) $E_d =71 \text{ J/mm}^2$ ; (c) $E_d =47 \text{ J/mm}^2$ ; and (d) zoomed-in image of (b). GB: granular bainite; M-A: martensite–austenite; LB: lower bainite; BF: bainitic ferrite [50]. ....	25
Figure 18: Microstructure of the as-deposited parts: (a) Low magnification image; (b) high magnification image; (c) SEM photo [55]. ....	26
Figure 19: SEM micrographs of a melt pool (a-b) and details of columnar dendritic (c) and equiaxed dendritic solidification structures (d) at the top layer of as-built samples [56]. ....	27
Figure 20: SEM micrographs of the S2 powders. ....	29
Figure 21: AconityMIDI SLM Machine [58].....	30
Figure 22: Scanner Strategy of 90°/90° [59]. ....	32
Figure 23: Samples used in this work. a) one of the six samples that could not be fully printed; b) the three selected samples used for further characterization. ....	33
Figure 24: Cutting of the samples a) for the Microscope Observations; b) for the DTA Analysis. ....	34
Figure 25: STRUERS equipment [60]. ....	35
Figure 26: Samples after preparation. ....	35

Figure 27: Olympus BX60 [61].....	36
Figure 28: Tescan Clara Ultra-High Resolution [62] .....	37
Figure 29: Samples after preparation with silver paint.....	37
Figure 30: Alicona InfiniteFocus G5 profilometer [63]. .....	38
Figure 31: AccuPyc II Serie 1345 Pycnometer [64].....	39
Figure 32: NETZCH STA 449C Jupiter for DTA tests[65]. .....	40
Figure 33: EMCO M1C 010 [67]. .....	41
Figure 34: OM micrograph showing the macrohardness indentation grid. ....	42
Figure 35: (a) TI 950 Tribointender by Hysitron [68] and (b) OM micrograph showing the nanohardness indentation grid.....	43
Figure 36: Graphical correlation between $E_d$ values and percentages of density of all the fully printed as-built samples.....	45
Figure 37: Process parameters of each samples correlated with the presence of specific surface defects. ...	46
Figure 38: Surface roughness of the samples at increasing volumetric energy density from a) low $E_d$ (Sample 05: 34,72 J/mm <sup>3</sup> ) to b,c,d) medium $E_d$ (Sample 08: 62,5; Sample 12: 83,33; Sample13: 111,1 J/mm <sup>3</sup> ) and e) high $E_d$ (Sample 16: 208,33 J/mm <sup>3</sup> ). .....	48
Figure 39: Overviews of all the cross-sections of the fully printed samples, taken with a 2,5x magnification.....	51
Figure 40: Gas porosity illustrations a) OM micrograph (pores are highlighted in the red boxes) b) SEM micrograph.....	52
Figure 41: Lack of Fusion pores illustrations: a) OM micrograph of a porous area filled with lack of fusion holes b) OM micrograph after etching of a big-sized lack of fusion pore c) SEM micrograph of b) showing unmelted powder particles inside the pore. ....	53
Figure 42: OM micrograph showing a key-hole defect.....	53
Figure 43: Combination of the two variable process parameters used to create the fully printed samples in relation to zoomed parts of the overviews to highlight the presence of porosities. ....	54
Figure 44: Side crack SEM micrographs. On the right a zoom-in of the centre of the same crack showing powder particles underneath.....	55
Figure 45: OM micrograph of a surface spatter. ....	55
Figure 46: Graphic illustrations of the distribution of the pores along the Y-axis of their cross-sections for three different situations of volumetric energy density: a) low (34,72 J/mm <sup>3</sup> ) b)medium (83,33 J/mm <sup>3</sup> ) and c) high (208,33 J/mm <sup>3</sup> ). .....	57
Figure 47: Graphic illustrations of the distribution of the pore size (z-axis) along the cross-section (x and y-axis) for three different situations of volumetric energy density: a) low (34,72 J/mm <sup>3</sup> ) b)medium (83,33 J/mm <sup>3</sup> ) and c) high (208,33 J/mm <sup>3</sup> ). .....	58
Figure 48: OM micrographs of the layer distribution for three different situations of volumetric energy density: a) low (34,72 J/mm <sup>3</sup> ) b)medium (83,33 J/mm <sup>3</sup> ) and c) high (208,33 J/mm <sup>3</sup> ). .....	59
Figure 49: OM micrographs of the top layers for three different situations of volumetric energy density: a) low (34,72 J/mm <sup>3</sup> ) b)medium (83,33 J/mm <sup>3</sup> ) and c) high (208,33 J/mm <sup>3</sup> ); d) Graphic correlation between volumetric energy density and top layer depth of all the fully printed samples. In b) illustrations of the top layer depth and the “apparent melt pool” depth can be found as well. ....	60
Figure 50: OM micrographs after etching: (a) showing the two regions with different macrohardness value and (b) zoomed-in image over the untampered region where the melt pool boundaries are visible;	

(c) image obtained using the scan mode of the nanoindenter showing the top layer region and the two different microstructures inside of it: untempered martensite and austenitization zone. ....	62
Figure 51: OM micrograph of the tempered region with a focus on the three different microstructures which were found. ....	63
Figure 52: SEM micrographs showing the four different areas at the top layer (a) and in the middle of the cross-section (b). ....	64
Figure 53: EDS atomic compositions of martensite: tempered type B (a), tempered type A (b) and untempered (c); comparison between segregation, dark plates and precipitates compositions with the one of the overall area profile. ....	65
Figure 54: OM micrographs of the cross-section of one sample before (a) and after etching (b) with illustrations to highlight the visible growth of the central columnar grain. ....	66
Figure 55: SEM Micrographs showing the presence of dendritic arms inside of the side grain (a) the different growth directions of the grains within one melt pool (b) and two adjacent ones (c). ....	67
Figure 56: DTA heating curve of the AISI S2 as-built, the three arrows highlight the location of the temperatures chosen for the isothermal heat treatments. Explanation of the principal heating peaks detected. ....	68
Figure 57: EBSD analysis results of the heat-treated sample until 300°C: a) Pattern Quality, b) Phase Map and c) IPFZ map with its colours legend. In the Phase Map, the red dots correspond to Iron BCC phase. .	69
Figure 58: OM (a) and SEM (b) micrographs of the top part of the cross-section after treatment up to 600°C; c) EDS atomic compositions of different elements detected in the microstructure. ....	70
Figure 59: EBSD analysis results of the heat-treated sample until 600°C: a) Pattern Quality, b) Phase Map and c) IPFZ map with its colours legend. In the Phase Map, the red dots correspond to Iron BCC phase. .	71
Figure 60: a) SEM micrographs of the cross-sections of the piece after the heat treatment until 900°C; b) zoom-in on the microstructure. ....	71
Figure 61: Graphic results of the macrohardness tests on the three selected samples (a,b,c) and graphic comparison between their overall hardness on the cross-section and top layer (d). ....	72
Figure 62: Nanohardness test results on the as-built sample. ....	73
Figure 63: Different values of Nanohardness among the three selected as-built samples. ....	73
Figure 64: Nanohardness test results on the heat treated samples a) until 600°C b) until 900°C. ....	74
Figure 65: Process map with regards to the printing of AISI S2 metal parts through SLM technology. ....	80
Figure 66: Sketch of the process of melt pool solidification. (a) Melt pool with molten powders after the laser travels by; (b) primary nucleated grains following the orientation of the building direction within the melt pool border (c) epitaxial growth with side-branching phenomenon of the nucleated grains (d) addition of a new powder layer (e) the process new step, which affects the microstructure of the layers below. ....	85
Figure 67: Sketches of two features of epitaxial growth: (a) of columnar grain growth which stays in the same direction along subsequent layers (b) of the side-branching phenomenon between two adjacent melt pools forming a 90° angulation. ....	85
Figure 68: Model of the in-situ tempering effect. ....	88

## List of Tables

Table 1: Main AM equipment sources and specification nching [7].....	4
Table 2: Types and characteristics of metal powders used in SLM technology [11].....	7
Table 3: Chemical composition analysis of the S2 powders. ....	29
Table 4: Technical specifications of Aconity Midi [58].....	31
Table 5: List of process parameters used for the samples fabrication. In red the samples that could not be fully printed.....	32
Table 6: DTA Test parameters. ....	41
Table 7: Density and percentage of density values for each fully printed sample computed.....	44
Table 8: Values of percentage of porosities and density of each fully printed as-built sample. ....	56
Table 9: Process parameters of the three selected samples. ....	61

# 1. INTRODUCTION

Over the past two decades, Additive Manufacturing (AM) has gained remarkable attention due to its capability of fabricate layer-by-layer 3D parts directly from a CAD model [1]. AM of metallic components can be carry out through Selective Laser Melting (SLM), a promising laser powder bed fusion technique which allows the layer-wise manufacturing of metal parts. As an AM process, it is able to produce robust near-net-shape pieces with complex geometries and inner functional structures [2]. Most steels commonly used with SLM are austenitic stainless steels such as AISI 316L, AISI 304L or maraging steels. However, these alloys are not suitable for certain applications because of, for instance, their insufficient wear resistance [3]. While tool steels with high content of carbon ( $>0,4$  wt.-%) might be a more adequate solution, they are considered as unweldable. This is due to the brittle martensitic phase that forms in AM out-of-equilibrium conditions [3], [4] and because of the presence of a network of solidification carbides which decreases both the toughness and the corrosion resistance of the material. However, recent promising studies have shown how to mitigate these issues [1], [3], [5], [6], but a more profound investigation needs to be achieved. For the latter reason, in this present work a carbide-free AISI S2 tool steel have been selected and processed by SLM prior to an in-depth microstructural characterization of the printed pieces.

This Master's thesis consists in a part of a PhD thesis which aims to fabricate new innovative alloys which could perform good self-lubricating properties, especially made by mixture of powders, using the SLM process. Thus the tool steel solely processed by SLM may correspond to an intermediate stage for which no specific application is expected, as the final product will be made of a compound. Nevertheless, the focus in this work will be put on multiscale characterization that can help to better understanding what occurs for the microstructure evolution during SLM processing.

Twenty pieces of AISI S2 were fabricated using different combinations of processing parameters. From literature it has been known how the volumetric energy density parameter can deeply affect the quality of the printed parts [2]–[4], [7]–[11]. Therefore, the different effects that the broad range of parameters had generated were investigated, aiming to find the optimum set-up to produce defect-free samples which are fully dense in the as-built conditions.

It has to be aforesaid that the information regarding the process and the microstructure of the as-fabricated pieces present in literature is lacking on details about the prior microstructure yielded by SLM process, especially for AISI S2 tool steel that remains under-studied. In addition, AM processes lead to out-of-equilibrium and complex structures that need in-deep studies.

Indeed, SLM is a process involving heating and cooling cycles, which initiates in situ processes similar to tempering, relaxation or precipitation that in turn affects the microstructure in the already solidified previous melt pool [12]. Understanding of these processes and an ability to control them is a huge advantage that can provide predictable and tailored microstructures and properties in SLM parts [12].

The microstructural investigation is carried out using several techniques such as Electron Backscattered Diffraction (EBSD) under Scanning Electron Microscope (SEM), reversed Differential Thermal Analysis (DTA), nanoindentation and post iso-thermal treatments. Crossed analyses performed while combining different characterization methods then allow to achieve in-depth understanding of major metallurgical phenomena that occurs either during SLM processing, or latter when post thermal treatments are carried out. All these features help to understand the microstructural evolution of the studied alloy under SLM processing. These innovative ways to investigate could set the ground for future studyings of AM-fabricated metal parts.

## 2. STATE OF THE ART

This chapter presents the state of art of the topics needed for the discussion of the results. The main treated matters are: (1) Additive Manufacturing (AM) technology, focusing on the Selective Laser Melting (SLM) process; (2) the materials mostly utilized in AM and in this present study: low-alloyed steel powders; (3) the microstructural elements expected to be found and characterization techniques commonly used for AM parts.

### 2.1 Additive Manufacturing (AM)

Additive Manufacturing, also known as 3D printing, is a “process of joining materials to make objects from 3D model data, usually layer upon layer, as opposed to subtractive manufacturing methodologies” [13]. This definition, from ASTM 52900-15 [14], is applicable to all kind of materials including metals, ceramics, polymers, biological tissues and composites.

AM has attracted much attention over the past years due to its immanent advantages, such as unrivalled design freedom and short lead times [15]. These techniques have already been known for more than 20 years but were at first limited to the rapid manufacturing of porous structures and prototypes. More recently, AM has been used to fabricate end-use products in aircraft, dental restorations, medical implants, automobiles, and even fashion products [16]. It has become possible to reliably manufacture dense parts with certain AM processes for several metallic alloys such as steel, aluminium and titanium [17].

Thus, AM transformed more and more from rapid prototyping to rapid manufacturing applications, which require not only profound knowledge of the process itself, but also of the microstructure resulting as a consequence of the combination of process parameters utilized and consequently of the properties of the fabricated parts. AM technology does not require moulds, fixtures or tooling that increase the time production. In addition, AM can guarantee near net shaping which can effectively minimize material usage and waste. Not only these benefits, but also other advantages come as a product of AM technologies, such as the production velocity, green manufacturing, cost saving and design freedom. Moreover, there is a opportunity to increase the geometric complexity of the object without increasing the production cost, weight reduction by rethinking the shape, short delivery times, and ultimately some techniques also allow the addition of functionalities and one-shot manufacturing of multi-material [18].

From the many technologies available, only a few allow producing metallic parts that fulfil the requirements of industrial applications [16]. Therefore, recent studies are turning their interests in the field of additive manufacturing of metals. The latter term is used to describe freeform processes that offer the possibility to produce complex-shaped parts without the design

constraints of traditional manufacturing routes. The process relies on the transfer of a digital file to a machine that then builds the three-dimensional component layer by layer from feedstock using a laser or an electron beam to fuse the particles together [5]. Over the last decades, the numerous progress within the constituent techniques of AM, involving higher energy density lasers, additional rational computer code management systems, and additional economical powder preparation strategies, boosts it to become a mature and prevalent digital processing technology [19]. This technology enables the integration of design freedom, material diversity, and green manufacture, making it widely accepted as a new paradigm for the production of high-end components for critical applications, such as in aerospace, automotive, and health-care fields [19].

AM system is also classified in terms of the fabric feedstock, energy supply, build volume, etc. Table 1 represents a list of different technologies and their equipment. In this table, manufacturing systems are divided into three broad categories (while there are many more): powder bed systems, powder feed systems and wire feed systems [7].

System	Process	Build volume (mm)	Energy source
<b>Powder bed</b>			
ARCAM (A2)(a)	EBM	200 × 200 × 350	7 kW electron beam
EOS (M280)(b)	DMLS	250 × 250 × 325	200-400 W Yb-fiber laser
Concept laser cusing (M3)(b)	SLM	300 × 350 × 300	200 W fiber laser
MTT (SLM 250)(b)	SLM	250 × 250 × 300	100-400 W Yb-fiber laser
Phenix system group (PXL)(c)	SLM	250 × 250 × 300	500 W fiber laser
Renishaw (AM 250)(d)	SLM	245 × 245 × 360	200 or 400 W laser
Realizer (SLM 250)(b)	SLM	250 × 250 × 220	100, 200, or 400 W laser
Matsuura (Lumex Advanced 25)(e)	SLM	250 × 250 diameter	400 W Yb fiber laser; hybrid additive/subtractive system
<b>Powder feed</b>			
Optomec (LENS 850-R)(f)	LENS	900 × 1500 × 900	1 or 2 kW IPG fiber laser
POM DMD (66R)(f)	DMD	3,200° × 3°, 670° × 360°	1-5 kW fiber diode or disk laser
Accufusion laser consolidation(g)	LC	1,000 × 1,000 × 1,000	Nd:YAG laser
Irepa laser (LF 6000)(c)	LD		Laser cladding
Trumpf(b)	LD	600 × 1,000 long	
Huffman (HC-205)(f)	LD		CO <sub>2</sub> laser cladding
<b>Wire feed</b>			
Sciaky (NG1) EBFFF(f)	EBDM	762 × 483 × 508	>40 kW @ 60 kV welder
MER plasma transferred arc selected FFF(f)	PTAS FFF	610 × 610 × 5,182	Plasma transferred arc using two 350A DC power supplies
Honeywell ion fusion formation(f)	IFF		Plasma arc-based welding

Country of Manufacturer: (a) Sweden, (b) Germany, (c) France, (d) United Kingdom, (e) Japan, (f) United States, and (g) Canada

Table 1: Main AM equipment sources and specification [7].

Regarding the powder bed system, a powder bed is created by raking powder across the work area (Figure 1). The energy supply (electron beam or laser beam) is programmed to deliver energy to the surface of the bed melting or sintering the powder into the required form. Then, additional powder is raked across the work space, and the method is repeated to generate the solid three-dimensional piece. The advantages include its ability to produce high resolution features, internal passages, and maintain dimensional control [20].



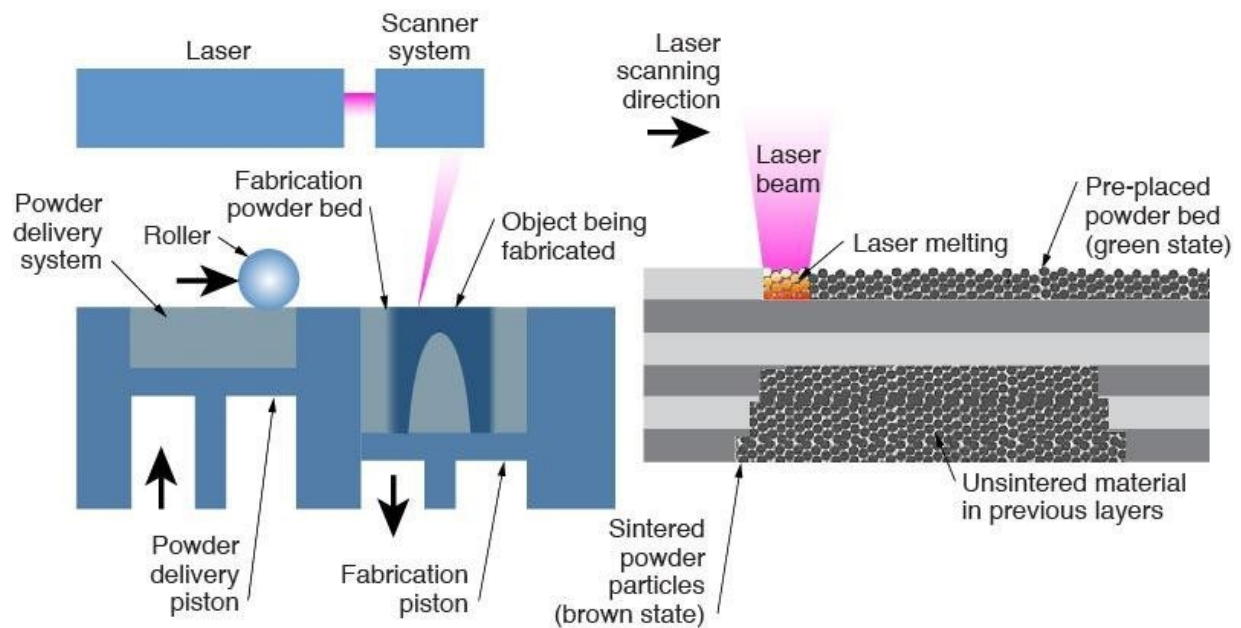


Figure 1: Schematic illustration of an AM powder bed system [20].

Subsequently, a schematic illustration of an AM powder feed system is shown in Figure 2. Powder are conveyed through a nozzle on the build surface. A laser is used to melt a monolayer or more into the desired shape. The advantages of this type of system include its larger build volume and its ability to refurbish worn or damaged components [21].

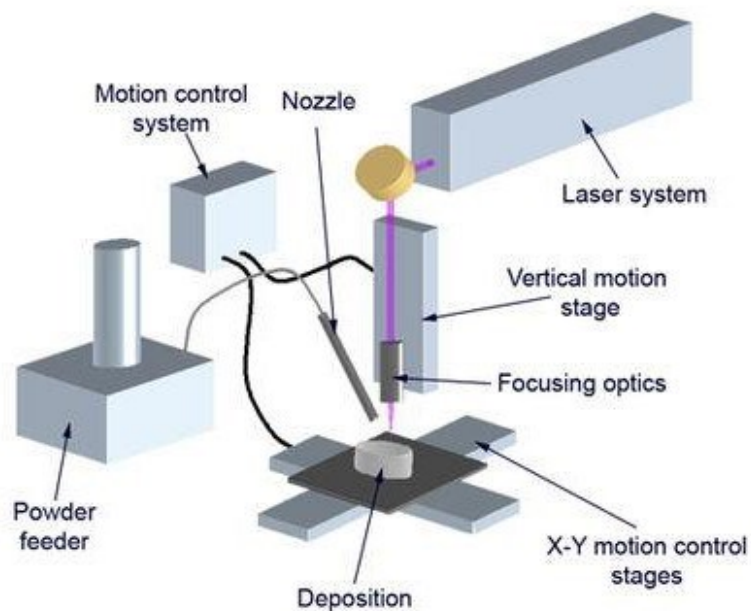


Figure 2: Schematic illustration of an AM powder feed system [21].

With reference to the wire feed systems, in this situation the feed stock is a wire and the energy supplier may include electron beam, laser or plasma arc. Firstly, a single bead of material

is deposited and upon subsequent passes is built upon to develop a three-dimensional structure. The wire feed system is well suited for high deposition rate and for large build volumes. However, the final product usually requires extensive machining (Figure 3) [22].

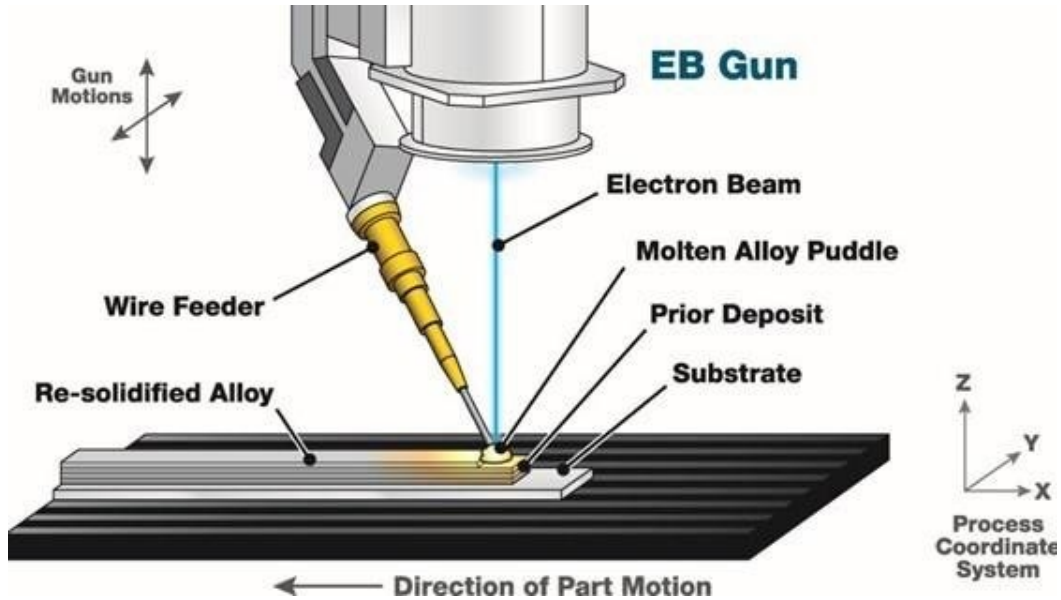


Figure 3: Schematically illustration of an AM wire feed system [22].

The most popular processes for AM of metals are Laser Beam Melting (LBM), Electron Beam Melting (EBM), and Laser Metal Deposition (LMD). LBM process is also known as Selective Laser Melting (SLM), Direct Metal Laser Sintering (DMLS), Laser CUSING, Laser Metal Fusion (LMF) or industrial 3D printing. LMD process is also called Direct Metal Deposition (DMD), Laser Engineered Net Shaping (LENS), Laser Cladding (LC) or laser deposition welding. Most of these names are trademarks of different machine manufacturers.

### 2.1.1 Selective Laser Melting

Among Powder-Bed Fusion (PBF) Additive Manufacturing processes, SLM is an impressive development of the AM technology as it has the potential to obtain parts with fine microstructure and high mechanical properties [23]. The SLM technology uses high-energy laser beam which selectively melts the metal powder layer by layer according to the contour data by means of layered powder levelling, melting, and solidification. During the layer processing, the powder bed drops and the powder feeder is spread with a layer of powder at the same time. Differently from traditional metal processing strategies, SLM processing technology usually uses ultrafine powder with a particle size of about 30  $\mu\text{m}$  as raw material [11].

SLM technology is characterized by complete melting and solidification of the metal

material, making it suitable for successfully processing pure metals, alloys, and metal matrix composites. Table 2 shows the main metal materials used in this technology and their preparation methods. The characteristics of metal powder feedstock such as particle size distribution, particle shape, fluidity, oxygen content, and absorption rate of powder materials directly affect the processing quality of SLM final parts [11].

Powder type	Iron-based (316L, 420, M2), titanium and titanium-based (Ti6Al4V, TiAl), aluminum-based (AlSi, AlCu, AlZn), nickel-based (Inconel 625, 718), copper, etc.
Preparation method	Water atomization, gas atomization, rotating electrode method
Particle size distribution/ $\mu\text{m}$	20–50
Oxygen content/ppm	$\leq 1000$

*Table 2: Types and characteristics of metal powders used in SLM technology [11].*

Compared to conventional casting and forging processes, the molten pool has a very high cooling rate about  $10^3$ - $10^6$  K/s, hence the solidification process is in non-equilibrium and its rapid cooling causes a complex thermal history and therefore a microstructure which is hardly predictable. Secondly, in the SLM process different energy inputs might be used, their values strongly affect the melt pools shapes and conditions. As a consequence to these two aspects, parts formed through SLM process present defects such as porosities, cracks and internal stresses together with supersaturated phases.

Although substantial progress has been achieved in comprehending the SLM process and fabricating different materials with this process, the industrial application is still restricted [24]. Limitations related to the efficient process parameters for different materials and defects on the printed parts are some of the main hurdles buried in this method that prevent it from manufacturing functional parts [24]. Moreover, there are significant challenges in making high performance and reliable products regarding metallic parts, inherently relate to the formation of porosity and complex microstructure development in solidification. To address such challenges, in addition to many efforts in obtaining insights into processing phenomena, it is necessary to have in-depth understanding of complex microstructure development during solidification from the single-track to multi-layer depositions with various scan strategies and the influence of process parameters to increase the confidence in tailoring the microstructure, and thereby the properties of alloys [25].

SLM has received heightened attention from the scientific society thanks to its multiple advantages (Figure 4). Its technology overcomes the design limitations of the traditional methods. It is capable of fabricating complex, compact structures (density up to 99.9%) by metallurgical bonding and provides excellent mechanical properties [26]. Hence, SLM is widely used in aerospace, medical and automotive applications. Its technology is particularly suitable for the development and even production of single parts and new and single-volume products in the aerospace field being a solution against traditional processing methods issues, such as many manufacturing processes, long cycles, and difficult-to-form complex structures[11].



Figure 4: Advantages of SLM technology over conventional methods for biomedical device manufacturing [27].

**2.2.1.1 Process mechanism**

As all AM technologies, The SLM process starts with a CAD model that contains information about the areas to be melted in separate layers, the 3D model data is later revolved into a 3D near-net functional component. Subsequently, the as-built parts can undergo post-processing treatments to achieve the final properties, as shown in Figure 5.

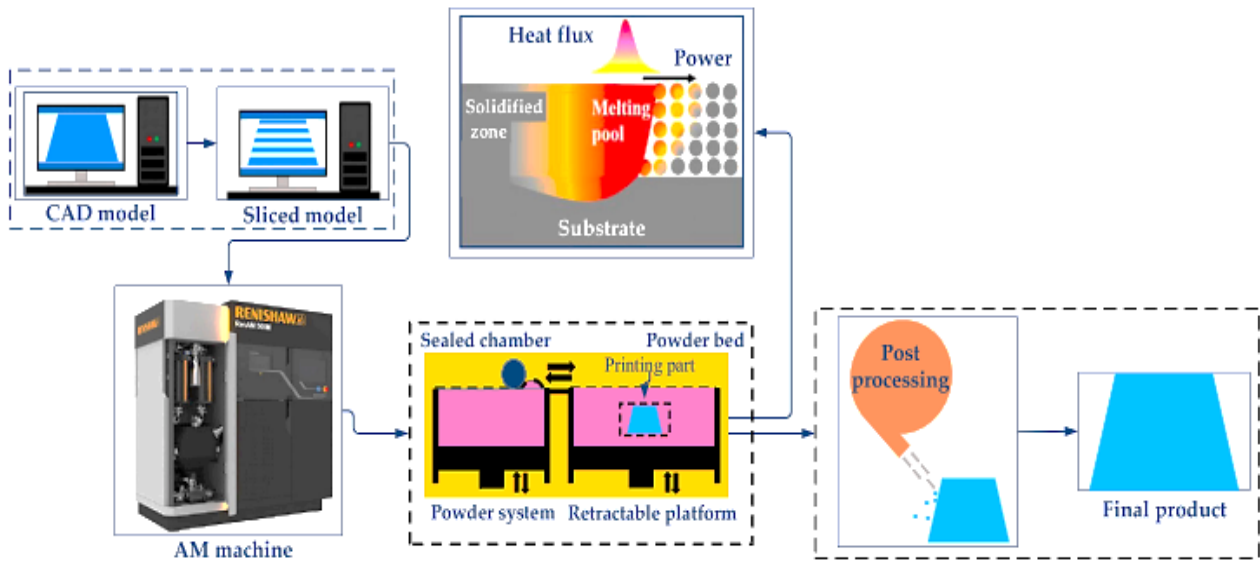


Figure 5: SLM schematic working principle [24].

During the SLM process, 3D components are digitally "cut" into thin 2D layers. Each sliced layer is further developed with the appropriate scan paths. Through the scanner mirrors, a laser beam selectively scans and melts the powders that are previously paved on the substrate [9]. At this point in the powder bed, the cohesion of the particles is achieved via a high-performance laser that exposes the contours and surfaces of the 2D layers, causing the powder to melt and bond locally at these points. The process is formed by the interaction between the laser and the powder which includes a series of physical and chemical processes, together with energy transfer and physical state changes. After a layer is finished, the building platform is lowered by an amount equal to the layer thickness, and a new layer of powders is paved (Figure 6). The process repeats until the completion of the whole part and the components can now be separated from the platform. Heat treatment is suitable as post-processing in order to eliminate thermal stresses [28] as it will be deeper explained in the paragraph 2.2.1.3.

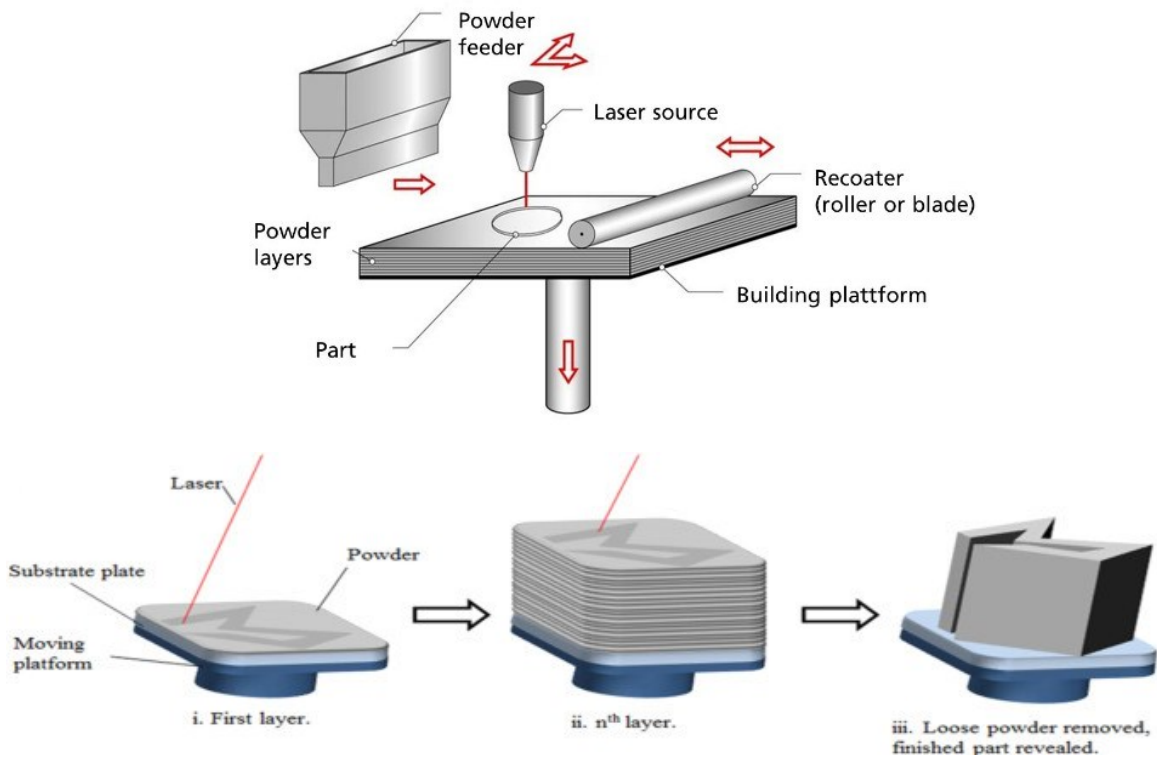


Figure 6: SLM schematic working procedure inside the sealed chamber [28].

### 2.2.1.2 Influence of process parameters and defects

Selective Laser Melting is a technology for which the mechanical properties of printed metal parts are highly dependent on the printing parameters. Indeed, given the presence of a wide spectrum of custom-made and commercially available SLM systems, the manufacturing of parts is affected by a large number of different deposition parameters, at least 130 according to Yadroitsev [29]. As a consequence, the tailoring of the proper process parameters is paramount for the manufacturing of SLM parts, especially in order to achieve fully dense parts with minimized defects such as porosity, incomplete fusion holes, and cracks [24]. Achieving full density in final parts is, for instance, one of the most desired outcomes in additive manufacturing (AM) since the retention of even minimal amounts of residual porosity seriously degrades mechanical properties [30].

Researchers have often presented their results on final part porosity using an approach based on the volumetric energy density ( $E_d$ ), finding that in many cases when deposition occurs in a specific energy density range, final porosity can be minimized [30]. Therefore,  $E_d$  is a parameter of crucial importance for the fabrication of SLM pieces. This parameter reflects the laser beam's energy transmitted to a volumetric unit of powder material and correlates with

several relevant laser and scan parameters, from the empirical equation:

$$E_d \left( \frac{J}{mm^3} \right) = \frac{P}{D_h \cdot D_s \cdot v_s} \quad \text{Equation 1}$$

Where P is the laser power (W), which is the energy intensity of the laser beam;  $v_s$  is the scanning speed (mm/s), the traverse speed of the laser beam;  $D_h$  is the hatch distance (mm) which is the gap between two head-to-head scan pathways; and  $D_s$  layer thickness (mm): the thickness of a layer that equals one incremental amount of the powder bed. The graphical representation of the track parameters is shown in Figure 7 [31]. In addition, the value of energy density differs from material to material and a value greater than the materials specific energy density range leads to a wider and deeper melt pool [24]. This means that the building job can be modified by changing the different parameters which indirectly and/or directly affect the quality of the melted area [30].

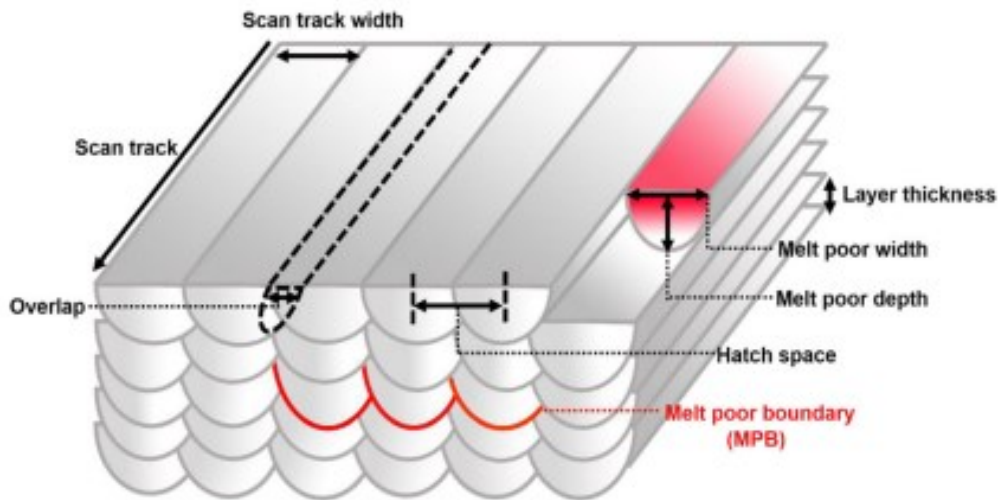


Figure 7: Graphical representation of SLM process parameters [31].

During the SLM process a high-power laser with a distinctive pattern melts the powder and creates 3D parts. In this stage, powder particles absorb energy when the high energy laser beam irradiates on the powder bed. A transient temperature field with high temperature and rapid cooling rate will occur, both of the events will deeply affect the microstructure and mechanical properties of the specimens [31]. Therefore, the  $E_d$  value becomes really influential with regards to the overall quality of the as-fabricated pieces.

Indeed, based on different laser energies and residence times, the metal powder undergoes corresponding state changes by absorbing different laser energies. For instance, when the laser energy is low or the residence time is short, the metal powder absorbs less energy, thus only the surface temperature of the metal particles rises and the material softens and deforms, still exhibiting a solid state. While if the laser energy is high, the temperature of the metal powder

exceeds its own melting point, and then the metal particles appear to be in a molten state. When the laser energy disappears instantaneously, the molten metal cools rapidly to form fine-grained parts [11].

A few studies analysed the effects of the tailoring of process parameters in SLM technologies. For example Zhang, et al. [9] studied the defect formations in the SLM process, and they concluded that the energy density process parameters could control defects in the SLM process. Additionally, most of the defects are found at the scan track endpoint and between two adjacent tracks, meaning that scan strategy is influential parameter for the location distribution of defects [24].

Parameter optimization enhances the printed part quality; however, understanding each process parameter imparts a good quality product. All the process parameters are significant based on the study response, therefore, increasing or decreasing the magnitude of parameter levels must depend on the material properties and the required properties of the specific case study.

As previously mentioned, besides the volumetric energy density parameters, a combination of an ideal scanning strategy can significantly enhance the mechanical properties of the printed part. The two most common scan strategy used for SLM processes are shown in Figure 8 [31]. Among them, the so called “cross-hatching” scan strategy (Figure 8a) can make the entire laser energy input more balanced in the whole layers, which effectively prevents defect accumulation and propagation [9].

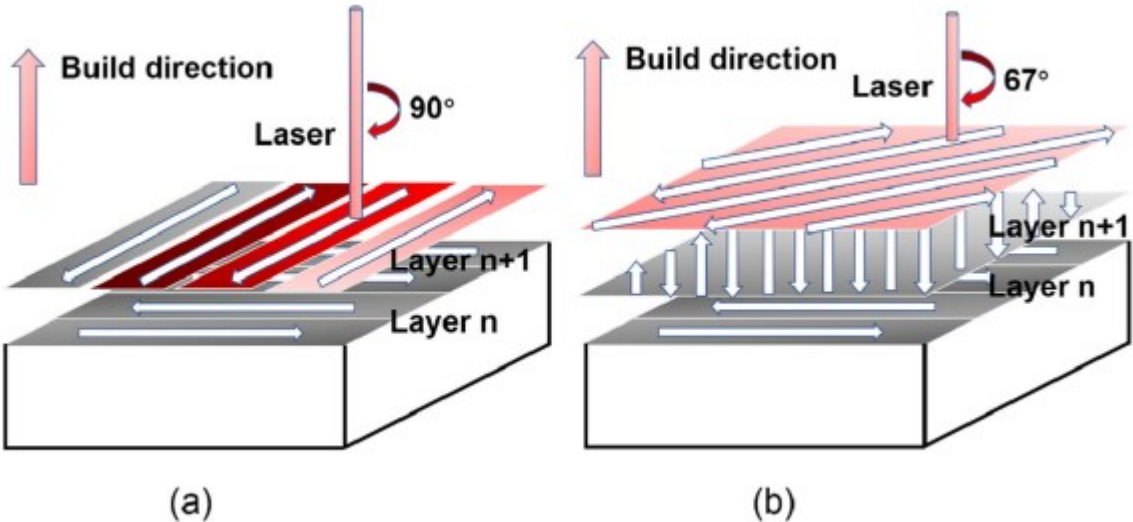


Figure 8: a “Cross-hatching” scanning strategy (the rotation of the scanning direction by 90°). b The rotation of the scanning direction by 67° [31].

Defect formation is a critical problem in the SLM processes and it has a significant influence on the real-world application of the SLM fabricated parts. For the latter reason, it is



necessary to have an in-deep knowledge of the defects structure and formation.

3D printed SLM parts often contain porosity that can lead to changes in the local thermal field and therefore alter the solidification microstructure. In these technologies, porosity can be categorized into three groups based on the mechanism of formation: key-holes, entrapped gases and lack of fusion [25]. Key-hole occurs when excessive power density is used in melting the material, leading to the penetration of the power beam deep into the beneath layers (Figure 9a). Lack of fusion occurs when there is insufficient molten metal to flow to fill gaps, leading to irregular pores (Figure 9b). Pores formed due to entrapped gases are either from pre-existing gas inside powder or vaporized material during fusion. These pores are usually spherical and typically smaller than keyhole pores and lack-of-fusion pores (Figure 9d). The presence of pores can cause disruption to crystal growth depending on the size of pores [25]. Indeed, small entrapped gas bubbles do not cause any significant changes in solidification microstructure. Meanwhile big pores can serve as thermal insulation, leading to reductions in both the thermal gradient and the cooling rate in the regions above pores [25].

Besides porosities, cracks can also occur within 3D SLM printed parts which need to be taken into account. Among the many reasons for cracks formation of in SLM printed parts, there are collisions between specimens and the powder recoating machine and high thermal stresses associated with the manufacturing SLM process, the latter leading to which delamination from the base plate (Figure 9c) [31].

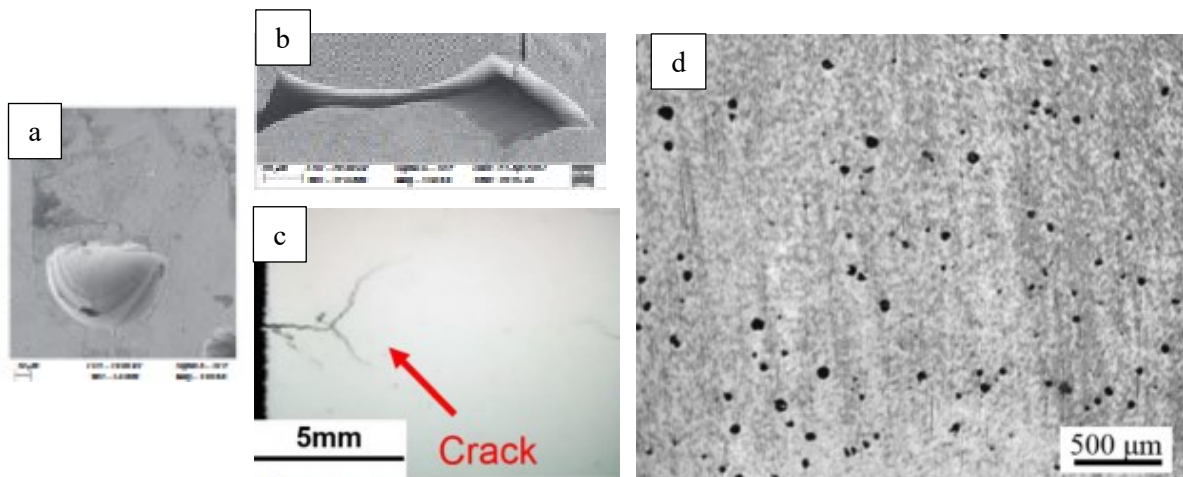


Figure 9: illustrative examples of SLM typical defects. a) Keyhole porosity b) Lack of fusion c) Cracks d) Gas porosities.

A source of macroscopic defects like cracks and a reason for achieving a bad surface roughness is the balling effect (Figure 10). The surface roughness is one of the most important features of complex geometry in AM production, usually originated from insufficient melting of

the powder particles on the powder bed or balling effect.

The reasons for balling effect are multiple [31]. Firstly, when the laser power is above a certain value, there is evaporation and splashing into the molten metal pool, the splashed liquid will fall into the molten pool and form a small spheroidizing area. Excessive laser energy input causes a steep temperature gradient between the centre and the edge of the entire surface, resulting from the surface tension gradient and the resulting Marangoni effect [32]. As a result of the Marangoni effect, the melt has a tendency to flow radially inward to the centre of the melt pool rather than outwards on the surface below. As well as a high laser power, a low one can cause a balling effect too. Laser sintering is a line-by-line process in which the powder particles absorb energy as the solidus sintering temperature decreases with the laser power, which results in the amount of liquid reducing. This causes the rearrangement of liquid flow, thus the molten material in the focused spot area of each point tends to aggregate into a single coarsening sphere, whose diameter is approximately the diameter of the laser beam. Regarding the scanning speed, if it is high, the melt droplet is easier to splash from the surface of the molten track, thereby producing longitudinal cracks in the finally solidified tracks. On the other hand, a very low laser scanning also results in a balling effect. The interaction time between laser and powder is relatively long with a slow scanning speed, which leads to an excessive local liquid. Due to the too large molten pool, the powders around it are sucked into the pool, resulting in the shortage of powder in the original position. As a consequence, cracks and surface roughness caused by the balling effect are the major macroscopic characteristics [31].

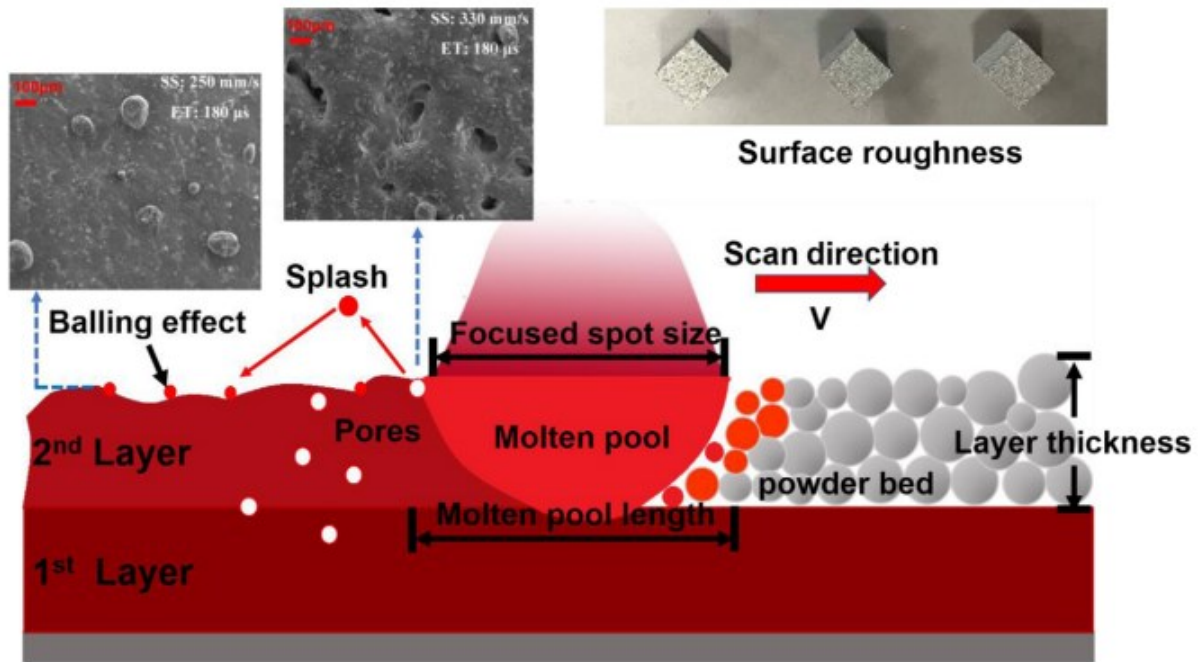


Figure 10: Schematic representation of balling effect in SLM technology [31].

Another issue with SLM fabrication is that the metal powders solidify quickly after melting in the presence of high-energy laser beams. Additionally, the complicated heat conduction process is usually accompanied by spattering, which greatly influences the stability, energy utilization of the fabrication process, and quality of the fabricated structures [33]. Spattering is very common in laser manufacturing. During the processes the laser beam that is applied to the processed material can have a very high volumetric energy density. For the latter reason the surface of the material is melted and at times, vaporized into plasma to help the material absorb the laser. Under the blow off impulse pressure, the melted material is compressed to cause some liquid material to leave the molten pool at a certain speed, thereby forming the spatters [26]. Observing and analysing dynamic variations of spatters by varying energy inputs reveals a close relationship between the formation mechanisms of spatter and the volumetric energy density. Therefore, spattering is greatly attributed to thermodynamic, dynamic, and metallurgical instability of the small molten pool. As shown in Figure 11, the surface of the liquid deforms and is sunken under the vaporization pressure, therefore the one in the molten pool at high elevation instantly collapses due to the force of gravity [26]. The recoil pressure associated with extreme expansion of the gas phase causes the metal jet (type-I spatter). Meanwhile, in order for surface energy to reduce in the presence of surface tension, the jetted liquid metal stretches during its flight and decomposes into small drops, causing droplet spatter (Type-II spatter). Simultaneously, non-melted powder particles splash at the front of the molten pool

(Type-III spatter) [26]. The presence of such defect as spatters obstruct the printing process until the point that it might impede it, leading to failure. The control of the volumetric energy density input can help mitigate similar situations.

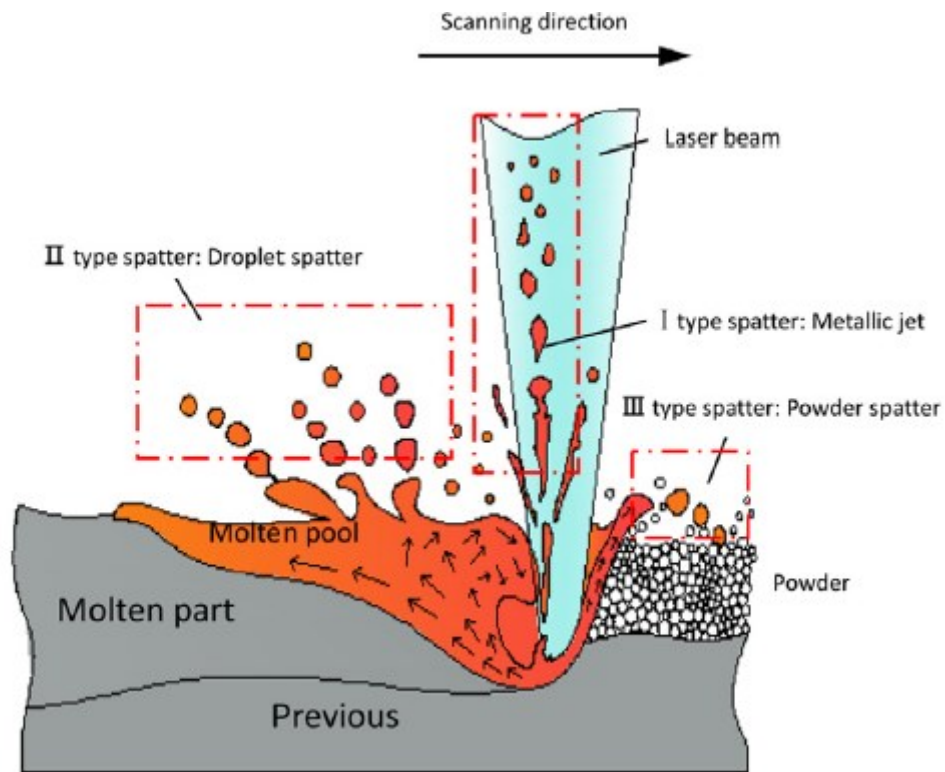


Figure 11: Formation mechanism of spattering and graphical representation of the three types of spatters [26].

In conclusion, macroscopic characteristics of steels produced by SLM lie in the correct process parameters that lead to the proper volumetric energy density value, mainly laser scanning speed and laser power. Since defect formation has a significant influence on the mechanical properties of the SLM fabricated parts, which restricts the application of the SLM technique, the quality control in an SLM process relies on defect detection and elimination. For high quality SLM fabrications, defect monitoring, simulation and modelling, as well as real-time defect elimination become necessary [9].

### 2.2.1.3 Post-processing Thermal Treatments

SLM is a promising technique, however, as it has been described in the previous paragraph, it has greater issues which can occur, such as evaporation, balling, spattering, porosities, cracks and thermal stress deformation that can seriously affect its practical application. Besides the process parameters and scan strategy control, it is possible to consider the use of post-processing heat treatments to eliminate part defects, extend service life, and

improve the overall performance of the parts. Common heat treatments methods include hot isostatic pressing (HIP), cold isostatic pressing (CIP), annealing, and solid solution strengthening [11]. The selection of the post-processing process depends on the type of materials, geometry, and types of required surface quality.

One of the most used post-processing method is the isostatic pressing technology, which ensures higher densities (up to 100%) of the part while also ensuring uniform microstructure and good mechanical properties. Therefore, powder metallurgy additive manufacturing technology and isostatic pressing can be combined to produce parts with complex shapes and high density without the use of complex metal sheaths. Isostatic pressing can be divided into hot isostatic pressing (HIP) and cold isostatic pressing (CIP) according to the temperature at which it forms and consolidates [11]. Afterwards, the SLM parts have more uniform microstructure, exhibiting excellent elongation and fatigue properties [11].

Common annealing processes include stress-relief, recrystallization, and full annealing processes. Among these, the stress relief annealing can help improving the unevenness of the microstructure in the micro-melting pool, and eliminate the huge residual thermal stress in the processed part due to rapid melting/solidification, thereby improving the anisotropy of the processed part and reduce the possibility of being subject to cracking phenomena (Figure 12). While the recrystallization annealing process can eliminate the anisotropy of the mechanical properties of SLM parts, but the overall tensile strength will be reduced, and the grain orientation will no longer have obvious directionality. For the full annealing process, it can change the microstructure of the processed part, leading to either dissolution and recrystallization under heating, or precipitation or solid state transformation during cooling. However, grains with significantly coarse microstructure may cause deterioration of the mechanical properties of the SLM parts [11].

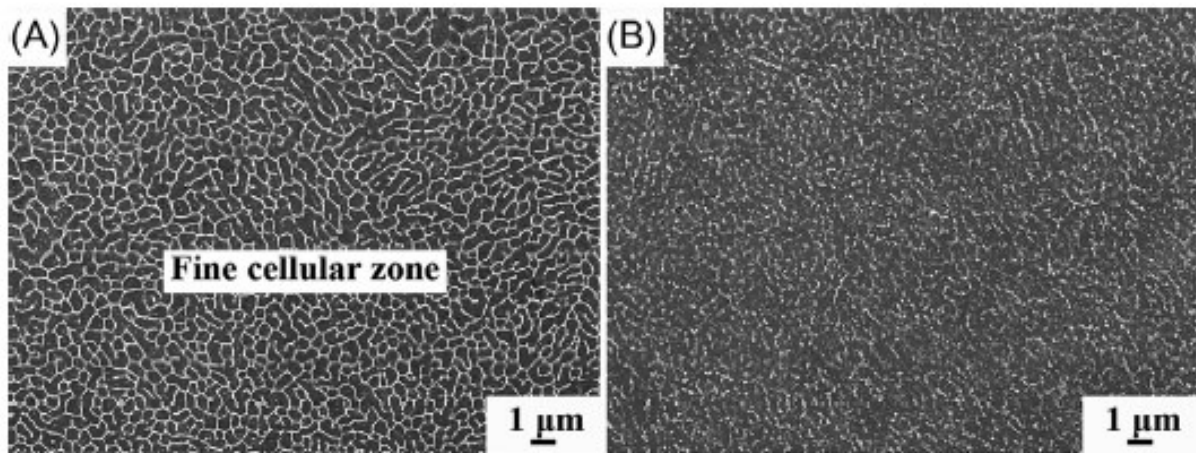


Figure 12: SLM prints surface morphology before (A) and after (B) annealing [11].

The third most-commonly used SLM post-processing treatment is solid solution strengthening. This method can help achieving a certain type of hardening which corresponds to the inclusion of substitution elements within the matrix to increase its strength [34]. In postprocessing, the solute atoms incorporated into the solid solution cause lattice distortion, which increases the resistance of the dislocation motion, making it difficult for the slip to proceed, thereby increasing the strength and hardness of the alloy solid solution [11]. Through adjustment of the solid solution parameters, the grain size of the steel can also be controlled to soften the structure of the steel [11].

In addition, one of the major challenges in the metal AM process is the surface quality of the manufactured component. The as-fabricated parts generally exhibit inadequate and poor surface quality in the as-built configuration. The surface imperfections and defects ranging from staircase effect due to the layer by layer nature of the deposition techniques, partially fused feedstock material, balling effects, spatters, or inadequate fusion lead to a notably irregular surface morphology [35]. This high surface roughness can significantly deteriorate the performance of the additive manufactured parts imposing a substantial limit on their prospective applications; for instance, fatigue performance, wear and scratch resistance [35]. A great effort has been lately dedicated to developing post-treatments for improving the surface quality of additively manufactured metallic parts [35]. Laser polishing, magnetic field-assisted finishing, grinding, blasting, polishing, and other post-processing techniques have been used with the additive manufactured metallic components to increase surface quality and regulate surface integrity characteristics [24].

## 2.2 Materials involved in AM processes

AM technology has completely changed the way and principle of traditional manufacturing, which is a subversion of the traditional manufacturing model [36]. At present, AM materials have become the main bottleneck restricting the development of AM, as well as the key and difficult point of making breakthrough in AM technology [36]. Only by developing more new materials can the application field of AM technology be expanded. Currently, AM materials mainly include polymer materials, metal materials, ceramic materials and composite materials [36]. As the present work deals with the fabrication and characterization of metal parts, this chapter will focus on the production of AM metal materials.

Metal additive manufacturing (AM) is, among the AM processes, one of the most impactful. Metallic components are created through the accumulation of metallic materials in the form of powders, wires, or sheets via a layer-by-layer manner using various energy sources [19]. The two main forms of feedstock for metal AM are wire and powder, their characteristics play an important role in influencing the processing windows or the functionalities and properties of fabricated components [19].

Wire feedstocks are generally welding wires produced from casting, roll bonding, drawing, or extrusion techniques. For this kind of feedstocks, contaminants and defects on the wire surface such as cracks and scratches may result in porosity in the fabricated components. Wires used for AM are typically range from 0.45 to 1.2 mm [19].

Powder feedstocks, which are the ones used in the current study, are mainly produced using atomization methods [19]. For metal powders, key characteristics are particle size distribution (PSD), particle shape, high bulk density, flowability, and chemical composition. These characteristics play a vital role in either the processing window establishment or the functionalities and properties of printed products [19]. The atomization method mainly includes water atomization and gas atomization, which is also the method utilized for producing the metal powder of this work. The powder prepared by gas atomization has the advantages of high purity, low oxygen content, controllable powder particle size, low production cost and high sphericity, and has become the main development direction of high performance and special alloy powder preparation technology [36]. The main principle of all atomization technologies is the fragmentation of a stream of molten metal by the impact of water, gas, oil or by mechanical dispersion [37]. During this process, molten metallic material is broken up into fine particles by impingement with gas or water. The atomization of metals can also be done by utilizing centrifugal force to disintegrate the melt into small powder particles [38].

Figure 13 shows the schematic illustration of powder manufacturing via gas atomization

processing. In the commonly used gas atomization process, a melt of elemental alloyed material passes through an orifice, and struck by a high pressure gas stream, before falling into a chamber where it cools and solidifies as it falls [20]. The powder is then collected and subsequently annealed to make it ready for use in manufacturing [20]. While in liquid atomization of molten metals, the melt stream is generally interrupted by spraying a high-pressure liquid, which rapidly cools and solidifies the melt droplets. Compared to gas atomization, liquid atomization results in less porous, smaller, and higher purity particle with wider particle size distributions [39]. On the other hand, with water atomization process, particles have irregular shape, while powders obtained by gas atomization process present a spherical or near to spherical shape (Figure 14).

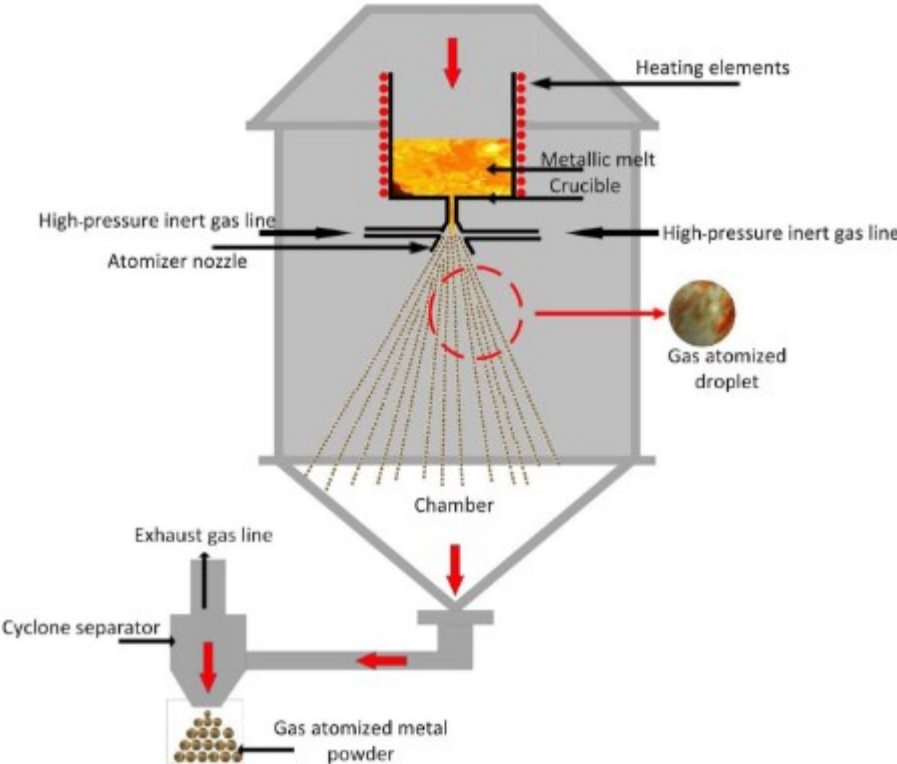


Figure 13: Schematic illustration of gas atomization process for metal powder manufacturing [38].



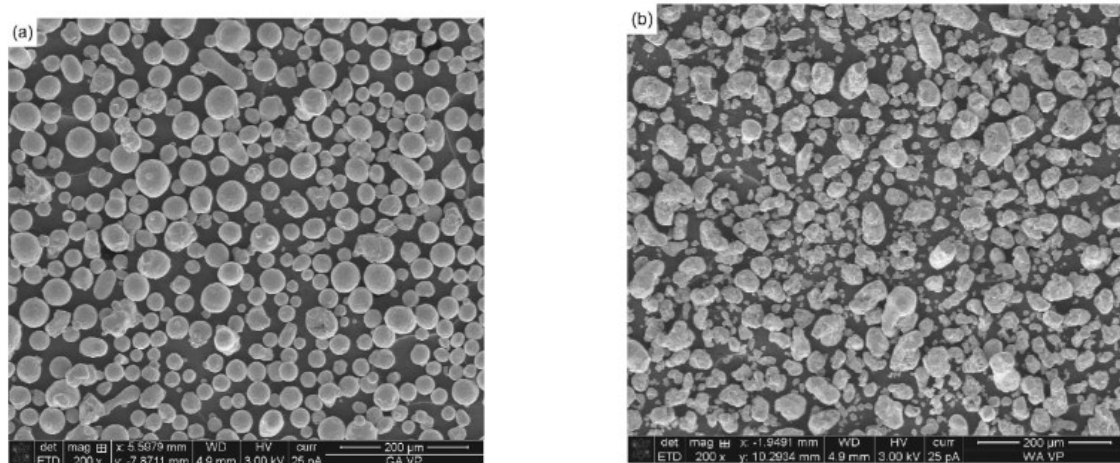


Figure 14: Low alloy steel powders produced by different atomization processes: (a) gas atomization, (b) water atomization [40].

The gas atomization processing is characterized by its high mass flow rate, and it is therefore frequently used for the production of metal powders with a mass median diameter ranging from 10 to 100  $\mu\text{m}$ . However, the wider particle size distributions of metal powders and the higher consumption of specific gases are major limitations of this process, as a wide particle size distribution of the raw metal powder correlates to a lower productivity [41]. Moreover, there are still two unavoidable issues in gas atomization-prepared powder particles. The first issue is that a substantial amount of satellite particles are generated when solidified metal particles rebound from the bottom of the chamber and collide with the falling molten particles. The other issue is the formation of gas pores or bubbles within the metal particles when the partial high-pressure gas applied is trapped and retained in the molten particles. These gas-trapped pores will remain and decrease the densities of printed components, which are detrimental to the mechanical properties of printed components, especially fatigue properties [19].

Metal materials used for AM include iron-based alloys, nickel-based alloys, aluminium-based alloys, and titanium-based alloys [42]. Iron-based alloys are rich in resources, which are widely used in industrial production and life. They can be subdivided into three categories: stainless steel, high-strength steel, and die steel; 304 and 316 austenitic stainless steel powders [36]. However, these alloys are not suitable for certain application because of, for instance, their insufficient wear resistance [3]. While tool steels with high content of carbon (>0,4 wt.-%), which is the case of AISI S2 tool steel used in this present study, might be a more advanced solution. Nevertheless they are considered as unweldable due to the brittle martensitic phase that forms in AM out-of-equilibrium conditions [3], [4], more recently there have been successfully applied to AM technology several researches showing how to mitigate these problematics [1], [3], [5], [6].

### 2.2.1 Low-alloy Steel

Steel is a critical material for modern society. It is by far the most produced type of structural metallic alloy, about 30 times more in weight than the second-ranking aluminium alloys [43]. Moreover, steel holds a key role in addressing two of the most pressing challenges faced today: climate change and natural resource exhaustion. It is ideally suited for numerous transportation and energy applications given the abundance and the even distribution of most of its base minerals. Its other key advantage is its unmatched versatility, as subtle tuning of its composition and its thermomechanical processing that can yield a wide range of microstructures and corresponding mechanical properties [44].

Most common steels are usually carbon steels with the addition of one or several alloy elements to improve their properties quality. A big section of the steel is occupied by low-alloy steels, in which the total alloy elements content is less than 5%. This type is the case of AISI S2 tool steel which was utilized in the current study.

Commercial low-alloy steel grades commonly include four or more alloying elements from about a dozen usual ones (B, C, N, Al, Si, Ti, V, Cr, Mn, Ni, Cu, Nb, Mo, W...), resulting in a many dimension design space. Designing enhanced-recyclability grades involves an even more complex space as trace elements from scrap metal must be accounted for as well [45]. The yield stress of steel determines how big stress that steel can suffer and does not cause any deformation, for low-alloy steel is at the range of 310-345 MPa. Regarding corrosion properties, some low-alloy steel has great inoxidizability and the presence of copper, phosphorus, silicon, chromium, nickel, molybdenum can raise the corrosion resistance.

Low-alloy steel has great technological properties such as machinability, cold and hot processing properties and heat treatment properties. Low-alloy steel can indeed make a huge impact on the development of one material, thus the size, weight, properties and etc of industry products can be improved [46]. It is widely used in the industries as the engineering plant, ships, bridges, buildings, automobiles and etc.

However, low-alloy steels present specific challenges regarding welding and fabrication. The complexity of the weldability is as varied as the alloy steel composition and its application [47]. With increasing carbon or alloy content, low-alloy steels generally become more difficult to weld as the heat affected zone hardness increases [48]. Generally, in welding processes, localized concentrated heat is applied to melt and join the work pieces together. Due to the rapid heating and cooling cycles, the work piece is subjected to steep temperature gradients that lead to microstructural changes in the welded areas, followed by residual stresses and deformations in the welded components [49]. It becomes a safety critical issue when a welded steel component

undergoes fatigue environment. This is because, the fatigue strength of the weldment is related to that of the heat affected zone. It has been reported that ~ 80% of mechanical failures are fatigue related [50]. One of the major factors that deteriorate this property of welded joints is residual stress. The combined effects of defects and residual stress contribute significantly to the limit of load that can be imposed on the structural member.

Although the unpromising weldability of such steels, an increasing interest on low-alloy carbon steel for additive manufacturing has been developed within the last years. The reasons lay into the broadening of AM application fields by using different kinds of materials. However, compared to classical processes of PM, 3D printed alloy steels were found so far to have poor mechanical properties [7]. One reason is the hard brittle martensite phase which the high carbon content tends to generate. Moreover, carbon is prone to react with oxygen in the laser molten pool, forming carbon monoxide and dioxide gas bubbles and latter phenomenon leads to not only the loss of C but most-likely also to the generation of pores in the fabricated alloy steels.

Regarding the powder production of low-alloy steel additive manufacturing, gas atomized and plasma atomized (PA) powders are commonly used in LPBF due to their chemical purity and near-spherical shape, which enables easier material distribution over the powder bed for laser processing [51].

While studying as-built additive manufactured low-alloy steels, it is important to take into account the fact that the microstructure is very sensitive to the influence of heat. After solidification, austenite, pearlite, bainite, and martensite may form under different cooling conditions. These microstructures also undergo phase transformation when heated and so tempered martensite, recrystallized ferrite, tempered bainite and tempered sorbite may form at different heating temperatures [52]. Indeed, as-built samples were found to show microstructure with alternate layers of untempered (hard) and tempered (soft) martensite, as the result of the multiple thermal cycling effects [1].

Hence, to fabricate and characterize low-alloy steel parts generated through SLM, a big effort to mitigate the issues due to the presence of defects and to investigate the microstructure is needed.

## **2.3 Microstructural characterization**

The current study aimed to face the challenges of printing low-alloy steels above mentioned and analysing as many aspects of the as-printed 3D parts as possible. One goal was to be able to analyse the supersaturated phases of low-alloyed steels together with the complex thermal history typical of SLM printed pieces. To do so, a microstructural investigation has been

performed using several common and others innovative techniques.

To begin with, it is important to consider that the AM process is characterized by high cooling rates that bring to a fine structure. The laser processes lead to solidification in metals that is more cellular dendritic instead of the classical columnar dendritic owned by the casting routes as Y. Lee et al. [53] reported (Figure 15).

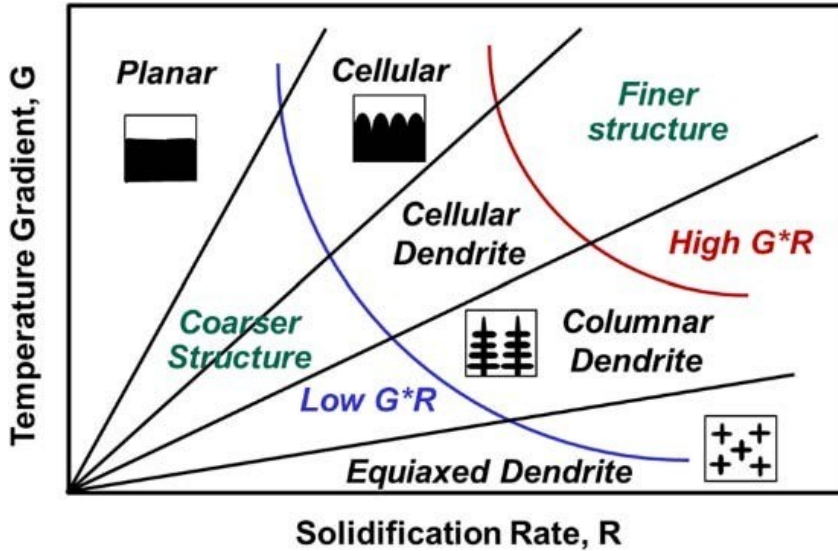


Figure 15: Correlation between Temperature gradient ( $G$ ), Solidification rate ( $R$ ) and the microstructure [53].

Moreover, as in SLM the 3D part is fabricated layer by layer, the changes of temperature field during the process as well as the heat input and heat accumulation have a significant impact on the microstructure, resulting in a complex final microstructure. The phase transformations associated with the thermal cycling process are affected by the input parameters (Figure 16, Figure 17). Thus, different microstructures are finally obtained at different values of volumetric energy density ( $E_d$ ) [52], gaining a big anisotropy and inhomogeneity and, as consequences, the mechanical properties of the final parts are affected.

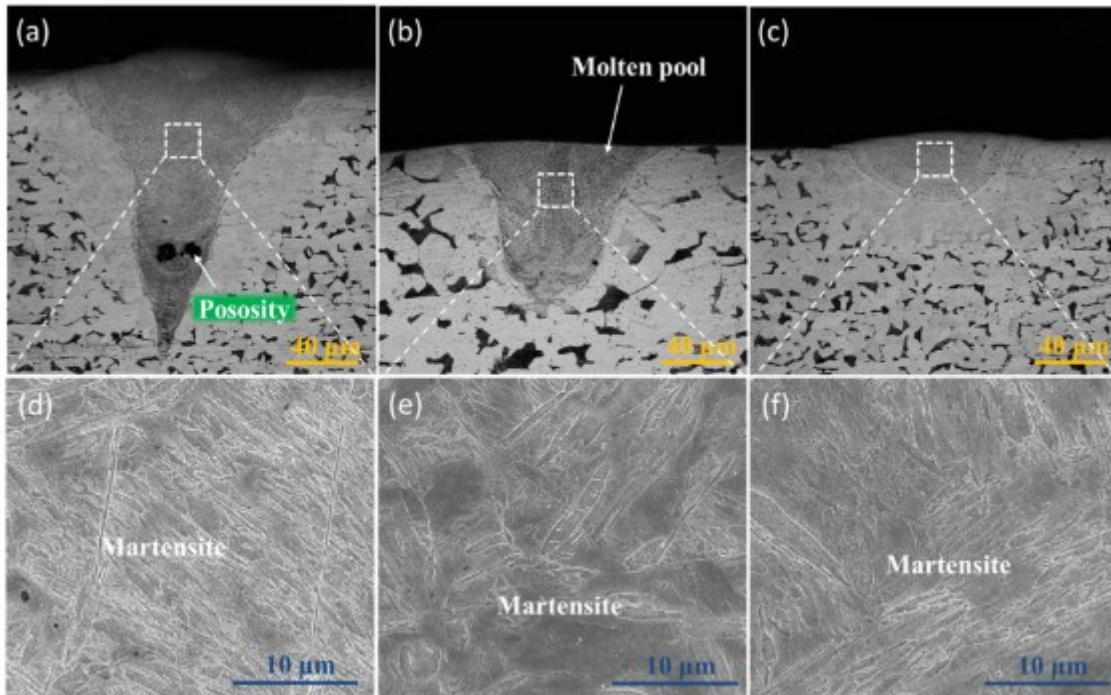


Figure 16: Molten pool morphologies and corresponding microstructural SEM images of SLM low-alloy steel samples grown with different  $E_d$ s: (a,d)  $E_d=284 \text{ J/mm}^2$ ; (b,e)  $E_d=71 \text{ J/mm}^2$ ; (c,f)  $E_d=29 \text{ J/mm}^2$  [52].

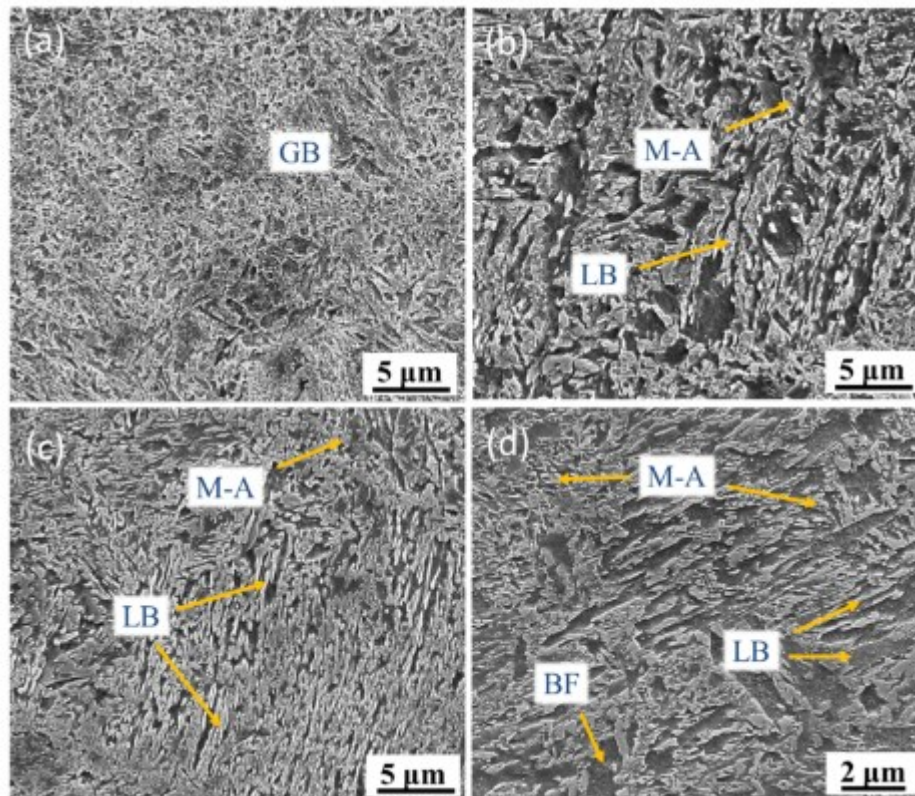


Figure 17: Microstructures of SLM low-alloy steel samples grown with different  $E_d$  s: (a)  $E_d=142 \text{ J/mm}^2$ ; (b)  $E_d=71 \text{ J/mm}^2$ ; (c)  $E_d=47 \text{ J/mm}^2$ ; and (d) zoomed-in image of (b). GB: granular bainite; M-A: martensite-austenite; LB: lower bainite; BF: bainitic ferrite [52].

Recent studies already aimed to characterize low-alloy steels produced by AM techniques. For instance, Liu et al. [54] investigated the microstructure evolution of 3D printed pieces finding that the as-deposited microstructure of the as-deposited samples is mainly the mixture of martensite and acicular bainite (Figure 18). To do so, OM and SEM observations have been performed, together with microhardness tests. From the SEM photos, the study observed that martensite is composed of many laths that are roughly parallel to each other. This has been found as a typical microstructure features of the additive manufactured low alloy steel parts [55], [56]. In the latter explained work the hardness evaluation was not used to evaluate the mechanical properties of the printed specimen, it was instead used to help the characterization of the phases. Indeed, different values of hardness can be correlated to different microstructural phases. This innovative technique will be utilized in this present study as well.

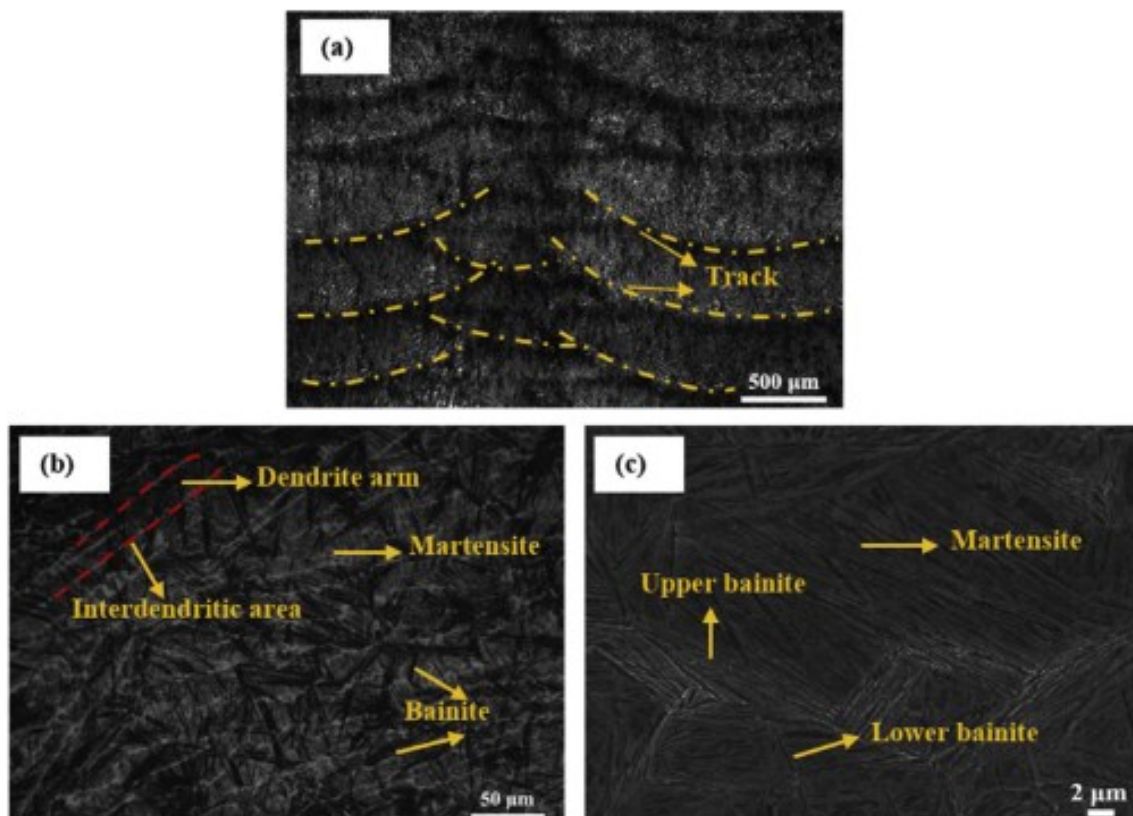


Figure 18: Microstructure of the as-deposited parts: (a) Low magnification image; (b) high magnification image; (c) SEM photo [57].

Other studies, such as Saewe et al. [58], investigated the solidification structure of the top layer of the specimen. Thanks to the use of OM and SEM observations, together with EBSD

and EDS analysis, they found both columnar dendritic structure close to melt pool boundaries and equiaxed structure in the centre of the melt pool. In particular, the cross-consideration of Energy dispersive X-ray (EDS) analysis (composition) and Electron Backscattered Diffraction (EBSD) analysis (information about lattice) appears as very promising to overcome the limitations specific to each of these techniques considered separately [59]. Their outcomes showed that dendrites are created by the rapid solidification and strong constitutional supercooling of the melt during the process, while the areas with an apparently equiaxed solidification structure in the middle of the melt pool may be caused by a locally reduced temperature gradient [58]. This sub-grain structure was found to be characterized by very fine dendrites and interdendritic areas (Figure 19). The equiaxed solidification structure is shown representatively in Figure 19d, where equiaxial precipitates are visible along interdendritic regions.

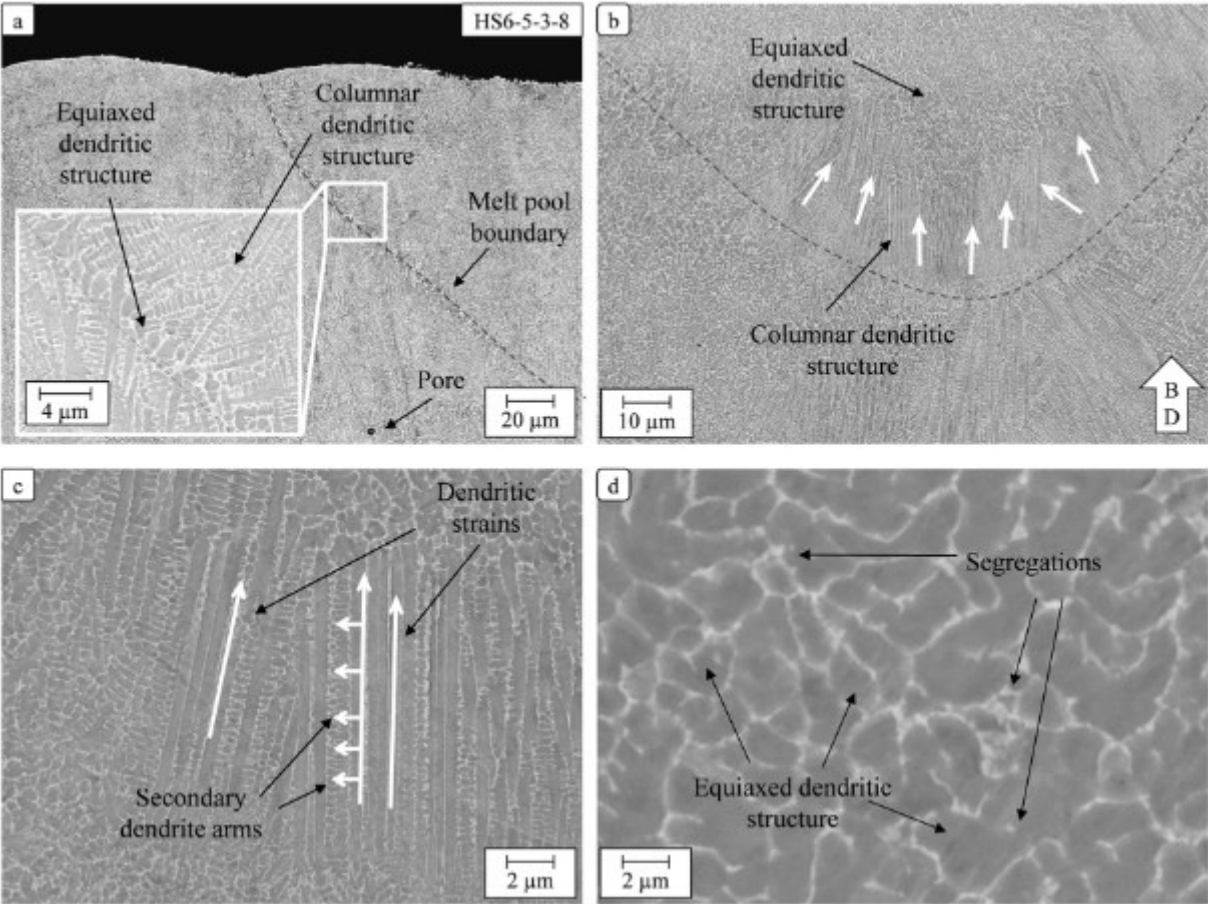


Figure 19: SEM micrographs of a melt pool (a-b) and details of columnar dendritic (c) and equiaxed dendritic solidification structures (d) at the top layer of as-built samples [58].

Moreover, Pham et al. [25] used again microscope observations together with EBSD and EDS analysis to show that perturbations on the sides of cells (or dendrites) facilitate crystals to change growing direction by side-branching along orthogonal directions in response to

changes in local heat flux. While the continuous epitaxial growth is responsible for slender columnar grains confined to the centreline of melt pools, side-branching frequently happening on the sides of melt pools enables crystals to follow drastic changes in thermal gradient across adjacent melt pools, resulting in substantial broadening of grains [25]. Furthermore, the study found that the variation of the scan strategy could interrupt the vertical columnar microstructure, but promote both in-layer and out-of-layer side-branching.

Another unique technique which has been used to achieve information about the microstructure of AM metal parts is the reverse differential thermal analysis. The latter consists in a common Differential Thermal Analysis (DTA) test which is carried out at a moderate and constant heating scan speed until complete remelting. However, the outcomes of the analysis are used to allow linking each of the endothermic or exothermic reactions peaks observed in the DTA curve to a related phase transformation that had occurred during the initial solidification in the spin-casting process [59]. Nevertheless the very high achievable cooling rates ( $50^{\circ}\text{C}/\text{min}$ ), these remain several orders of magnitude lower than those achieved under industrial casting processes. DTA is thus useful to build phase diagrams, in equilibrium conditions or close to equilibrium, however, because the cooling rate strongly influences both undercooling and solute partitioning during solidification, the crystallization behaviour achieved under DTA hardly corresponds to the actual solidification sequence which occurs during industrial casting processes [59]. Indeed, subsequently the reverse DTA, if combined to other microstructure investigation technique such as SEM/EDS–EBSD, constitutes in an innovative relevant approach to understand the phase transformations during complex casting processes with relatively high solidification [59].



# 3. MATERIALS AND EXPERIMENTAL METHODS

## 3.1 Original Powders

The powders used to create the samples are gas-atomized AISI S2 powders, supplied by Sandvik Osprey Ltd., U.K.. In Figure 20 their morphology and in Table 3 their chemical composition is shown.

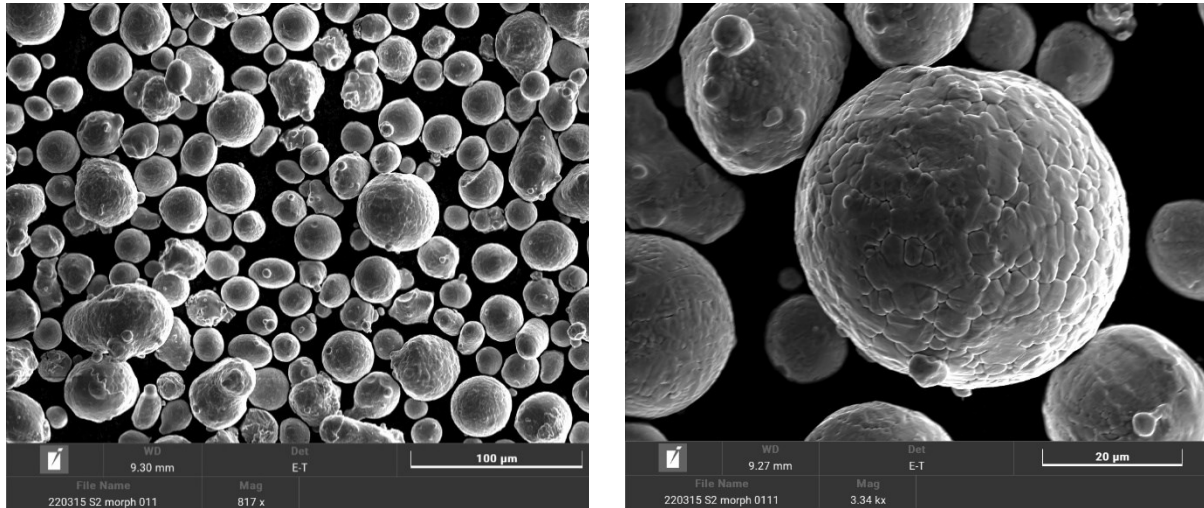


Figure 20: SEM micrographs of the S2 powders.

<b>Element</b>	<b>C</b>	<b>Si</b>	<b>Mo</b>	<b>Mn</b>	<b>Fe</b>
<b>%wt</b>	0,49	1,2	0,6	0,6	Bal.

Table 3: Chemical composition analysis of the S2 powders.

The particles size in the S2 powder varies, the Laser Diffraction Analysis reveals a D10 value of 20,6 µm, D50 value of 31,0 µm and a D90 value of 47,5 µm. Moreover, AISI S2 steel powders have an apparent density of 7,806 gr/cm<sup>3</sup>.

## 3.2 Samples fabrication

The additive manufacturing technique utilized to fabricate the samples was Selective Laser Melting (SLM). The samples have been produced by the company “Aconity 3D” and the machine used was the AconityMIDI.

### 3.2.1 SLM Machine

The Aconity Midi machine is displayed in Figure 21. It represents Aconity3D's approach towards a flexible production system equipped with process monitoring and high temperature preheating up to 1200°C. This machine has also an optional second process chamber, which

allows parallelizing setup times while the main system is still producing [60]. As for all Aconity systems, the Aconity Midi is equipped with the control software Aconity Studio which allows to have access to all relevant process parameters and machine components. The Aconity Midi is also available as Dual-Laser system for further maximized productivity. Additionally, it may be equipped with the unique vacuum option and Micro-SLM configuration [60].

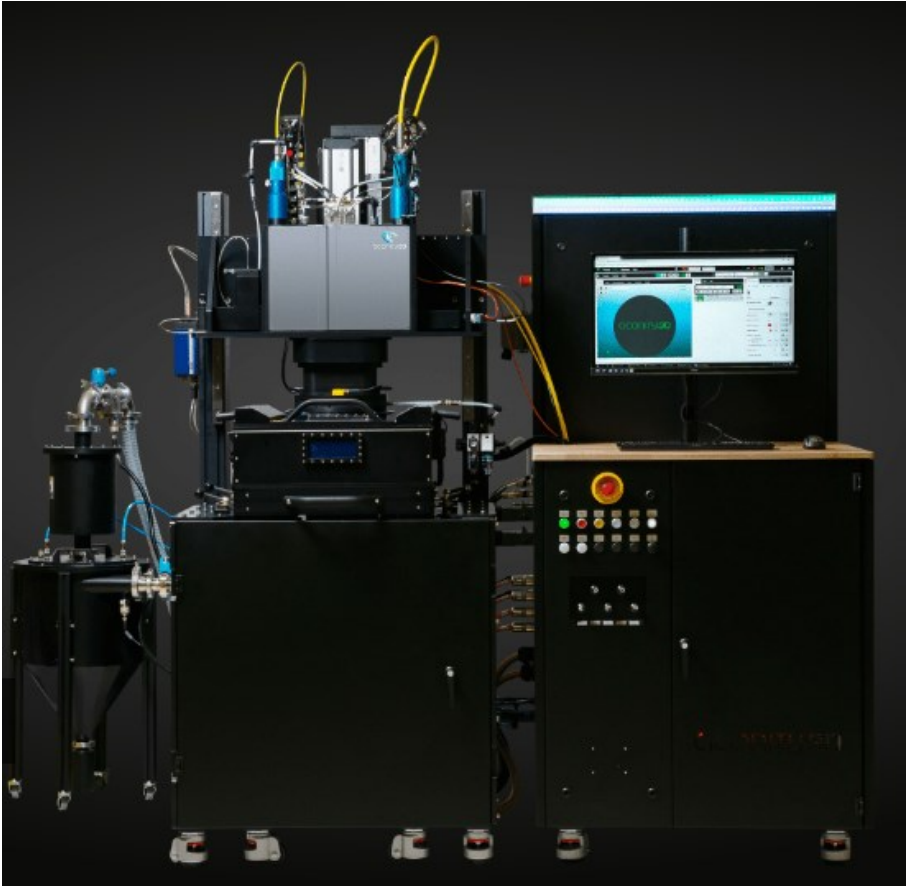


Figure 21: AconityMIDI SLM Machine [60]

This Selective Laser Melting machine has many attributes, its main technical specifications are explained in Table 4.

Build Space	Diameter of 170 mm Height of 250 mm
Optional Build Spec reduction	Diameter of 100 mm x height of 250 mm Diameter of 55 mm x height of 250 mm
Laser configuration	Single Mode Fibre 400W / 1000W

Optics configuration/ Spot size	F-Theta/ 80 micron 3D Scanning/ 80-500 micron
Preheating Temperature/ Heated Area	500°C/ Diameter of 170 mm x Height of 180 mm 800°C/ Diameter of 100 mm x Height of 180 mm 1200°C/ Diameter of 70 mm x Height of 150 mm
Fully adaptable process parameters	Maximum flexibility for application development
Layer Thickness	Down to 10 micron
Inert gas Type/ Pressure	Argon 4.6/ 6 bar Nitrogen/ 1 mbar
Optional inertization system	Vacuum/ 1 mbar
Optional Additional build chamber and setup station	Parallelized machine setup
Inert Gas Consumption	<5 lt / min during processing <30 lt /min during plugging
Residual Oxygen content	<100 ppm
Pressurized air Type/ Pressure	ISO 8573-1:2010 [1:4:1]/ 6 bar
Pressure Air Consumption	< 50 lt/min
Machine dimensions (width x depth x height)	2170 mm x 1590 mm x 2340 mm
Machine weight without powder	1385 kg

Table 4: Technical specifications of Aconity Midi [60].

### 3.2.2 Parameters for the realization of the samples

Twenty samples have been built using different processing parameters as listed in Table 5. The laser spot size used was of 80  $\mu\text{m}$  with a Gaussian laser distribution for all the built samples and the layer thickness was set at 30  $\mu\text{m}$  for all the cubes. The scanning strategy that was used was of 90°/90°, hence rotating the laser orthogonally after each layer deposition, as displayed in Figure 22 [61].

<i>Sample</i>	<i>Laser Power [W]</i>	<i>Laser Scan Speed [mm/s]</i>	<i>Volumetric Energy Density [J/mm<sup>3</sup>]</i>
1	100	400	104,2
2	100	600	69,44
3	100	800	52,08

4	100	1000	41,67
5	100	1200	34,72
6	150	500	125,0
7	150	750	83,33
8	150	1000	62,50
9	150	1250	50,00
10	150	1500	41,67
11	200	500	166,7
12	200	750	111,1
13	200	1000	83,33
14	200	1500	55,56
15	200	2000	41,67
16	250	500	208,3
17	250	750	138,9
18	250	1000	104,2
19	250	1500	69,44
20	250	2000	52,08

Table 5: List of process parameters used for the samples fabrication. In red the samples that could not be fully printed.

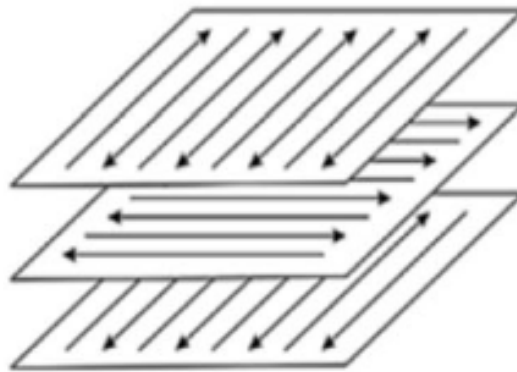


Figure 22: Scanner Strategy of 90°/90° [61].

The samples used for this work are showed in Figure 23. The pieces have cubic shape and their dimension is of 1 cm<sup>3</sup> (10 x 10 x 10 mm). Among them, five could not be used for the analysis since they were not fully printed. Therefore a total amount of 15 samples were studied, each one was used for the microstructural characterization, while only four of them were selected for the Differential Thermal Analysis, Differential scanning calorimetry and the Hardness tests. Moreover, profilometer observations were carried out on all the fifteen samples.

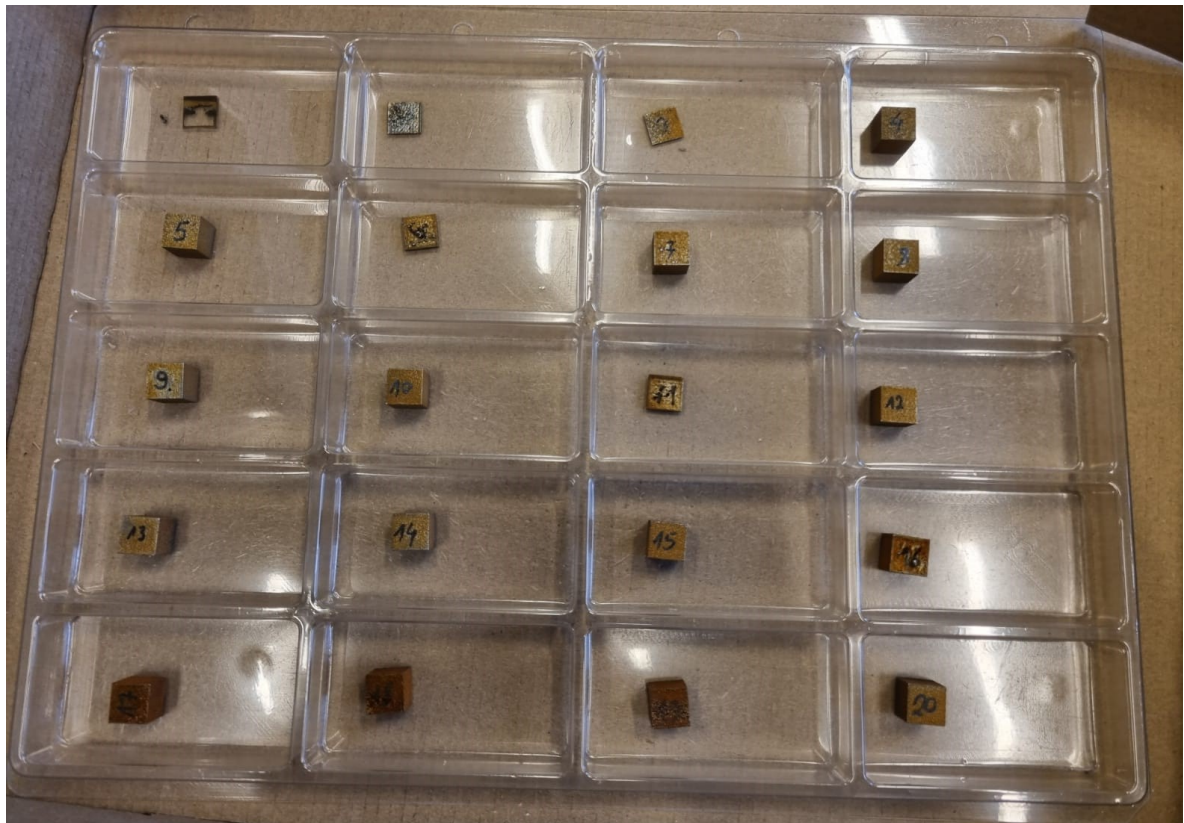


Figure 23: Samples used in this work. a) one of the six samples that could not be fully printed; b) the three selected samples used for further characterization.

### 3.3 Microstructural Characterization

Further characterization concerning the microstructure was held using both Optical Microscope (OM) and Scanning Electron Microscope (SEM) combined with Electron Backscatter Diffraction (EBSD). For all the samples, the internal cross-section at mid-thickness that is parallel to the building direction was considered.

#### 3.3.1 Samples preparation

All the as-built samples were cut by Spark Erosion Machine to obtain parallelepiped shape samples (Figure 24a) for thermal analyses or different cross-sections available for the microstructural characterization.

In the case of thermal analysis such as Differential thermal Analysis (DTA), precise

dimensions are required for the samples to appropriately fill the crucible. For the latter reason, from the parallelepipedal cut samples of 10 mm height (Figure 24a), smaller pieces of 9 mm height and 3 mm width (Figure 24b) were extracted via electro erosion, eliminating the substrate.

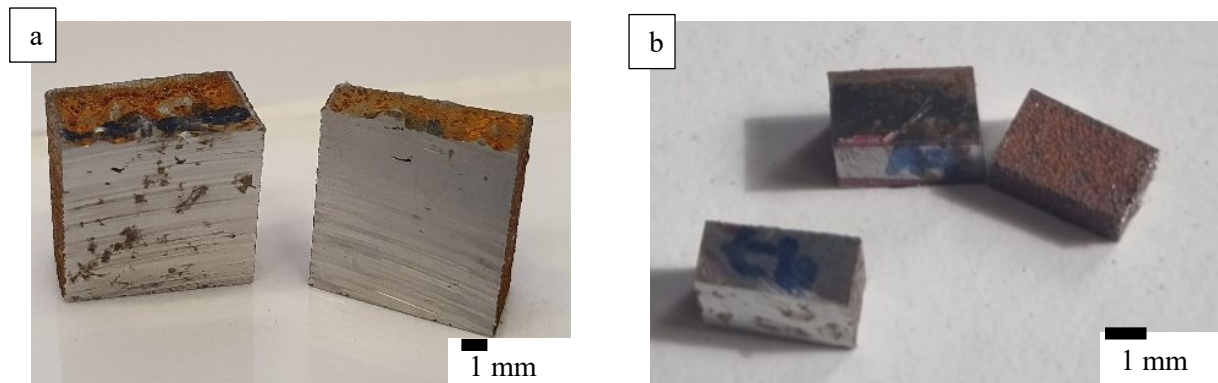


Figure 24: Cutting of the samples a) for the Microscope Observations; b) for the DTA Analysis.

The samples needed a preliminary preparation to achieve mirror-like sections that help to check for both internal and surface defects using optical microscope and electron microscope. As-polished samples were also used for the analysis of Vickers hardness and nanoindentation. Therefore all the cut sections were hot-mounted and polished down to 1  $\mu\text{m}$ .

Firstly, they were embedded in a bakelite cylinder using a Struers Citopress-1 (Figure 25) [62]. The bakelite cylinder is obtained by pressing at high temperature the bakelite powder, which then allows the polymerization. After embedding the samples in the phenolic resin, they were polished down to 1  $\mu\text{m}$  using a Struers Tegramin-30. This latest process is required to obtain a clean and plane surface. Indeed, a plane surface is necessary for the microscope analysis. The Struers Tegramin-30 owns a disc of 300 mm of diameter. The polishing process consists in circular movements of the samples on a wear paper using also lubricant liquid. Finally, the samples have been treated with an Oxide Polishing Suspension (OPS), that is composed of colloidal silica, as super finishing preparation for EBSD analyses under SEM to identify phases from their crystal lattices.

The cut sections were prepared with different techniques. For specific uses the OPS was held for 5 or 20 minutes. Moreover, in order to observe the differences among the microstructure's phases, an etching of 3% Nital was applied on some of the samples as well.

*STRUERS Citopress-1*

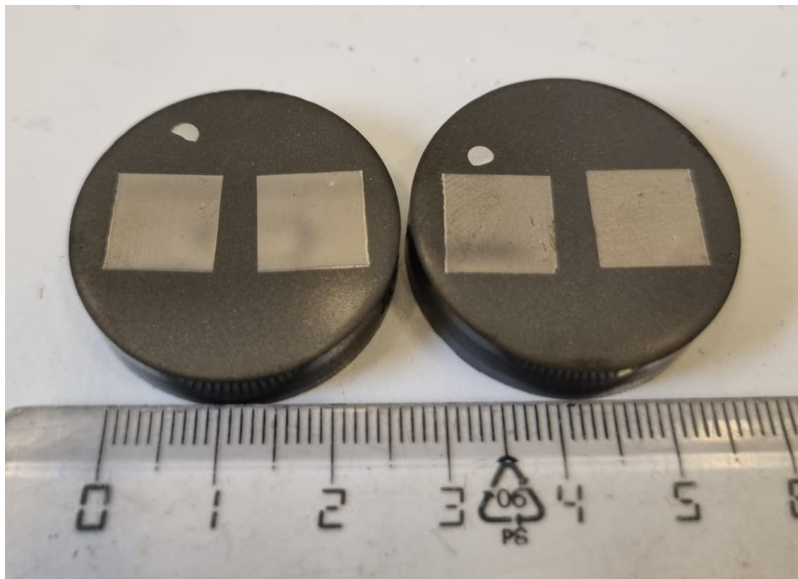


*STRUERS Tegramin-30*



*Figure 25: STRUERS equipment [62].*

In Figure 26 are visible the samples after all the steps of the preparation.



*Figure 26: Samples after preparation.*

### **3.3.2 Optical Microscope (OM) and Stream Analysis Software**

Optical Microscope observations were performed on all the cut sections with an Olympus BX60 Microscope (Figure 27) [63]. Analyses were done at magnifications of 2.5x, 5x, 10x and 20x. Overviews of the entire cross-section were obtained at 2.5x magnification.



*Figure 27: Olympus BX60 [63].*

The Stream Analyse Software was used to analyse the overviews obtained from the Optical Microscope and to assess samples porosity. In this study, the software was utilized to calculate the percentage of porosity of the cross-section, together with the investigation of the dimensions and the distribution of the pores present in the samples. Indeed, the overviews were processed to understand the position of the particles in the deposit, along Y direction, where Y represents the direction parallel to the building direction of the “as built” sample. Moreover, the results that were computed were used to compare the different medium values of the particle size distribution (D50) among the samples and therefore to investigate about the dimensions of the pores.

### **3.3.3 Scanning Electron Microscope (SEM)**

Observations were carried out with a Tescan Clara Ultra-High Resolution (UHR) SEM displayed in Figure 28 [64] in order to observe better the cross-sections of the cut samples thanks to the higher resolution of the machine.

In the case of using this microscope, an additional sample preparation was required. Therefore the samples that were examined were treated with a silver painting to bond the real sample with the bottom of it (resin part) [Figure 29].





*Figure 28: Tescan Clara Ultra-High Resolution [64]*



*Figure 29: Samples after preparation with silver paint.*

Selected profiles and specific points' composition were obtained with EDS (Energy Dispersive Spectrometry) to better understand the chemical composition of different zones in the cross-section.

Moreover, EBSD (Electron Back Scattered Diffraction) was used to recognize the different crystallographic lattices of the different zones. In this case silver painting is required to enhance the evacuation of electrical charges during EBSD analysis. For this observation, the samples were placed on a special support, to ensure that the sample does not move when it is tilted to an angle of  $70^\circ$ .

### 3.4 Profilometer Analysis

The Alicona InfiniteFocus G5 that is shown in Figure 30 was used to analyse the top surface of each as-built samples. This machine uses a non-contact, optical, three-dimensional measurement principle based on Focus-Variation. The main component of the system is a precision optics containing various lens systems that can be equipped with different objectives, allowing measurements with different resolution [65]. The instrument objectives magnification is up to 100x. This machine allows to perform 3D images that very well show the surface parts, as well as being capable of measuring depth of the valleys which were visual. This way one image of the top surface of each sample was taken in order to compare the different surface qualities.



*Figure 30: Alicona InfiniteFocus G5 profilometer [65].*

### 3.5 Thermo-Physical Analysis

The samples have been characterized in terms of their thermal and physical properties. The density was computed as one of the aims of the project was to print fully dense metal parts. In the case of the DTA, it was used to perform the solidification sequence of the pieces during the process. Moreover, several isothermal heat treatment were performed using the DTA technique in order to obtain better results during the EBSD analysis.

#### 3.5.1 Density Measurements with the Pycnometer

As in this study it is the most important physical property, the density of each as-built

bulk sample (1 x 1 x 1 cm) is computed. To do so, an AccuPyc II Serie 1345 Pycnometer (Gas pycnometer) was used (Figure 31) [66]. Once the experiment is initiated, 10 measurements on each sample are performed, and every time the density of the material is displayed.



Figure 31: AccuPyc II Serie 1345 Pycnometer [66].

Gas pycnometry is recognized as one of the most reliable techniques for obtaining true apparent volume and density. This non-destructive technique utilizes the gas displacement method to measure the volume of a material. Density determinations from the gas displacement method are more accurate, reproducible, and faster than the traditional Archimedes water displacement method [66].

### 3.5.2 Differential thermal Analysis (DTA)

The DTA tests were performed with a NETZCH STA 449C Jupiter DTA (Figure 32) [67] following standard DIN 51 007. There were performed several tests on the optimum sample (Sample 13) in his as-built conditions after being properly cut (section 3.3.1). One up to 1500°C to use as “reverse” DTA and obtain an idea of the solidification sequence which occurred during the process. DTA was indeed used to investigate the possible solid state transformation during heating of the cut parallelepiped samples. It is important to notice that the scanning speed used during the DTA tests (5°C/min for the heating and 20°C/min for the cooling) is many times lower than the steep thermal gradients achieved during SLM process. This device can observe the mass changes, oxidation/reduction behaviour, decomposition and corrosion studies. It can operate under a high vacuum or under protective atmosphere [67]. The difference of temperature between the sample and the standard is measured by means of thermocouples and expressed in

$\mu\text{V}$  (thermal voltage). When several peaks are overlapped in the same temperature range, a deconvolution allows to distinguish these peaks, [68].



*Figure 32: NETZCH STA 449C Jupiter for DTA tests[67].*

DTA technique was used to perform isothermal heat treatment tests on the selected cut sample (sample 13) as well. The different parameters of the treatments are listed in Table 6. The isothermal treatments were performed until 300, 600 and 900°C with 1h of holding time. The latter tests were used as a stress-relief treatment to the piece. The aim was to reach a deeper understanding on the microstructure, looking at the different transformations of phases which occurred under different heating treatments. Moreover, they were used to gain better results at the EBSD analysis thanks to the less oversaturated microstructures produced.

Sample	Heating Rate [°C/min]	Range Temperature [°C]	Isothermal for 1h	Cooling Rate [°C/min]
13	5	25-1550		20
13	5	25-300	X	20
13	5	25-600	X	20
13	5	25-900	X	20

Table 6: DTA Test parameters.

After thermal analyses, the microstructures of the samples have been observed, following same procedure as for the “as built” samples. Indeed, direct observations with SEM through Secondary Electrons (SE) and EDS analyses were carried out.

### 3.6 Hardness Tests

Macro and nanohardness tests were performed on the same cross-sections of three selected samples.

#### 3.6.1 Macrohardness Test

Hardness indentation were performed on the selected samples, using EMCO MIC 010 (Figure 33) [69]. This machine is considered a digital low-load hardness testing machine. DIN EN ISO, ASTM E- 92 HV 30 were used in this study. The hardness tester is equipped with an automatic tool which permits the exchange of lens and indenter, fully automatic test cycle, automatic lens focusing, leading-edge high- resolution CCD camera, fully automatic image evaluation and manual cross slide.



Figure 33: EMCO MIC 010 [69].

In this work the location of each indentation was set manually. It was obtained an indentation grid (Figure 34) on the left side of the cross-section of each sample, where every mark was 0,4 mm aside of the following one. The aim was to reach a complete macrohardness characterization of the sample tested. Indeed, afterwards, it was possible to calculate the hardness value, in Vickers scale, by measuring the distances between the rhombus edges with an appropriate software for the image analysis, ecos010/image.

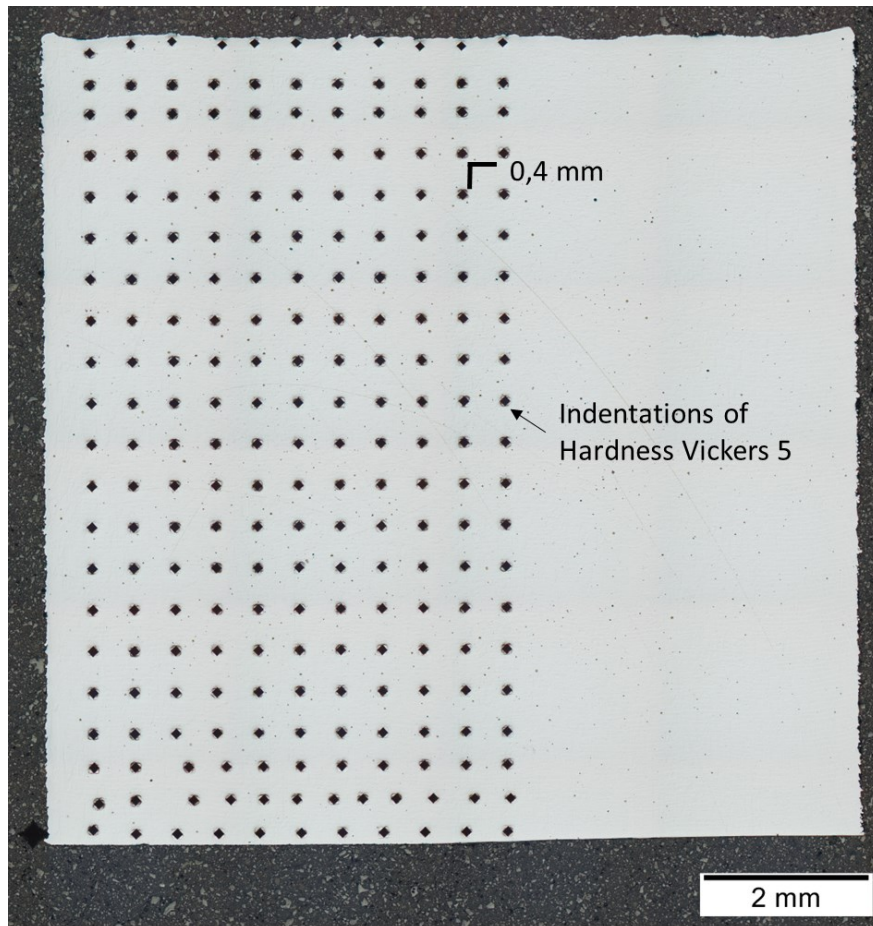


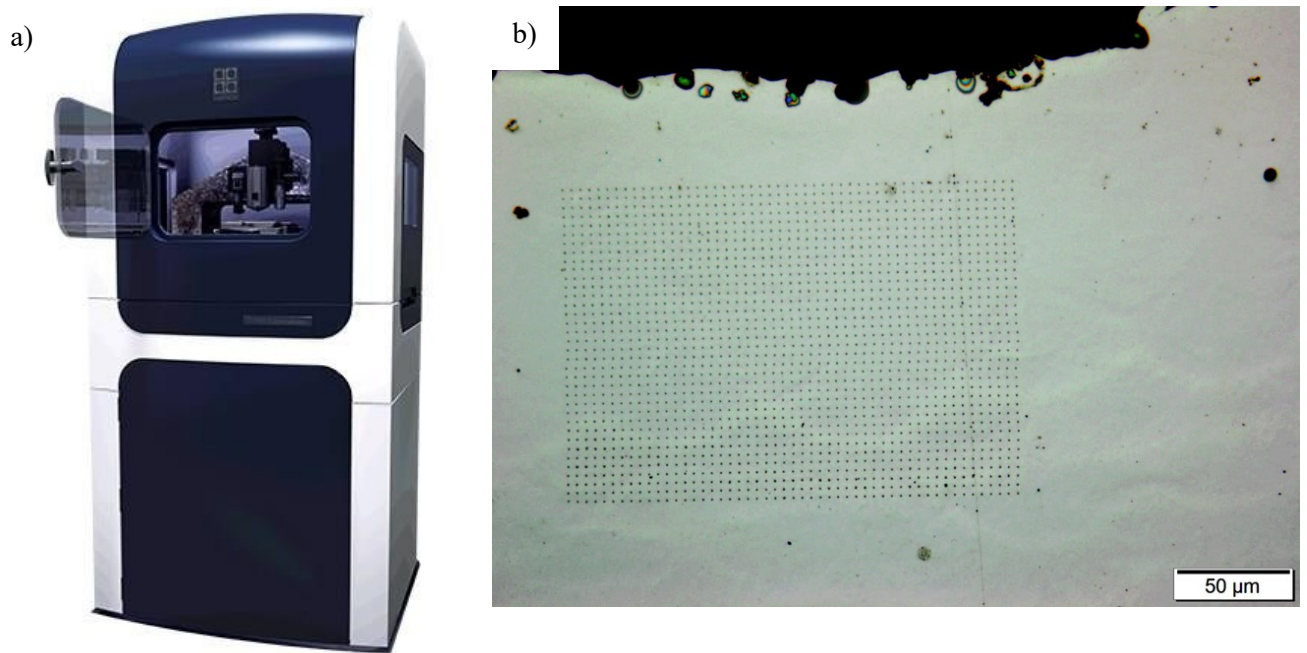
Figure 34: OM micrograph showing the macrohardness indentation grid.

### 3.6.2 Nanohardness Test

The nanohardness was evaluated with a TI 950 Triboindenter nanoindenter by Hysitron (Figure 35a) [70]. The machine works in two modes: load control modality and displacement control modality.

Nanohardness indentation grids ( $200 \times 200 \mu\text{m}^2$ ), as shown in Figure 35b, were carried out in order to understand the nanohardness evolution in different part of the cross-section. A controlled displacement equal to 150 nm using a Berkovich indenter tip on a low load transducer was used. The load was continuously monitored. A minimum distance of 4  $\mu\text{m}$  was maintained

between the indents to avoid overlapping of their affected volumes. The data then generates a “Force-Displacement” curve, which can give a mechanical fingerprint of the sample’s properties.



*Figure 35: (a) TI 950 Triboindenter by Hysitron [70] and (b) OM micrograph showing the nanohardness indentation grid.*

## 4. RESULTS

### 4.1 Pycnometer density evaluation

Thanks to the use of the pycnometer, it was possible to obtain the density values of each fully printed sample. These values were very useful for the creation of the process map since they give a very important indication of the quality of the 3D printed parts.

Comparing the values obtained ( $\rho$ ) with the density of AISI S2 (Annex), which is 7,806 gr/cm<sup>3</sup> ( $\rho_{bulk}$ ), the percentage of density was computed as follow:

$$\% \text{ Density} = \frac{\rho \cdot 100}{\rho_{bulk}} \quad \text{Equation 2}$$

All the specimens were found to have a percentage of density above 96% (Table 7). In Figure 36, the correlation between the volumetric energy density values of the printed pieces and the percentages of density is displayed.

<i>Sample</i>	<i>Density (gr/cm<sup>3</sup>)</i>	<i>% Density</i>
04	7,53882	96,577
05	7,57492	97,040
07	7,75504	99,347
08	7,77464	99,598
09	7,76741	99,506
10	7,76303	99,450
12	7,77855	99,648
13	7,76336	99,454
14	7,75002	99,283
15	7,69372	98,562
16	7,76562	99,483
17	7,78430	99,722
18	7,79693	99,884
19	7,74477	99,216
20	7,65605	98,079

*Table 7: Density and percentage of density values for each fully printed sample computed.*



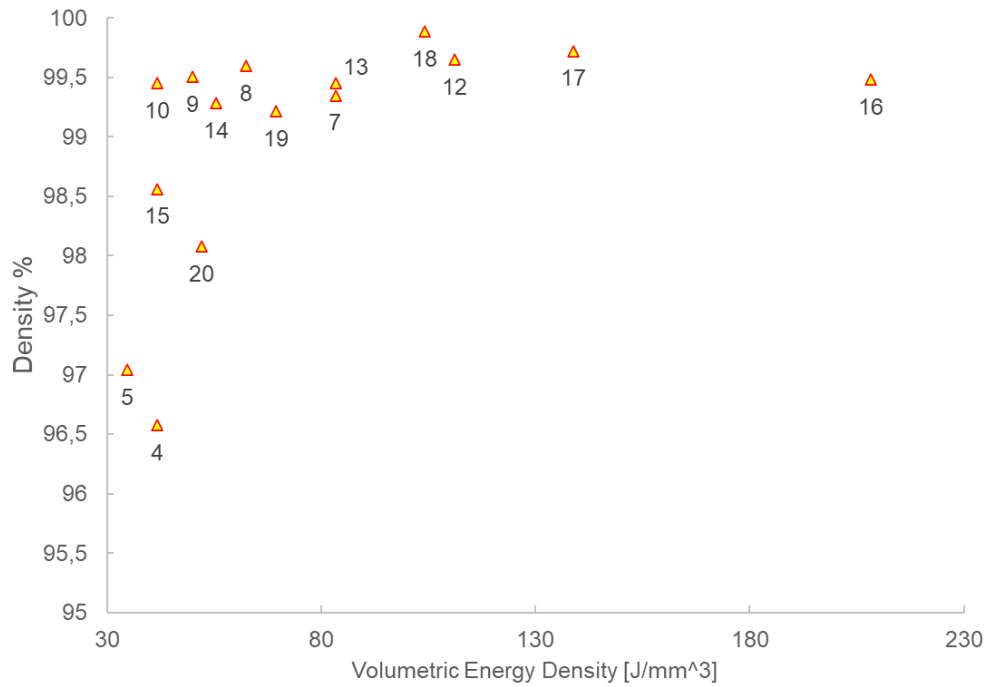


Figure 36: Graphical correlation between  $E_d$  values and percentages of density of all the fully printed as-built samples.

## 4.2 Surface Characterization

Using the profilometer, the surface quality of all the samples was evaluated. The surface quality of the pieces could be correlated to the process parameters values, as shown in Figure 37.

The specimen created using a high  $E_d$  (Figure 38e), exhibited large spatter particles distributed along the surface. While in the samples with low  $E_d$  together with high laser scanner speed (above 1250 mm/s) and low laser power (below 150 W), a lot of irregularities were detected (Figure 38a). These irregularities were mainly short peaks and valleys in a sizeable quantity, enhancing the surface roughness. The selected pieces (Figure 38b,c,d) for which hardness tests and microstructure investigation were held, showed a low presence of the two events. Therefore, they were to have a better surface quality. These pieces had a medium value of  $E_d$  and medium values of laser power and laser scanner speed.

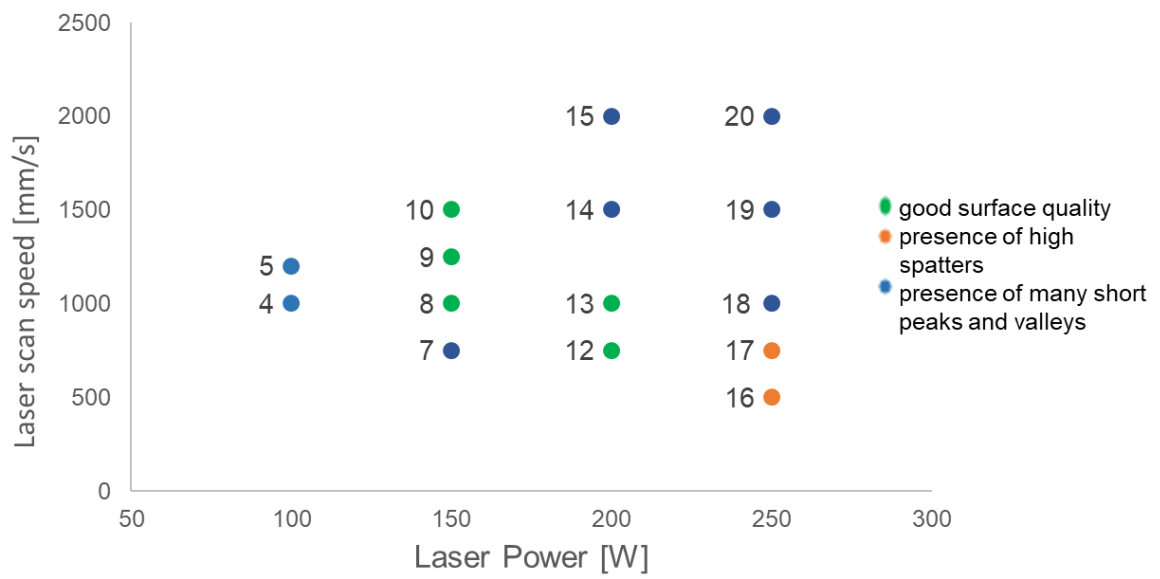
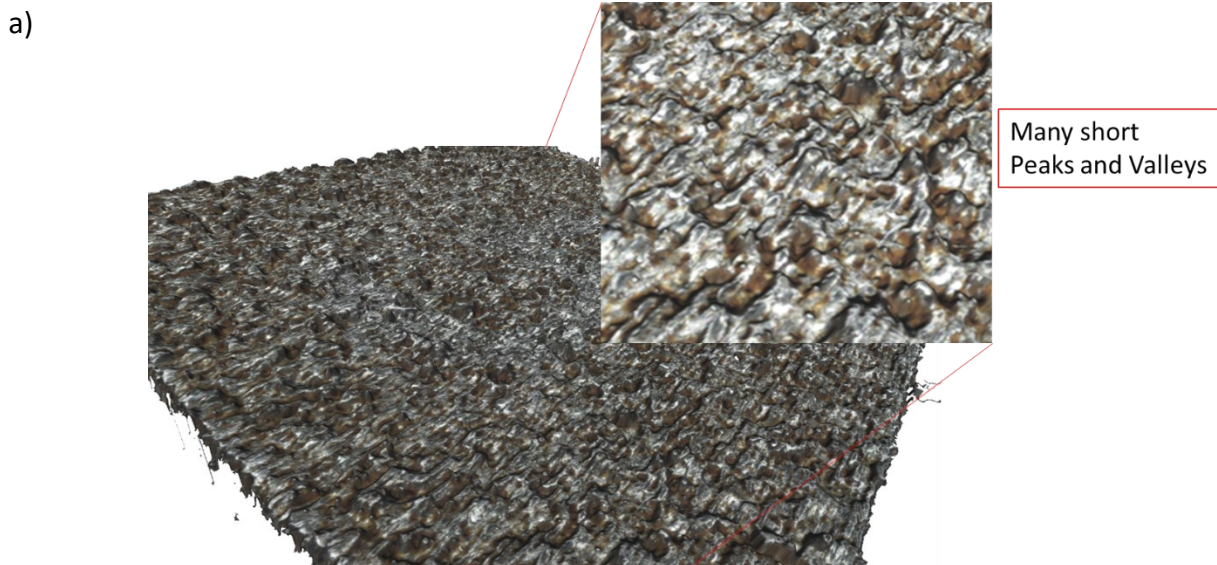
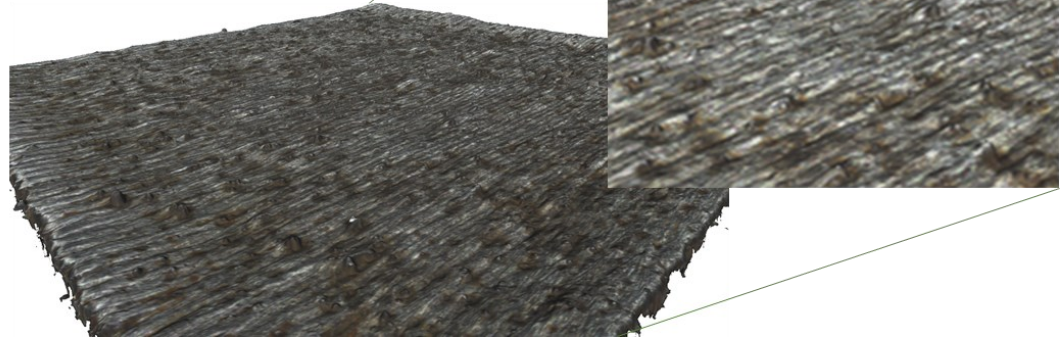


Figure 37: Process parameters of each samples correlated with the presence of specific surface defects.



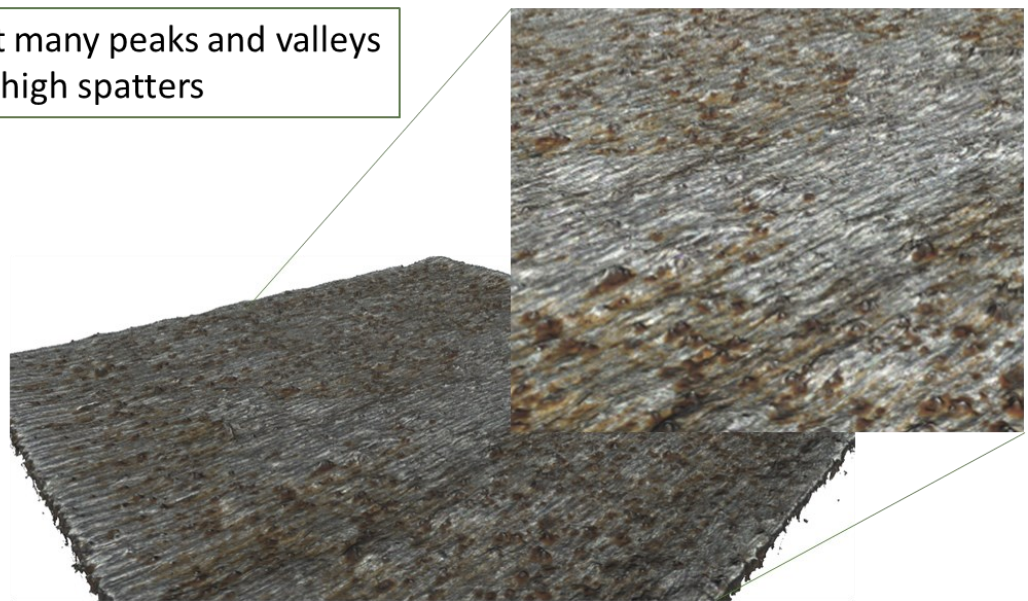
b)

-Not many peaks and valleys  
-No high spatters



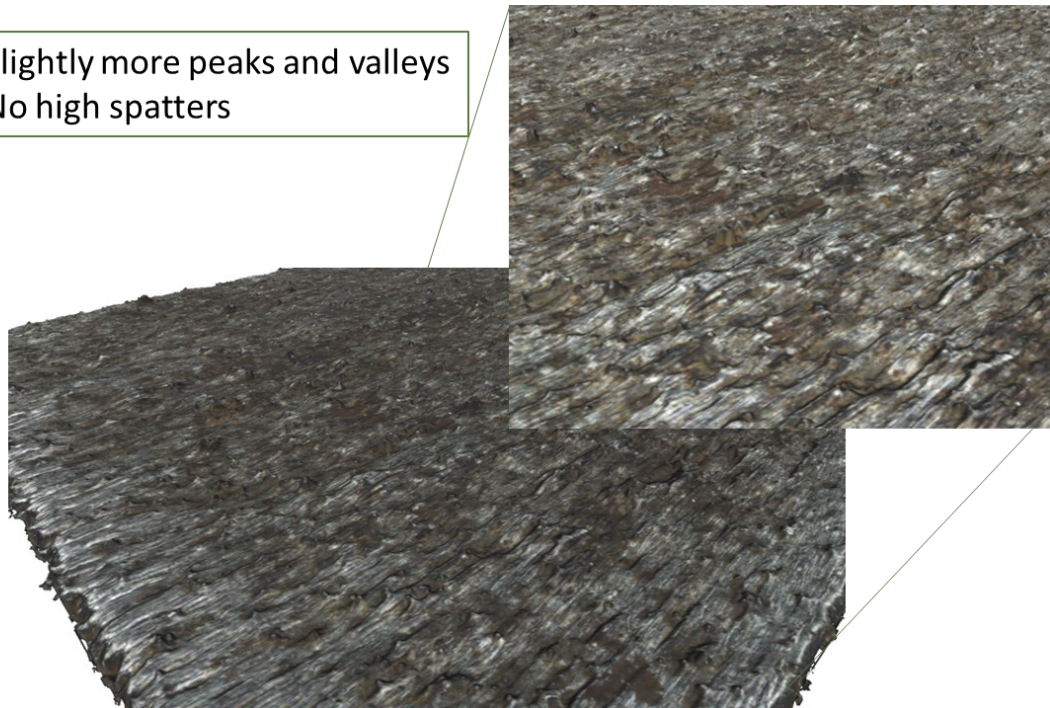
c)

-Not many peaks and valleys  
-No high spatters



d)

-Slightly more peaks and valleys  
-No high spatters



e)

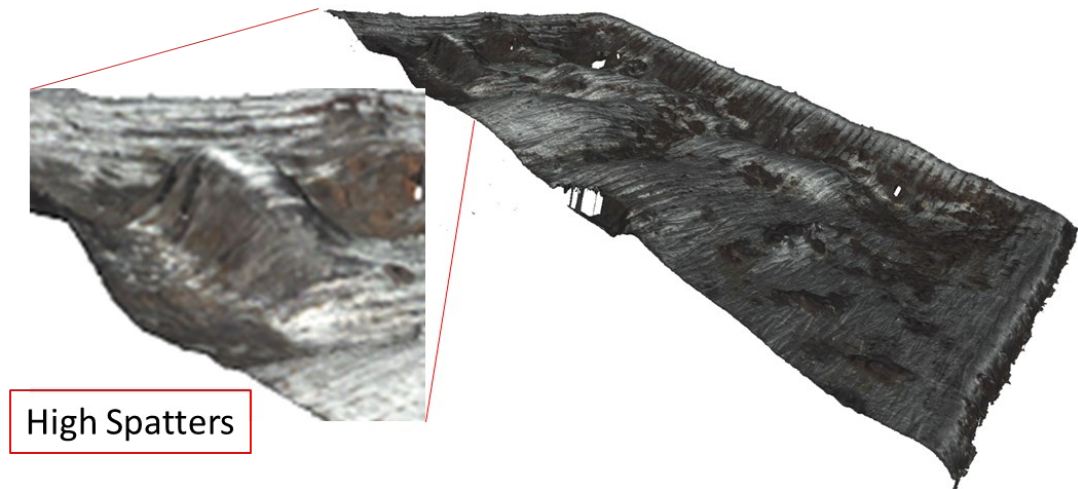


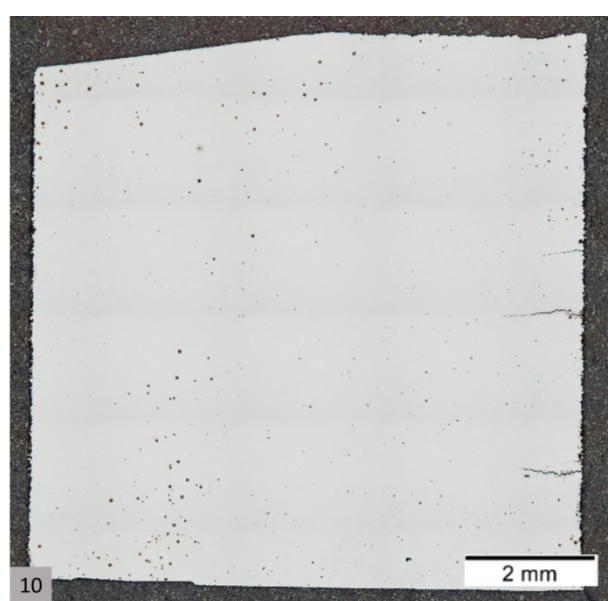
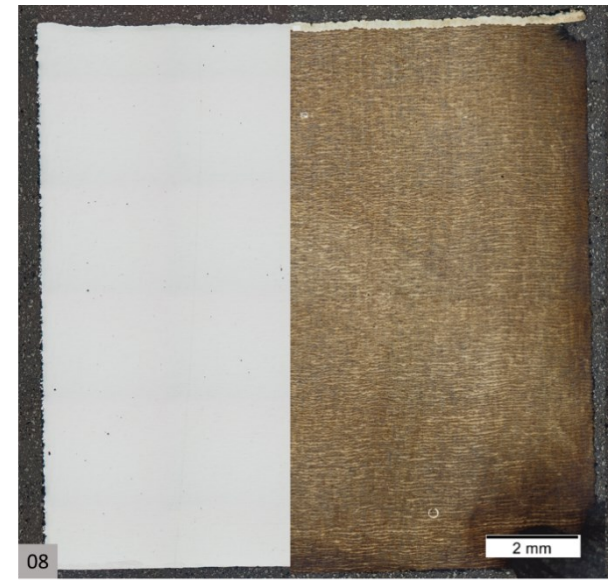
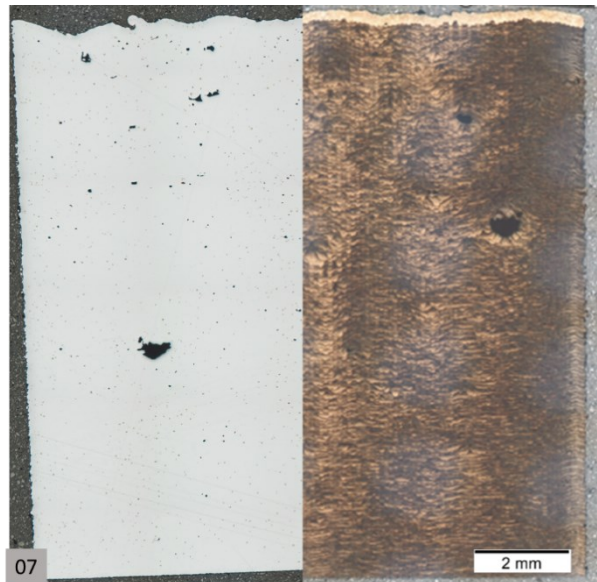
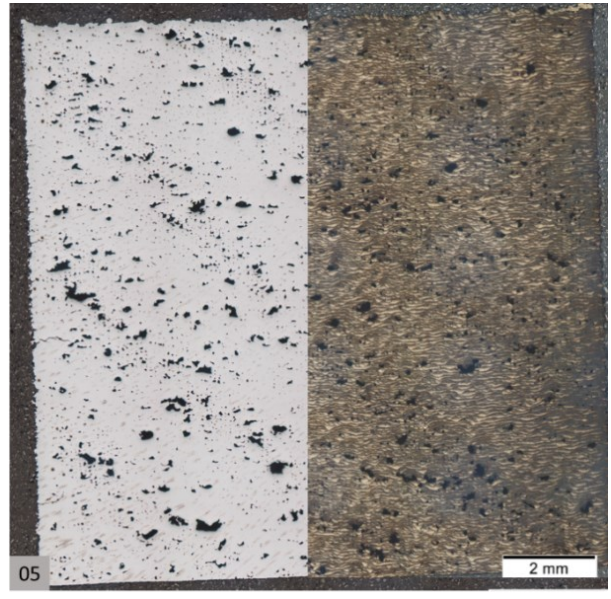
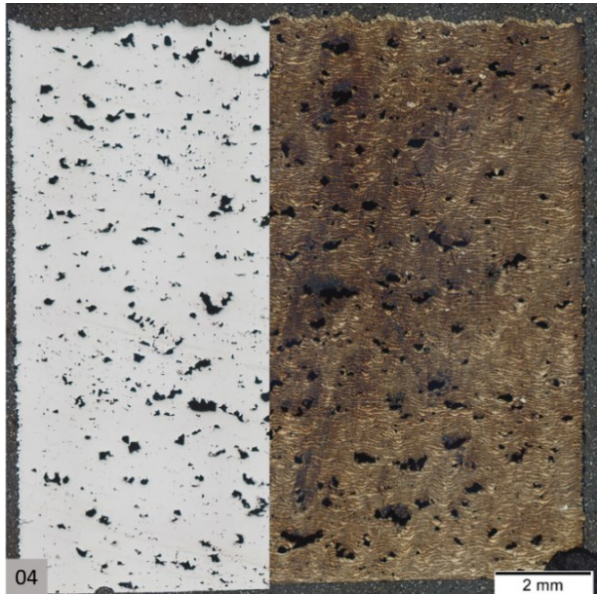
Figure 38: Surface roughness of the samples at increasing volumetric energy density from a) low  $E_d$  (Sample 05: 34,72 J/mm<sup>3</sup>) to b,c,d) medium  $E_d$  (Sample 08: 62,5; Sample 12: 83,33; Sample 13: 111,1 J/mm<sup>3</sup>) and e) high  $E_d$  (Sample 16: 208,33 J/mm<sup>3</sup>).

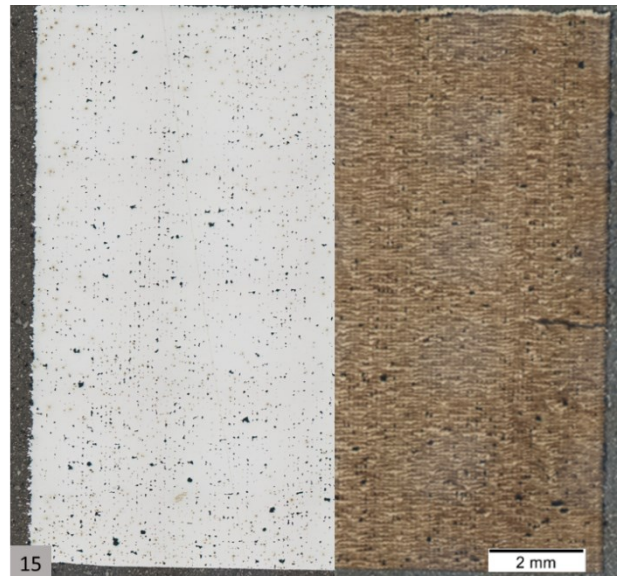
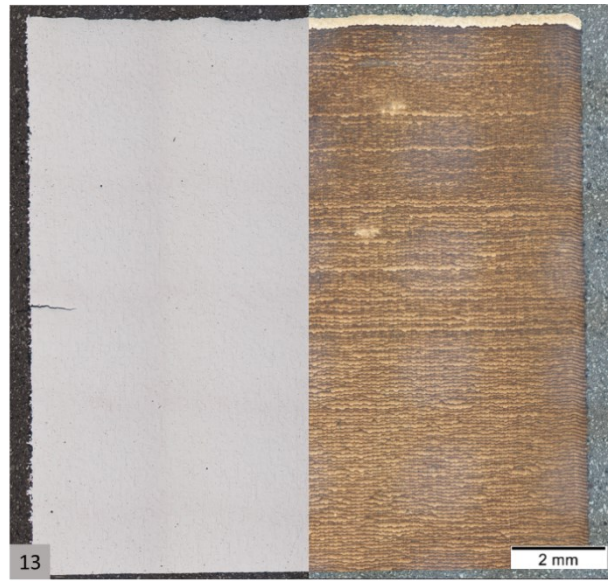
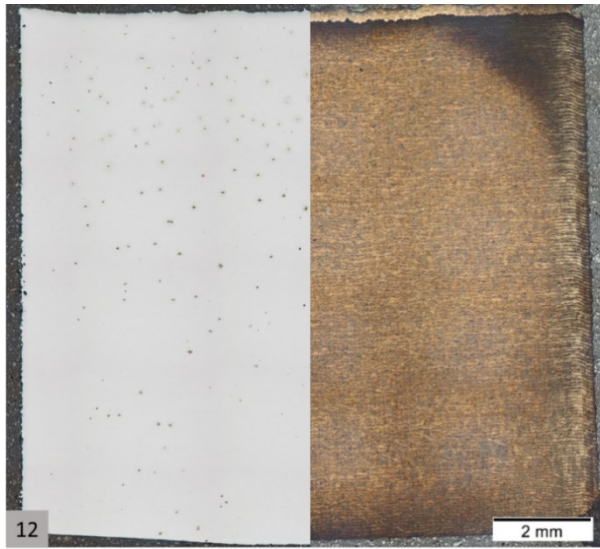
### 4.3 Cross-section overviews

Figure 39 shows the overviews of the cross-section (1 cm x 1 cm) of each samples, before (left) and after (right) etching with Nital.

These micrographs were used to observe the defects present within the pieces and to check the closed porosity that were not considered by the pycnometer analysis. The porosities percentage was evaluated by Stream Analysis Software.

Moreover, the cross-section overviews after etching were used to observe the top layers of the pieces (light etched area at the top of each cross section). Further explanations are given in the next chapters.





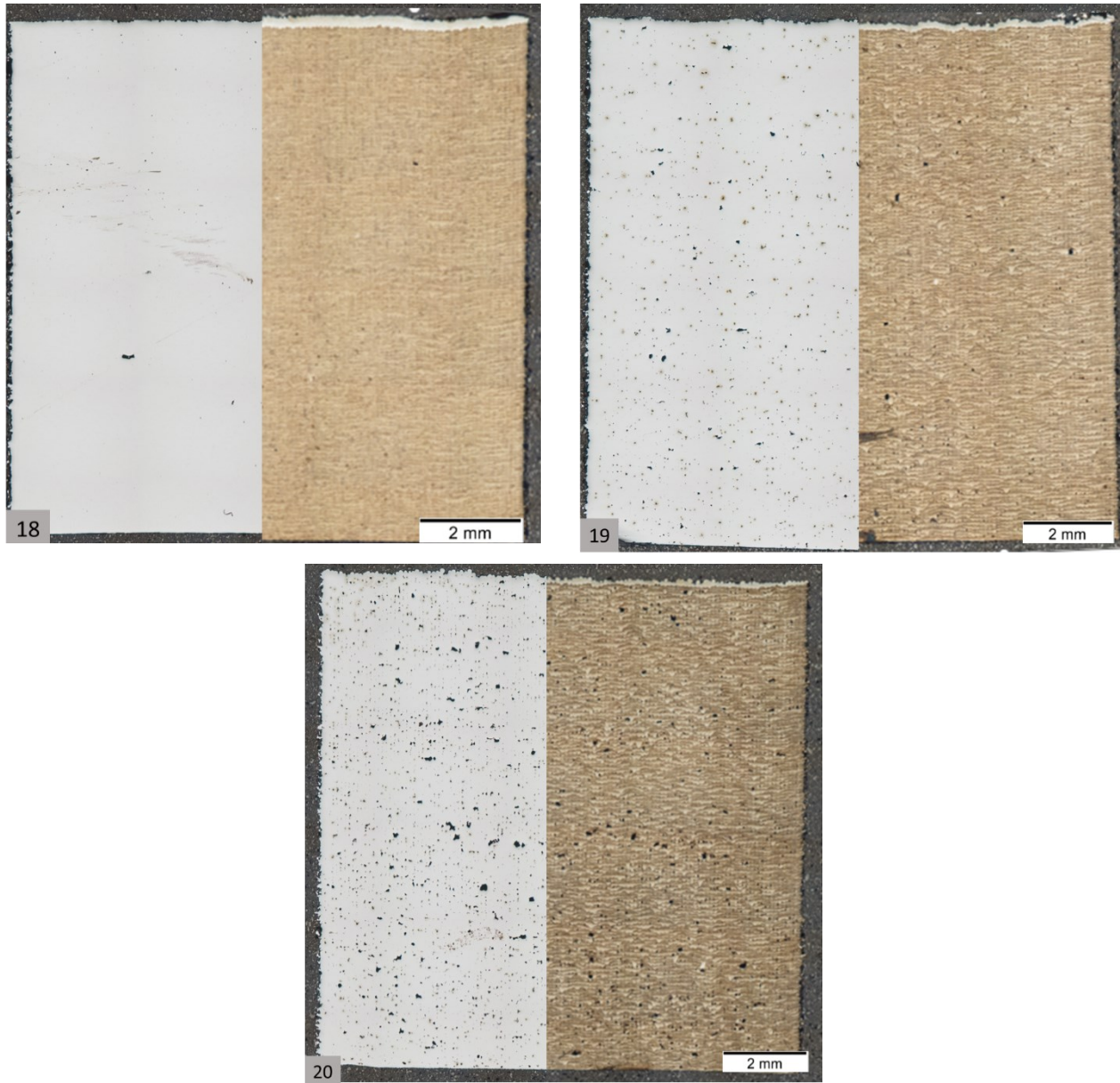


Figure 39: Overviews of all the cross-sections of the fully printed samples, taken with a 2,5x magnification.

#### 4.3.1 Internal Defects Analysis

Figure 40 shows the most common type of porosity which was found in all the cross-sections (Figure 39): gas porosities. This kind of porosity consisted of very little spherical gas bubbles trapped inside the microstructure.

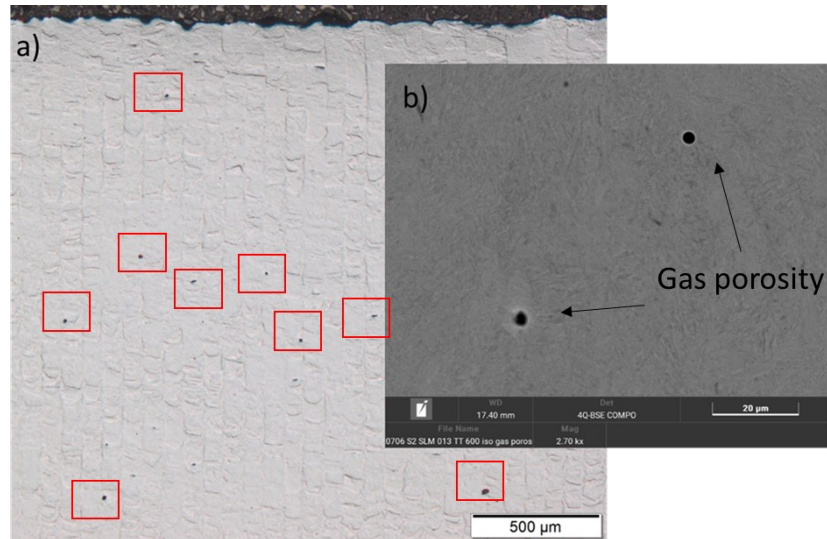


Figure 40: Gas porosity illustrations a) OM micrograph (pores are highlighted in the red boxes) b) SEM micrograph.

Another type of porosity which was detected during the microscope examinations is the Lack of Fusion (LOF) porosity, shown in Figure 41. This kind of defect was established to have no specific shape and some virgin powders has been observed inside of it (Figure 41c).

Differently from gas pores, LOF porosity was not detected in all the specimens, but only in the samples with high (above  $150 \text{ J/mm}^3$ ) or low (below  $70 \text{ J/mm}^3$ ) volumetric energy density together with extreme combinations of laser power and laser scanner speed. Indeed, the samples which were affected by this kind of porosity were localized in the outermost points of the graph (Figure 43): high laser power-high laser scanner speed, low laser power-low laser scanner speed and high laser power- low laser scanner speed.



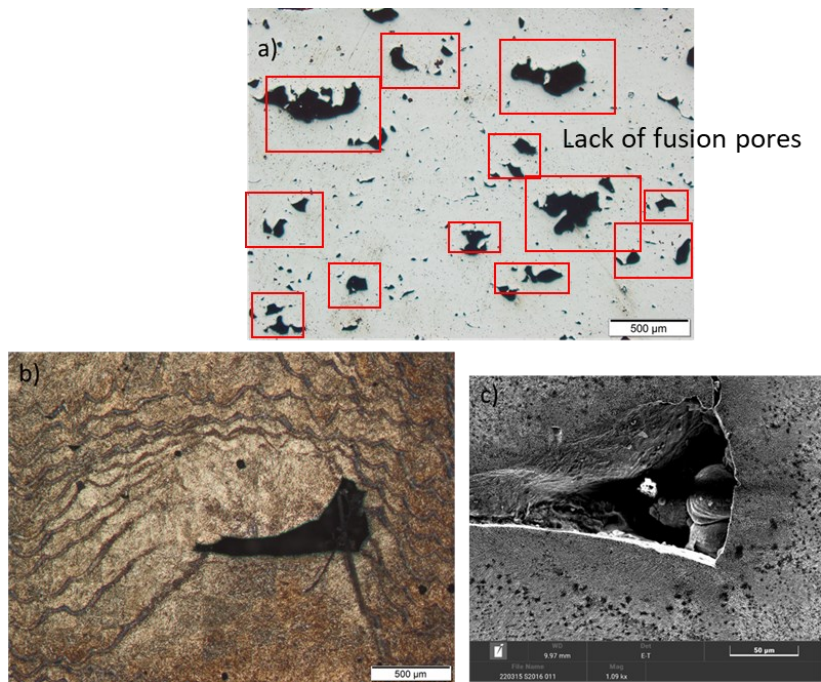


Figure 41: Lack of Fusion pores illustrations: a) OM micrograph of a porous area filled with lack of fusion holes b) OM micrograph after etching of a big-sized lack of fusion pore c) SEM micrograph of b) showing unmelted powder particles inside the pore.

Only in a few specimens was also possible to find Key-hole defects, as displayed in Figure 42. This kind of porosity showed a specific “vase” shape. Their presence could not be correlated to specific parameters ranges.

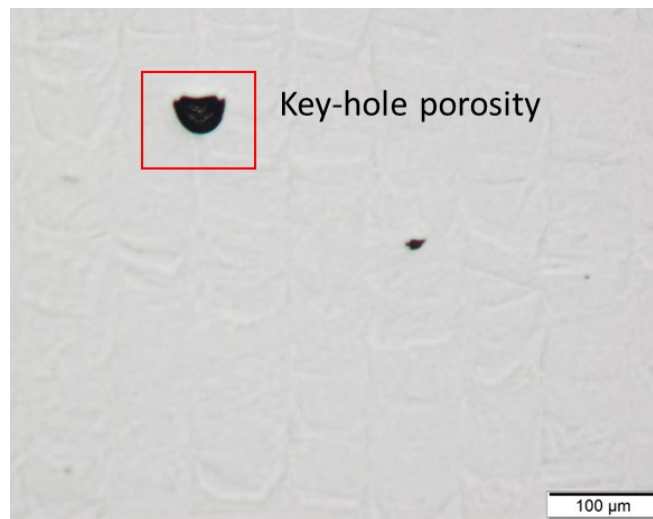


Figure 42: OM micrograph showing a key-hole defect.

In Figure 43, the effect of different sets of parameters on the presence of porosities of different kinds is displayed.


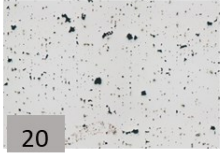
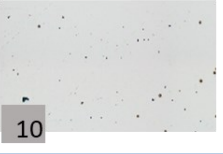
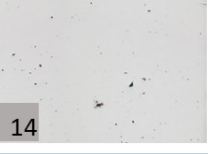

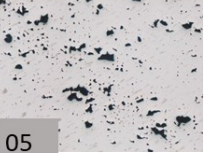
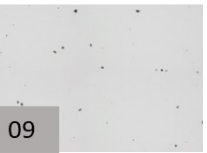
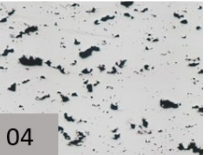
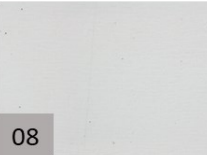
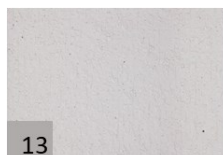
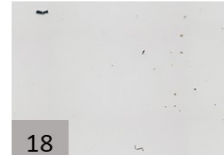


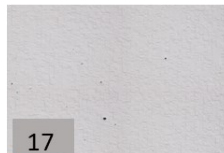
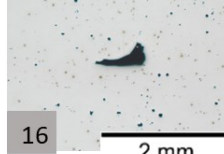
Laser Scan Speed [mm/s]	2000	Not processed	Not processed	 15	 20
	1500	Not processed	 10	 14	 19
	1250	 05	 09	Not processed	Not processed
	1000	 04	 08	 13	 18
	750	Unprocessable	 07	 12	 17
	500	Unprocessable	Unprocessable	Unprocessable	 16 2 mm
	0	100	150	200	250
	Laser Power [W]				

Figure 43: Combination of the two variable process parameters used to create the fully printed samples in relation to zoomed parts of the overviews to highlight the presence of porosities.

In many samples, cracks on the sides of the cross-sections were identified, as it is shown in Figure 44. As well as for the key-hole defect, it was not possible to correlate their presence to a combination of process parameters.

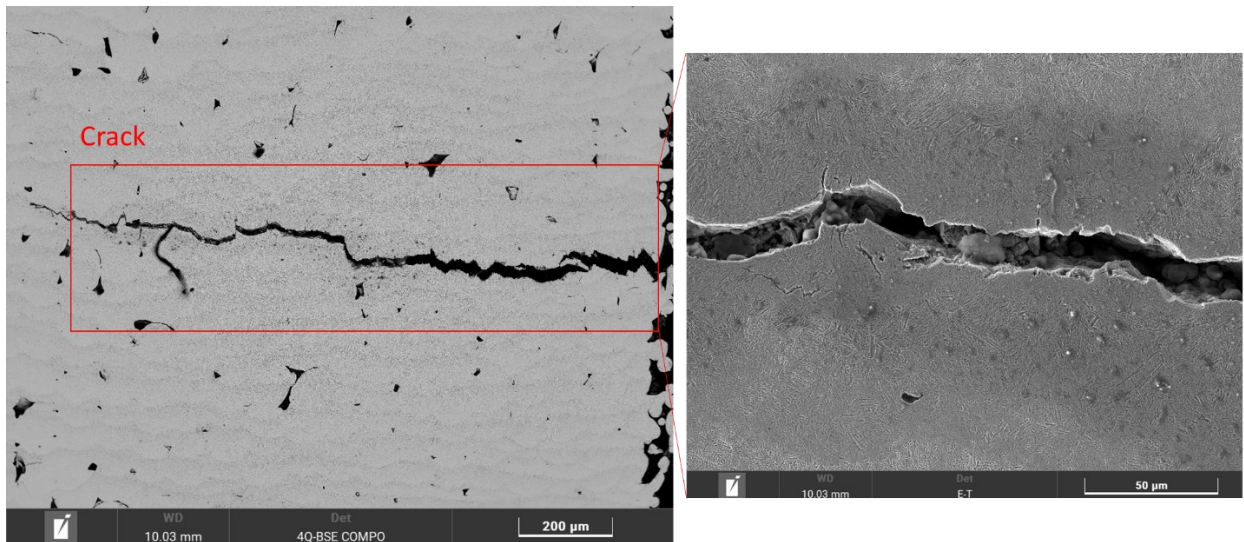


Figure 44: Side crack SEM micrographs. On the right a zoom-in of the centre of the same crack showing powder particles underneath.

Lastly, on the top part of some of the cross-sections, it was possible to see big spatters (Figure 45). Their presence was correlated to the presence of trapped porosities below them and to a very high volumetric energy density of the laser beam.

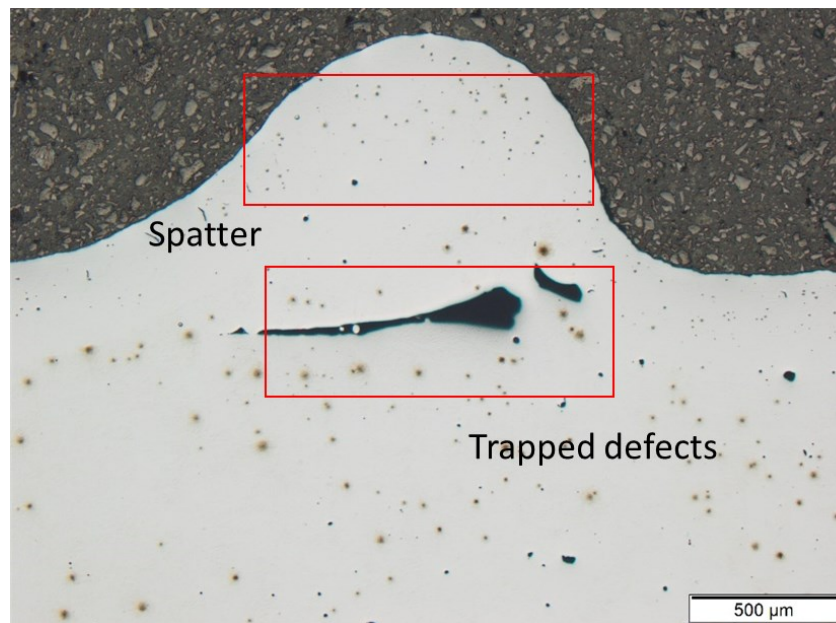


Figure 45: OM micrograph of a surface spatter.

In order to deeper analyse the porosity inside the cross-sections of the samples, a quantification was held using Stream Analysis Software. Thanks to the overview before-etching, it was possible to identify the porosities and to quantify them. In Table 8 are shown the percentage values of porosities of each as-fabricated piece which were computed by the software. These values were only an indication of the level of porosities inside the whole piece, considering

that they had been only calculated in one single cross-section, not in the entire volume. However, they were really useful once compared to the density values (Table 7) from which it was possible to find a remarkable correlation, proving the quality of the density measurements.

Sample	% of porosity	% of density
04	6,220	96,577
05	4,893	97,040
07	0,422	99,347
08	0,040	99,598
09	0,031	99,506
10	0,071	99,450
12	0,033	99,648
13	0,039	99,454
14	0,221	99,283
15	1,423	98,562
16	0,377	99,483
17	0,062	99,722
18	0,039	99,884
19	0,708	99,216
20	2,205	98,079

*Table 8: Values of percentage of porosities and density of each fully printed as-built sample.*

Moreover, the software quantification of porosities was useful to obtain a distribution of the pores on the Y-axis and on the pore sizes. This analysis was made for all the cross-sections but only three representative ones will be shown. They stand for three stages of volumetric energy density: sample 05 as low  $E_d$  (34,72 J/mm<sup>3</sup>), sample 13 as medium  $E_d$  (83,33 J/mm<sup>3</sup>) and sample 16 as high  $E_d$  (208,33 J/mm<sup>3</sup>).

In the case of the distribution along the Y-axis, shown in Figure 46, the pores are considered all equal in terms of size and they are all represented by simple dots. From the outcomes it is clear that there is no such correlation between  $E_d$  and the porosity distribution.

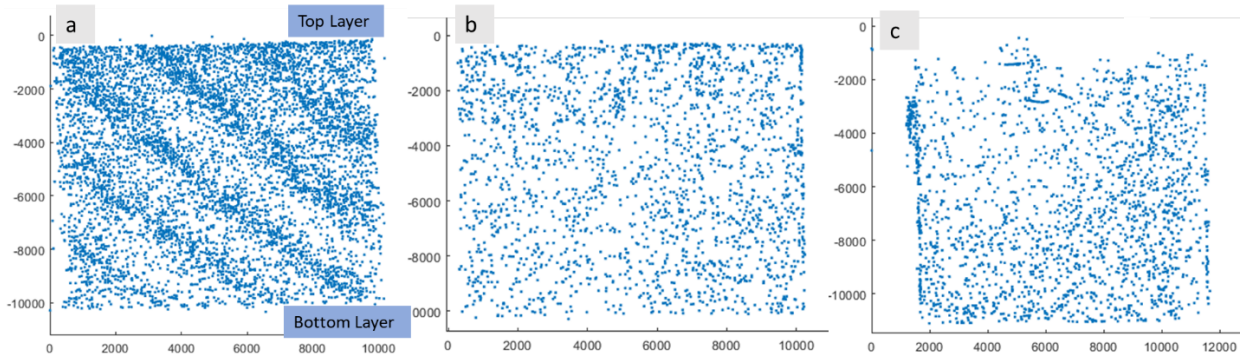


Figure 46: Graphic illustrations of the distribution of the pores along the Y-axis of their cross-sections for three different situations of volumetric energy density: a) low ( $34,72 \text{ J/mm}^3$ ) b) medium ( $83,33 \text{ J/mm}^3$ ) and c) high ( $208,33 \text{ J/mm}^3$ ).

In the case of the different pore size, shown in Figure 47, the equivalent diameter (which is defined as the diameter of a circle with an equal aggregate sectional area) of the pores, computed by the software, was used. In axis X and Y the cross-section is displayed, while on the axis Z the different sizes of the pores are visible. From the images it was clear that too-low and too-high  $E_d$  provoke higher values of such diameters. Nevertheless, in all the situations most of the pores are settled in the small-sized pores area (below  $40 \mu\text{m}$ ).

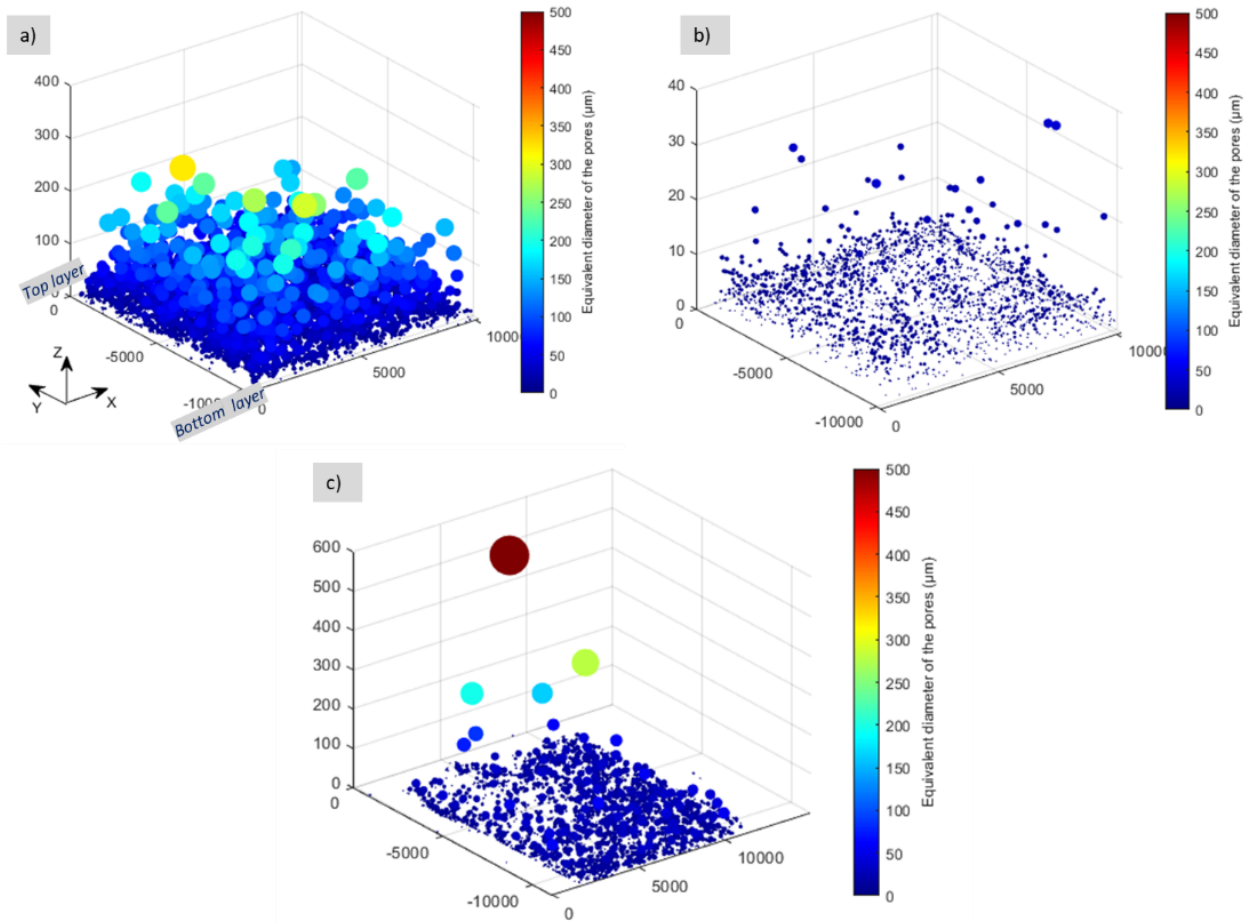


Figure 47: Graphic illustrations of the distribution of the pore size (z-axis) along the cross-section (x and y-axis) for three different situations of volumetric energy density: a) low ( $34,72 \text{ J/mm}^3$ ) b) medium ( $83,33 \text{ J/mm}^3$ ) and c) high ( $208,33 \text{ J/mm}^3$ ).

### 4.3.2 Layer Characterization

The evaluation of the melt pool morphology has been made using the cross-sections of the as-built specimens, considering once again the three symbolic ones: sample 05 as low  $E_d$  ( $34,72 \text{ J/mm}^3$ ), sample 13 as medium  $E_d$  ( $83,33 \text{ J/mm}^3$ ) and sample 16 as high  $E_d$  ( $208,33 \text{ J/mm}^3$ ).

In general, within a single layer, bright and dark etched regions could be observed, representing the different areas of the Heat Affected Zone (HAZ). They represented the beginning and the end of each layer: the laser track boundaries resulted as thin and dark etched, whereas the centre of the melt pools was seen as large and bright etched. In addition, the overlapping of the layers was also analysed in order to correlate the various situations with the presence of defects between the layers.

As it is possible to notice in the picture, the sample with the lowest energy density (Figure 48a) had a bad overlapping the laser track lines. A similar situation was visible in the as-printed piece with high  $E_d$  (Figure 48c), while the case of medium  $E_d$  (Figure 48b) showed a situation of

regularity and good overlapping corresponding to a very well distribution of the layers.

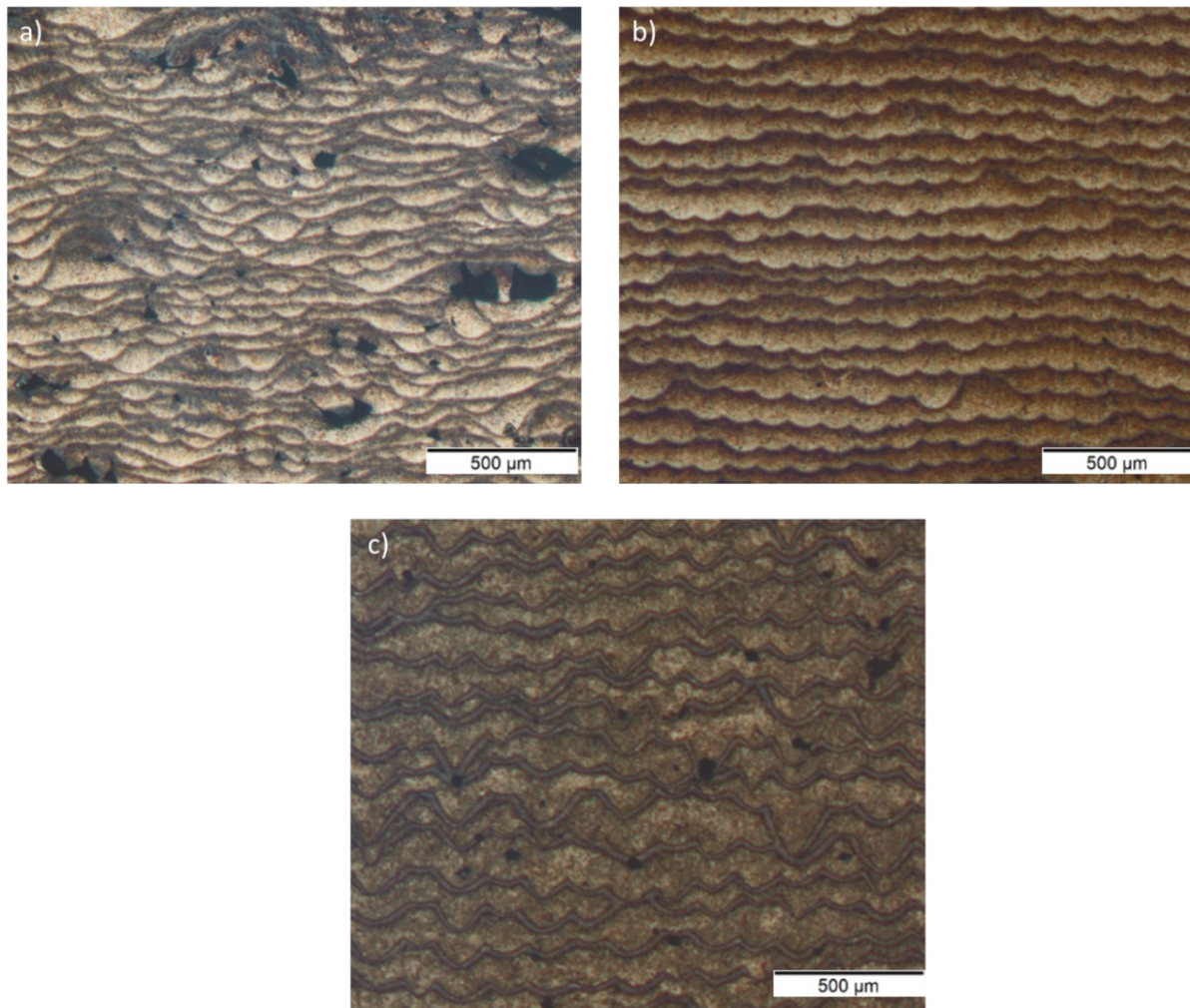


Figure 48: OM micrographs of the layer distribution for three different situations of volumetric energy density: a) low ( $34,72 \text{ J/mm}^3$ ) b) medium ( $83,33 \text{ J/mm}^3$ ) and c) high ( $208,33 \text{ J/mm}^3$ ).

Moreover, the average values of the top layer and of the "apparent" melt pool depth of each sample were obtained, as explained in Figure 49d. Indeed, the original melt pool was only visible in the top layer, as it had been the last one to be deposited, while the rounded bright etched areas between the dark etched track lines are only "apparent melt pools".

As it is possible to see from Figure 49d, a remarkable correlation between the  $E_d$  and the size of the top layer was established, demonstrating that a higher  $E_d$  results on a bigger depth. Whereas, in the case of the "apparent melt pools" depth, its average value was found to be close to  $30 \mu\text{m}$ , in accordance with the layer thickness set in the SLM Process (section 3.2.2).

Together with the depth, also the shape of the top layer was identified to be changed because of an increased value of  $E_d$  (Figure 49). Indeed, for the sample with low  $E_d$  (Figure 49a) the top layer was almost not recognisable and the original melt pools were very rounded. Whereas in the case of high  $E_d$  (Figure 49b), the top layer was much thicker and much less

rounded. The situation of the medium  $E_d$  (Figure 49c) resulted as an intermediate situation between the two.

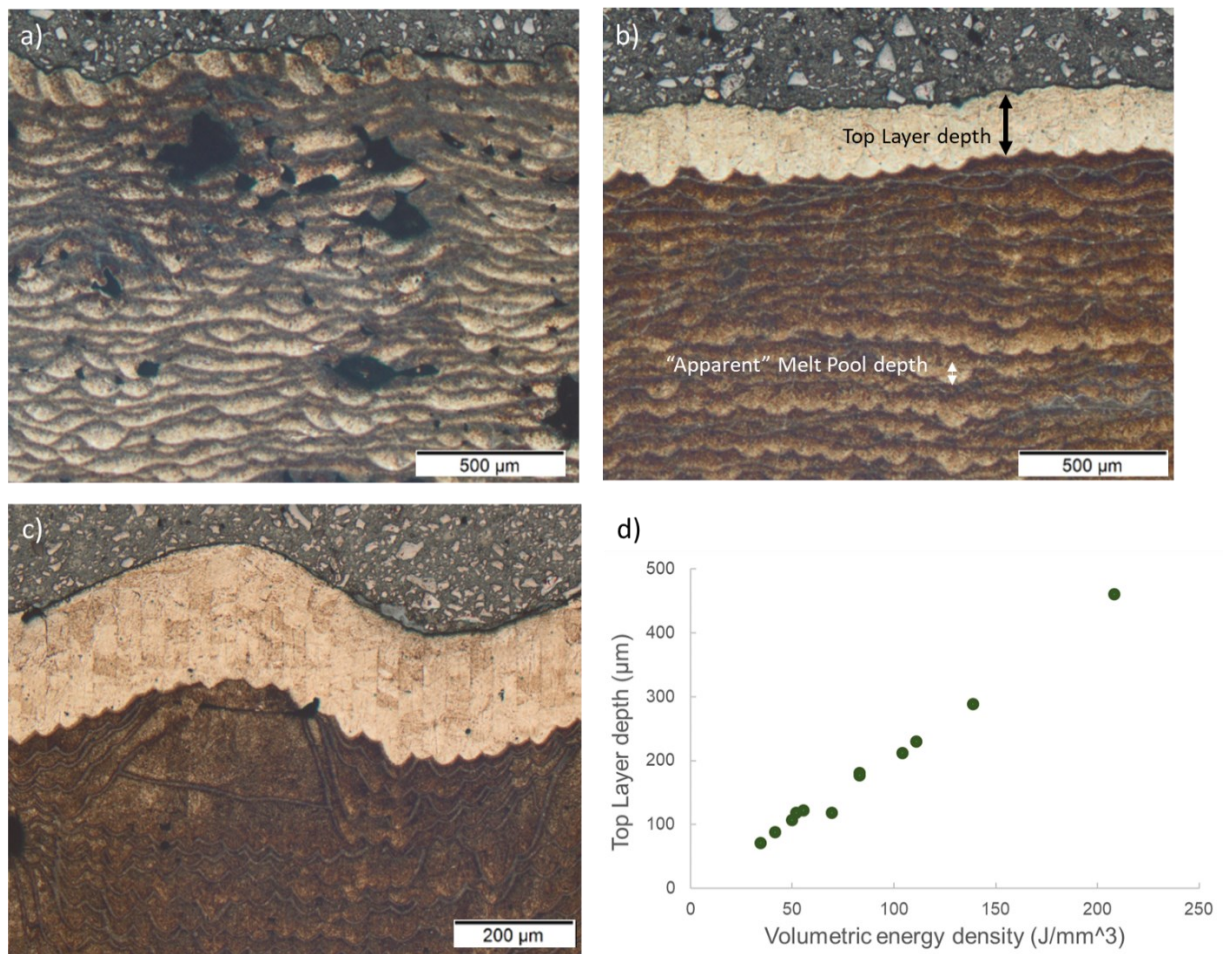


Figure 49: OM micrographs of the top layers for three different situations of volumetric energy density: a) low ( $34,72 \text{ J/mm}^3$ ) b) medium ( $83,33 \text{ J/mm}^3$ ) and c) high ( $208,33 \text{ J/mm}^3$ ); d) Graphic correlation between volumetric energy density and top layer depth of all the fully printed samples. In b) illustrations of the top layer depth and the “apparent melt pool” depth can be found as well.

### 4.3.3 Microstructure of as-built samples

To investigate deeply on the microstructure evolution, only three specimens have been ultimately considered and analysed in these terms. Indeed, as it will be explained in Chapter 5, three samples (sample 08, 12, 13) which had the best overall qualities, were selected. These pieces had slightly different values of  $E_d$  and different combinations of parameters as shown in Table 9.

Sample	Laser Power [W]	Laser Scanner Speed [mm/s]	Volumetric Energy Density [ $\text{J/mm}^3$ ]
8	150	1000	62,50

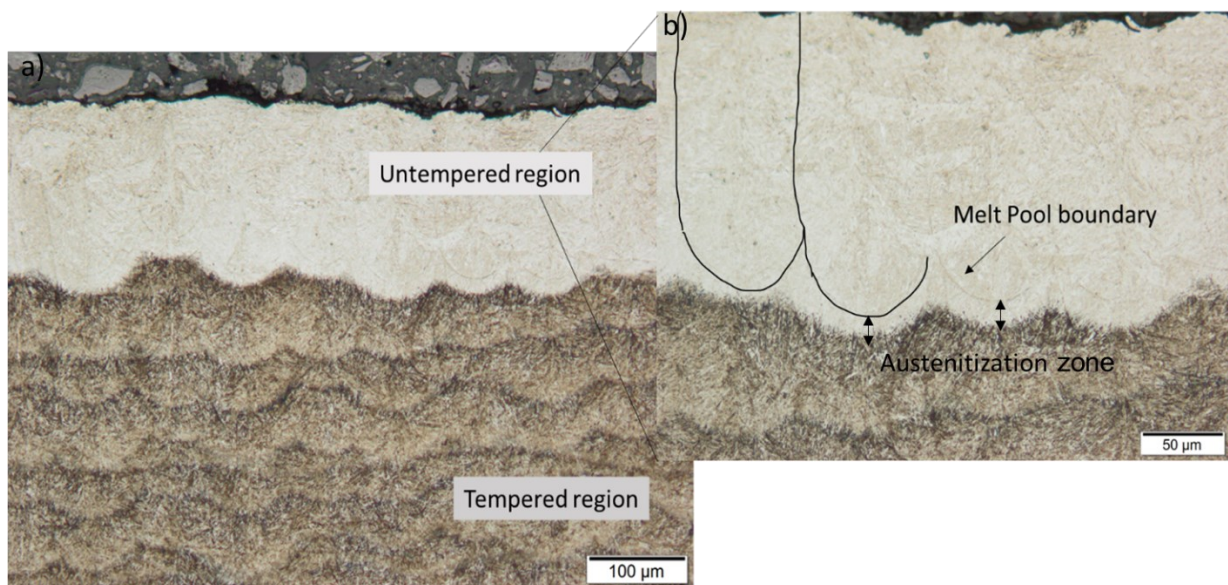


12	200	750	111,1
13	200	1000	83,33

Table 9: Process parameters of the three selected samples.

A deeper understanding of the microstructure situation is displayed in Figure 50. Indeed, taking into account the micrographs obtained after etching, it was clear that there were two different regions which will be called untempered and tempered (dark etched) martensite, as shown in Figure 50. From the micrographs it was possible to see also the original melt pools (Figure 50b). The depth of the top layer region along the Y-axis of the cross-sections was evaluated as well. The top layer depth, as previously mentioned, strongly depended on the values of  $E_d$ , but as for the selected samples its average value was in within the range of 150-250  $\mu\text{m}$ .

Furthermore, it was identified that there was a part inside the top layer that had a different microstructure as shown in Figure 50b and c. This area was called “austenitization zone”.



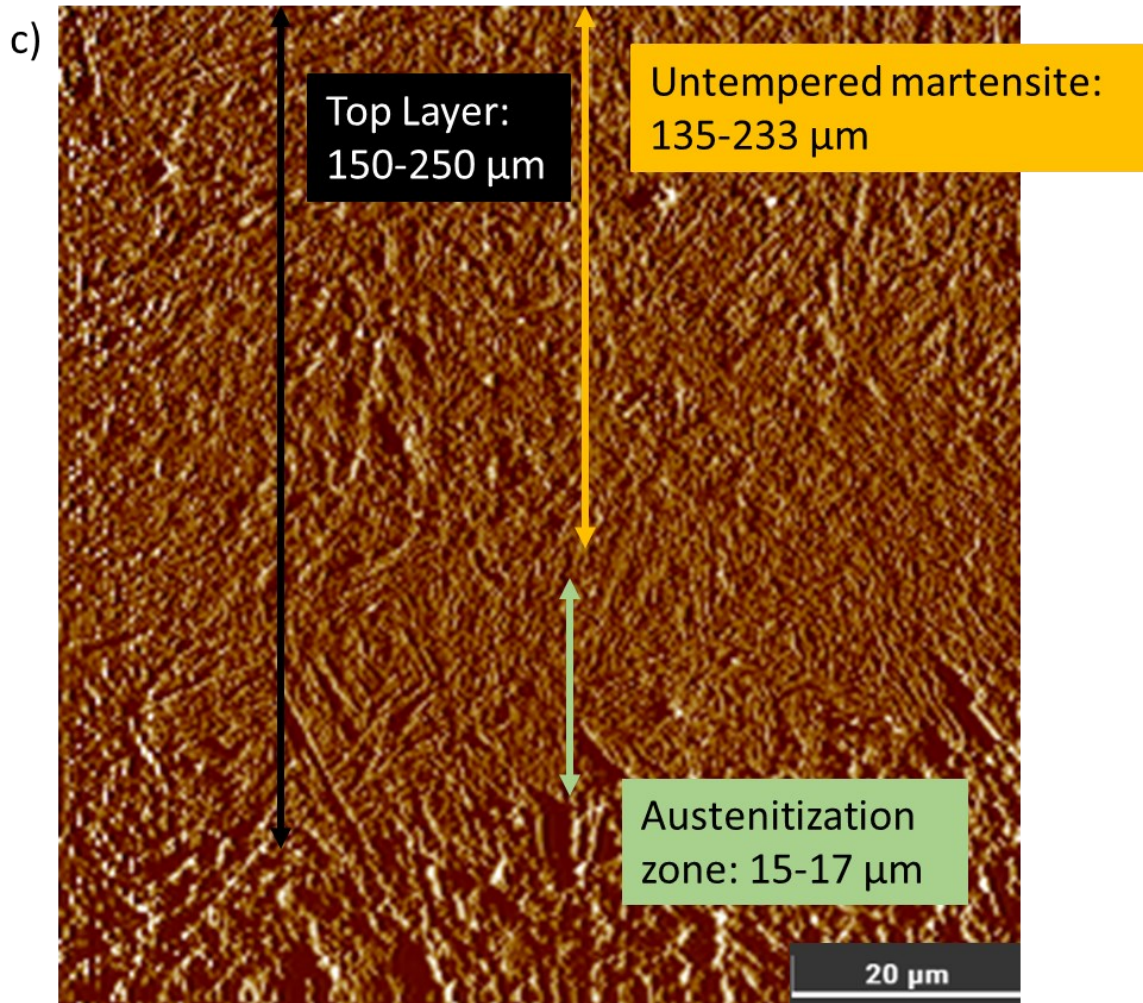


Figure 50: OM micrographs after etching: (a) showing the two regions with different macrohardness value and (b) zoomed-in image over the untampered region where the melt pool boundaries are visible; (c) image obtained using the scan mode of the nanoindenter showing the top layer region and the two different microstructures inside of it: untempered martensite and austenitization zone.

With regards to the tempered region, it was also possible to identify two different microstructures, type A and type B (Figure 51). The two different areas were easy to detect as after etching they showed a different chromaticity. The martensite type B is the dark brown etched part, while the martensite type A is light brown etched area.

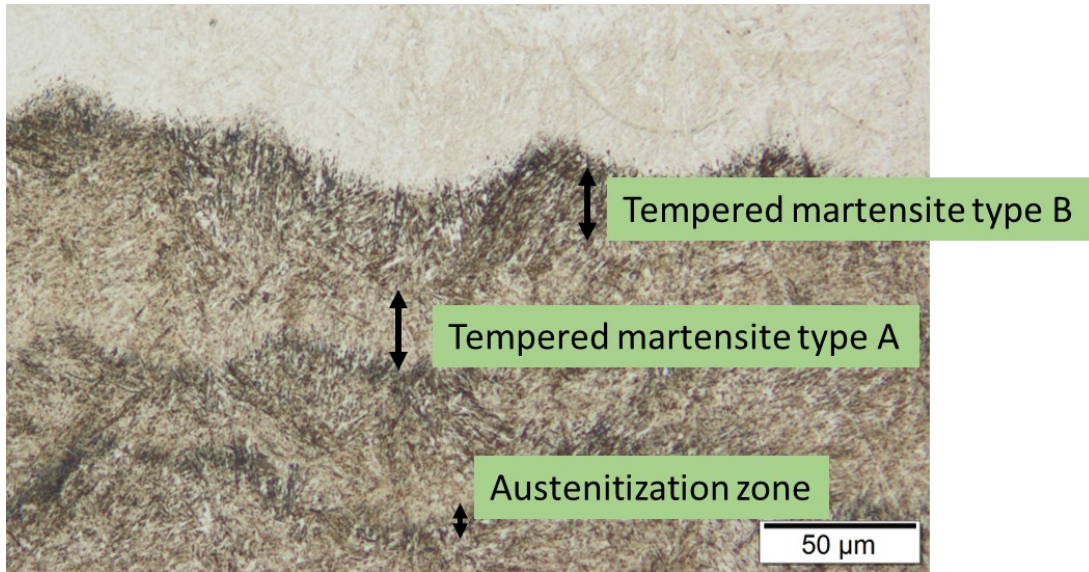
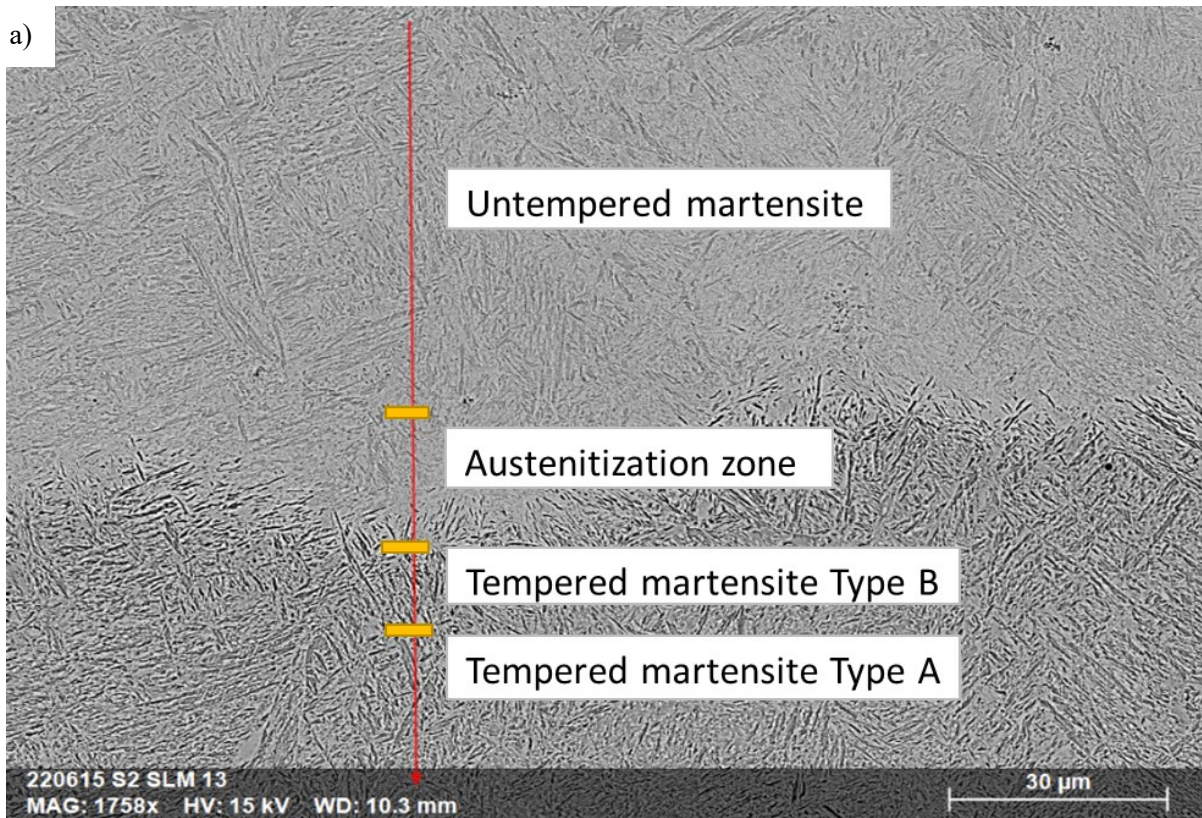


Figure 51: OM micrograph of the tempered region with a focus on the three different microstructures which were found.

The different zones detected in the as-built samples, were not only detected in the OM analysis, but in the SEM one as well, as shown in Figure 52.



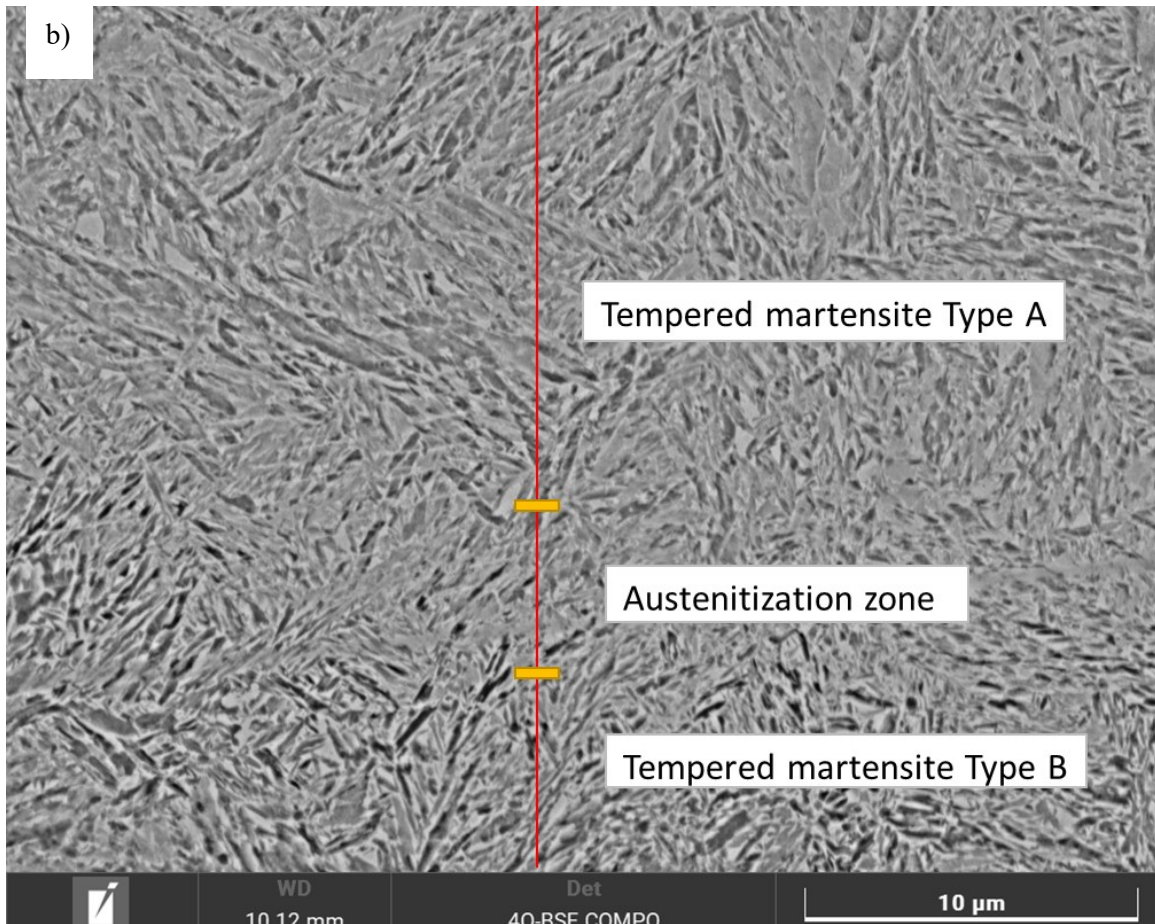
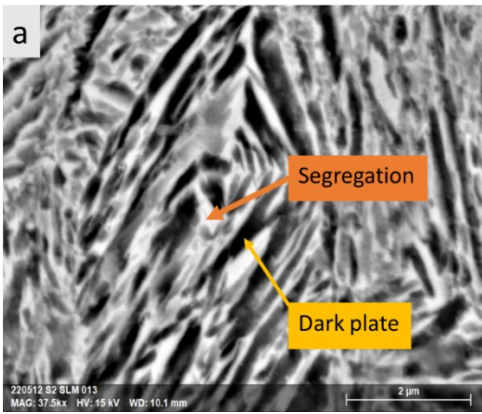
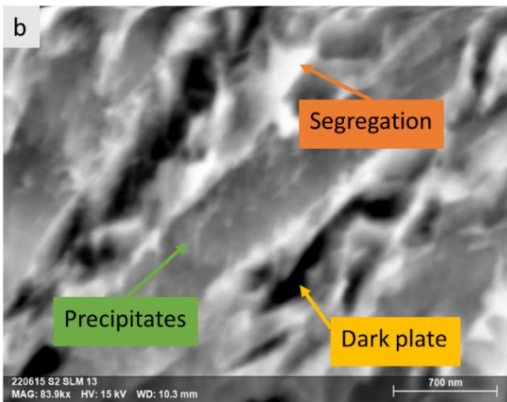


Figure 52: SEM micrographs showing the four different areas at the top layer (a) and in the middle of the cross-section (b).

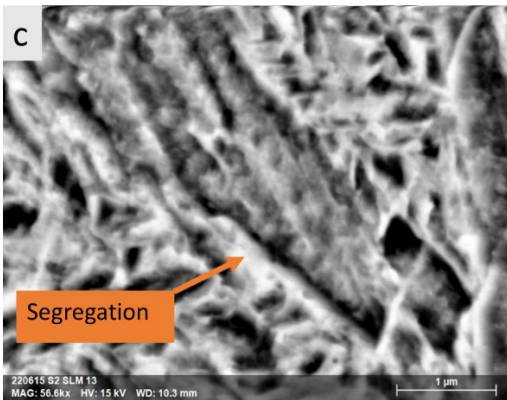
EDS analysis were performed on the different microstructures to investigate about their atomic compositions. As shown in Figure 53a, in the case of the tempered martensite type B, inside the microstructure there were various segregations and dark plates of martensite. Only in the situation of tempered martensite type A (Figure 53b), also an abundance of precipitates was detected. Indeed, as well as the tempered type B, in the untempered martensite no precipitates were found (Figure 53c). As the EDS outcomes show, both segregation and precipitates had higher content of carbon. The first ones were large bright areas, while the precipitates analysed in the type A were detected as small white spots within the martensitic lath.



% atom	Carbon	Silicon	Manganese	Iron	Molybdenum
Segregation	30,35	1,73	0,36	67,34	0,22
Dark plate	28,12	1,98	0,23	69,44	0,23
Profile	26,98	2,1	0,3	70,30	0,25



% atom	Carbon	Silicon	Manganese	Iron	Molybdenum
Segregation	27,96	1,84	0,36	69,64	0,19
Dark plate	24,52	2,01	0,38	72,91	0,13
Precipitates	26,59	1,96	0,28	70,98	0,2
Profile	25,05	2,01	0,34	72,43	0,18



% atom	Carbon	Silicon	Manganese	Iron	Molybdenum
Segregation	33,16	1,92	0,26	64,45	0,21
Profile	24,17	1,96	0,40	73,26	0,20

Figure 53: EDS atomic compositions of martensite: tempered type B (a), tempered type A (b) and untempered (c); comparison between segregation, dark plates and precipitates compositions with the one of the overall area profile.

Moreover, OM micrographs revealed a columnar growth of the central grain starting from the deepest point every melt pool track line (Figure 54). These fine columnar grains kept growing across multiple layers without changing their growth direction.

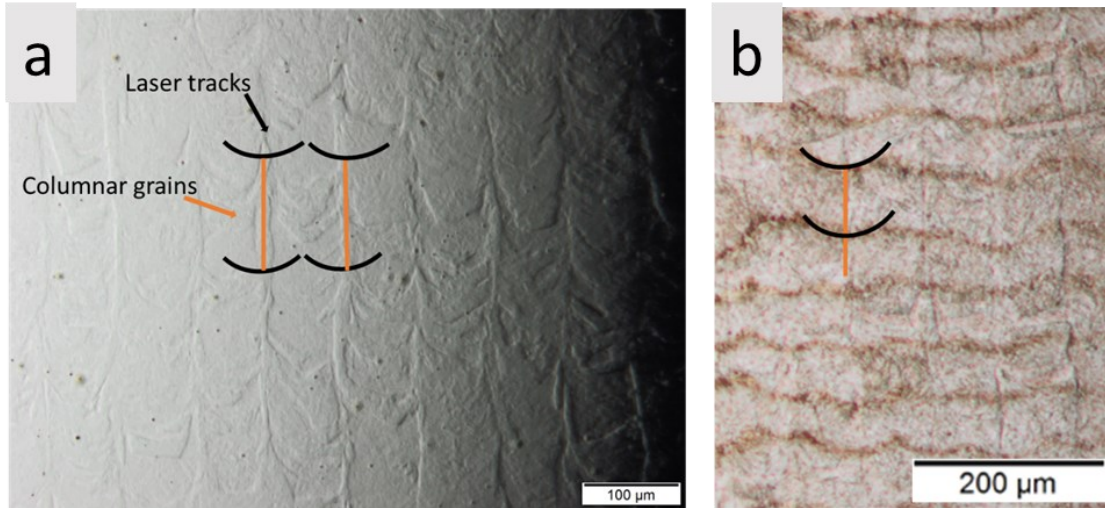
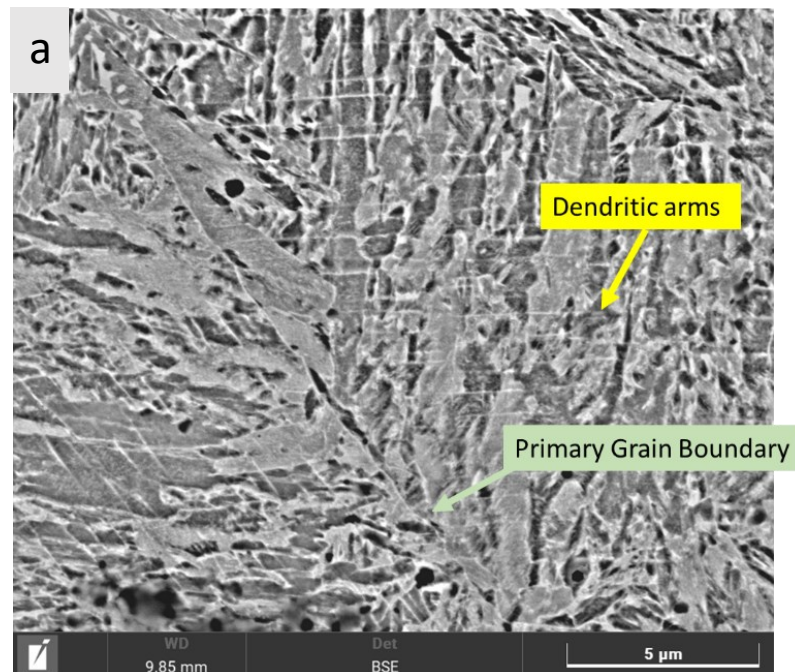


Figure 54: OM micrographs of the cross-section of one sample before (a) and after etching (b) with illustrations to highlight the visible growth of the central columnar grain.

Through the SEM investigation on the as-built samples it was seen that on the sides of the central columnar grain, several grains were growing following a different direction. Inside of these grains dendritic arms were present (Figure 55a). Indeed, a side branching phenomenon was visible, as it shown in Figure 55b, leading to epitaxial growth misaligned with the vertical grain. In addition, between two adjacent melt pools, the grains were found to be aligned at 90° each one (Figure 55c).



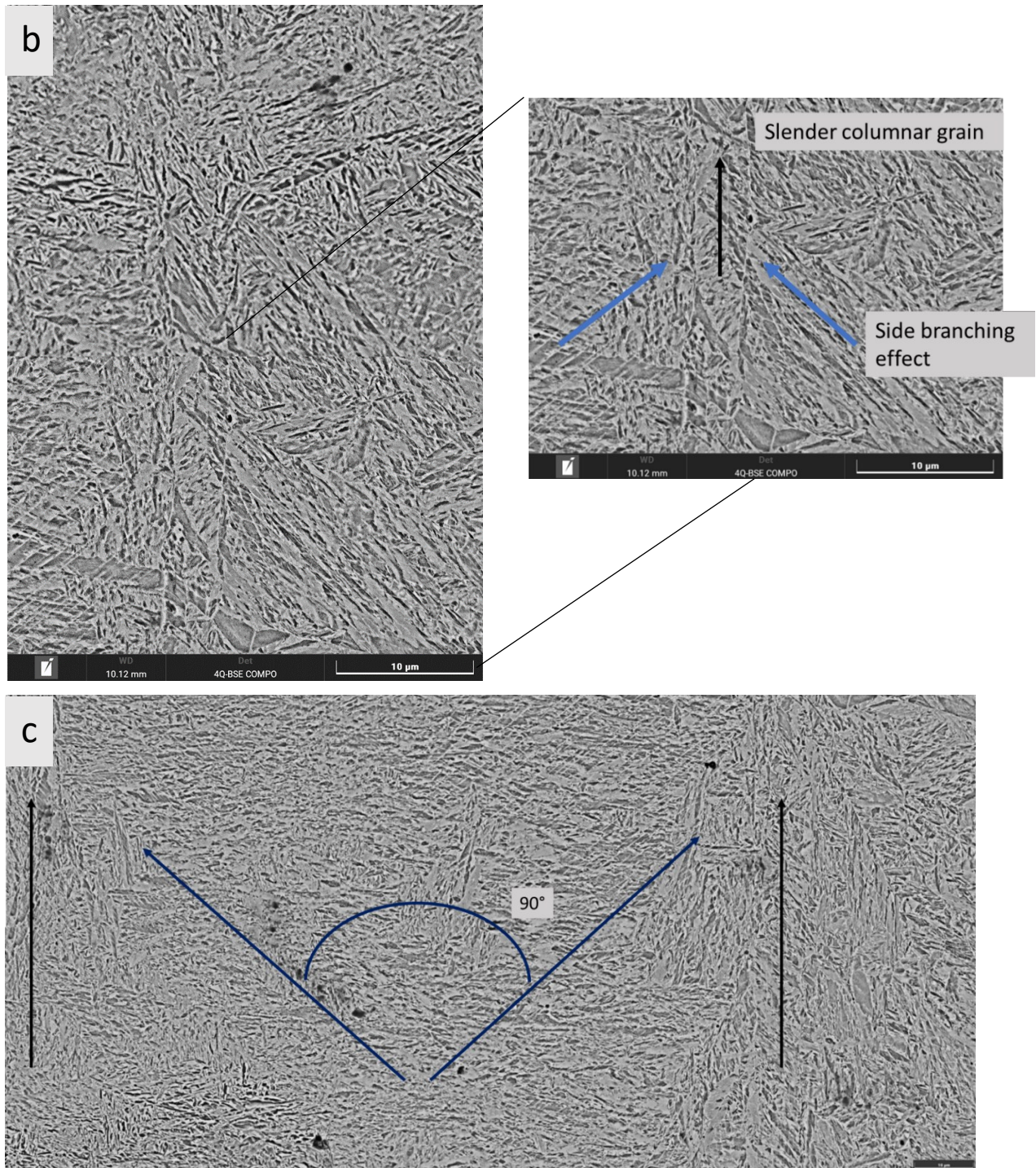


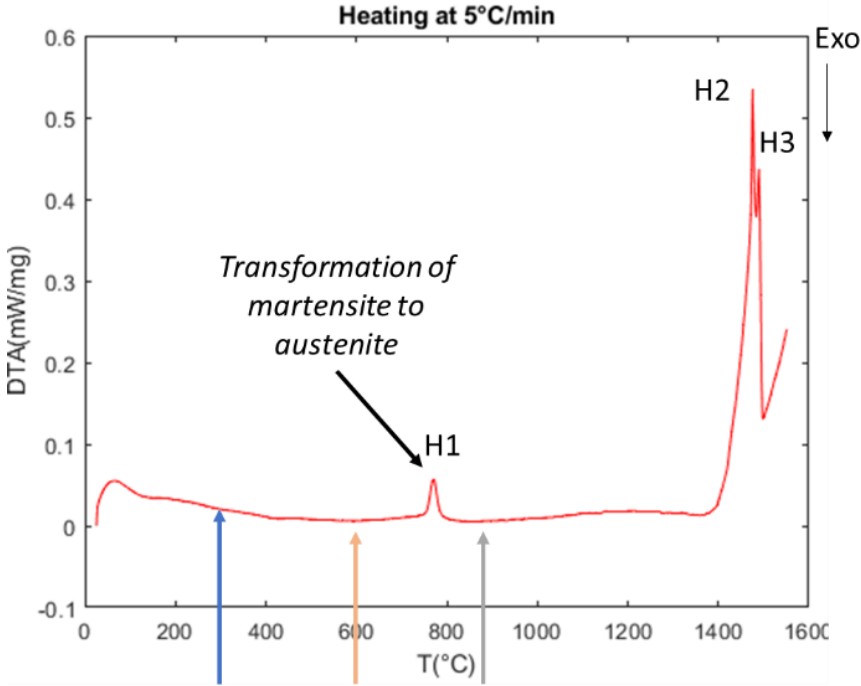
Figure 55: SEM Micrographs showing the presence of dendritic arms inside of the side grain (a) the different growth directions of the grains within one melt pool (b) and two adjacent ones (c).

#### 4.3.4 Microstructure of heat-treated samples

Sample 13 was chosen among the three best samples for DTA analysis, due to its medium value of  $E_d$  and its overall good characteristics.

A primary DTA analyse was performed up to 1550 °C to reach complete fusion. Figure 56 shows the heating curve. The endothermic peak at 760°C corresponded to the transformation

of martensite into austenite, followed by the reverse peritectic transformation (1400 – 1500 °C) where austenite is transformed into  $\delta$  ferrite and liquid. From this curve, three temperatures were selected to perform a specific heat treatment. These temperatures were 300, 600 and 900°C. For each temperature, an isothermal heat treatment of 1 hour was performed. The treatments were necessary in order to have a deeper knowledge of the microstructure of the SLM as-printed pieces.



Peak	Start Temperature [°C]	End Temperature [°C]	Reaction or phase transformation
H1	750	820	Martensite to Austenite
H2	1450	1490	Austenite to $\delta$ -Ferrite
H3	1500	1530	$\delta$ -Ferrite to liquid

Figure 56: DTA heating curve of the AISI S2 as-built, the three arrows highlight the location of the temperatures chosen for the isothermal heat treatments. Explanation of the principal heating peaks detected.

The first treatment was held until 300°C. The result was a stress-relieved microstructure, which allowed a good detection through EBSD. The bright regions in the Pattern Quality corresponded to the well indexed phases.( Figure 57a). These area was the untempered martensite type B, while the areas that were badly detected were dark etched and they corresponded to the austenitization zone (Figure 51). As the Phase Map displays (Figure 57b), the only phase used for the analyse was Iron alpha BCC, that corresponds to the bright areas of



the Pattern Quality. While looking at the Inverse Pole Figure with Z axis as orientation direction (IPFZ map, Figure 57c) it was possible to notice that within any two parallel track line, a slender vertical columnar grain was growing in the direction perpendicular to the build plate. This is the situation that was detected before as well, through the OM micrographs of the as-built samples (Figure 54).

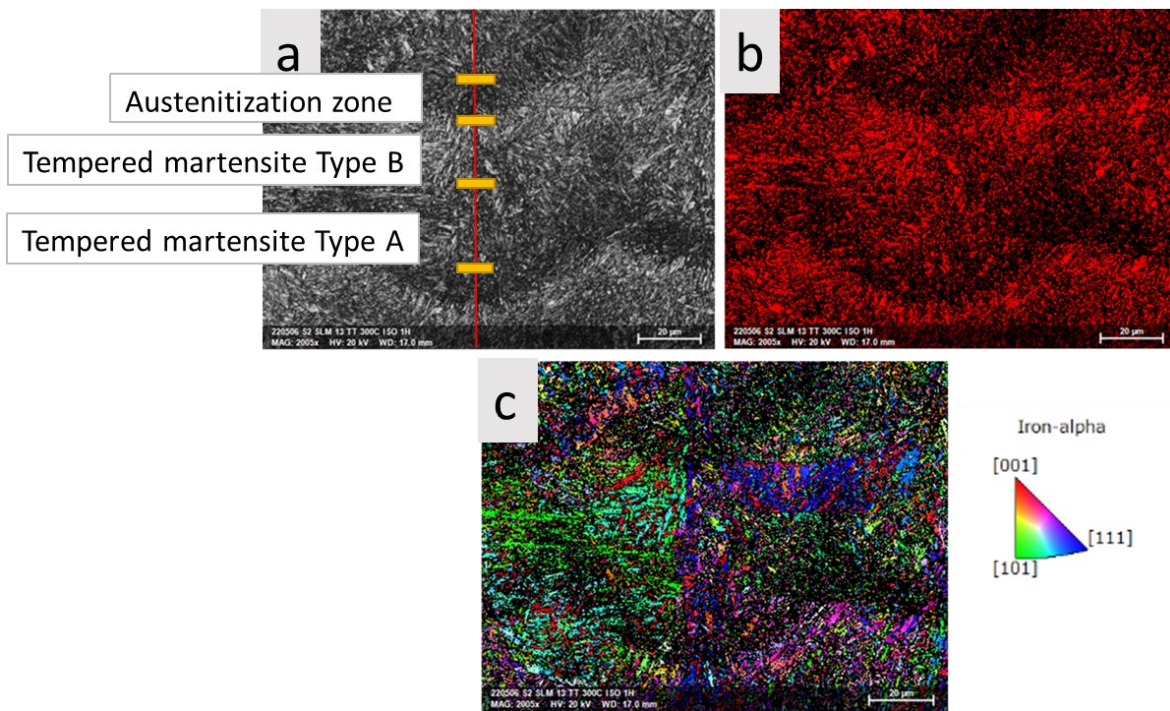


Figure 57: EBSD analysis results of the heat-treated sample until 300°C: a) Pattern Quality, b) Phase Map and c) IPFZ map with its colours legend. In the Phase Map, the red dots correspond to Iron BCC phase.

The second treatment was held until 600°C (Figure 56). As an outcome, the microstructure showed a higher quantity of precipitates and segregations (Figure 58c), which were also larger (0,3-0,4 µm) if compared to the situation in the as-built samples (0,1-0,2 µm) (Figure 53). The precipitates were still presented as white spots within the laths, whereas the carbon segregation were found to be more in the form of with lines separating the martensitic laths.

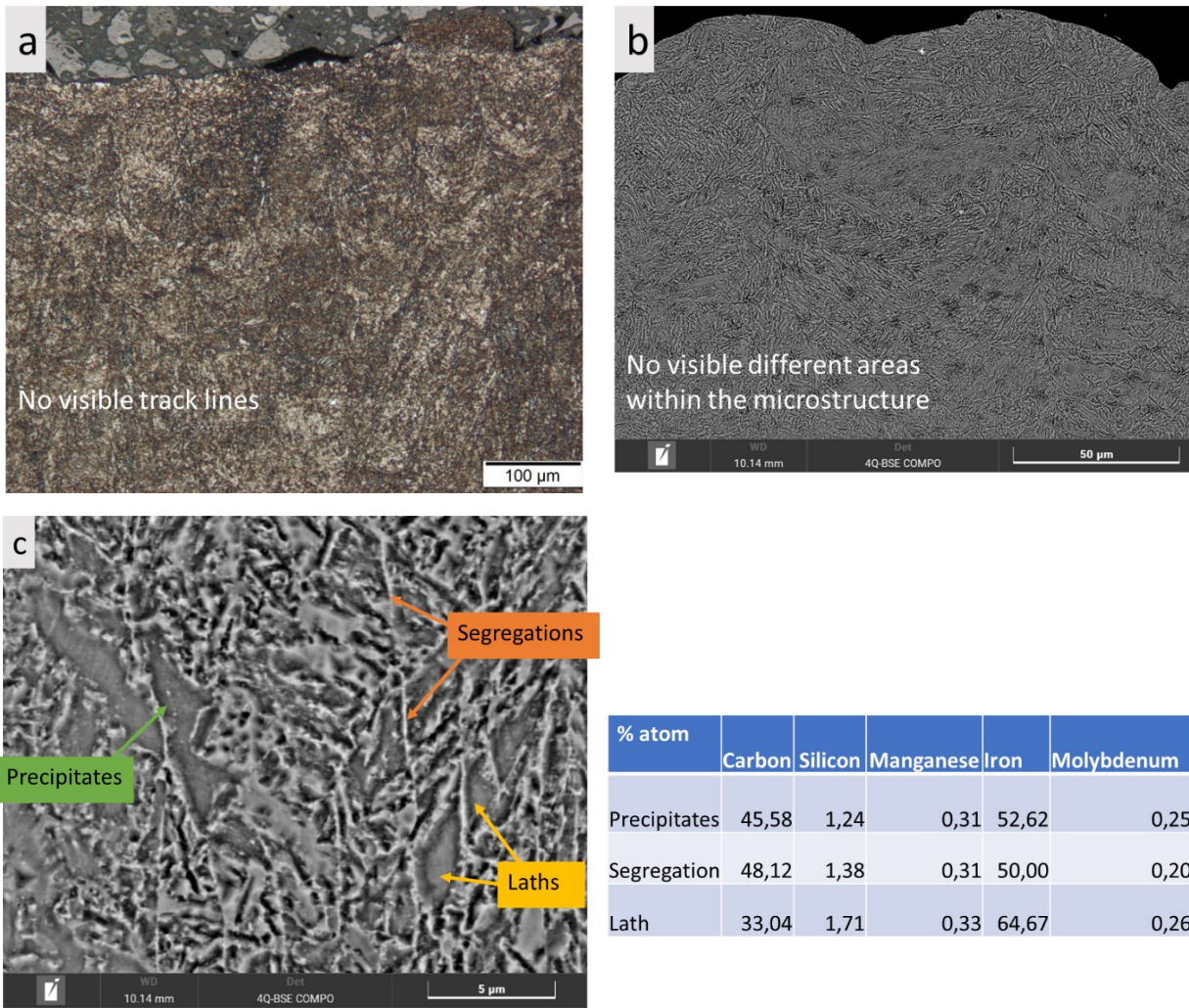


Figure 58: OM (a) and SEM (b) micrographs of the top part of the cross-section after treatment up to 600°C; c) EDS atomic compositions of different elements detected in the microstructure.

The treatment allowed to obtain a better indexed EBSD than the one of 300° (Figure 57). Indeed, in the Pattern Quality (Figure 59a) the bright areas corresponded to the whole untempered martensite, therefore this area was larger after treatment up to 600°C. Whereas, the areas that were badly detected once again correspond to the austenitization zone (Figure 51). The bright areas of the Pattern Quality corresponded to Iron BCC (Figure 59b) Whereas one big difference was the fact that it was not possible anymore to see the slender vertical columnar grain growth by looking at the IPFZ map (Figure 59c).

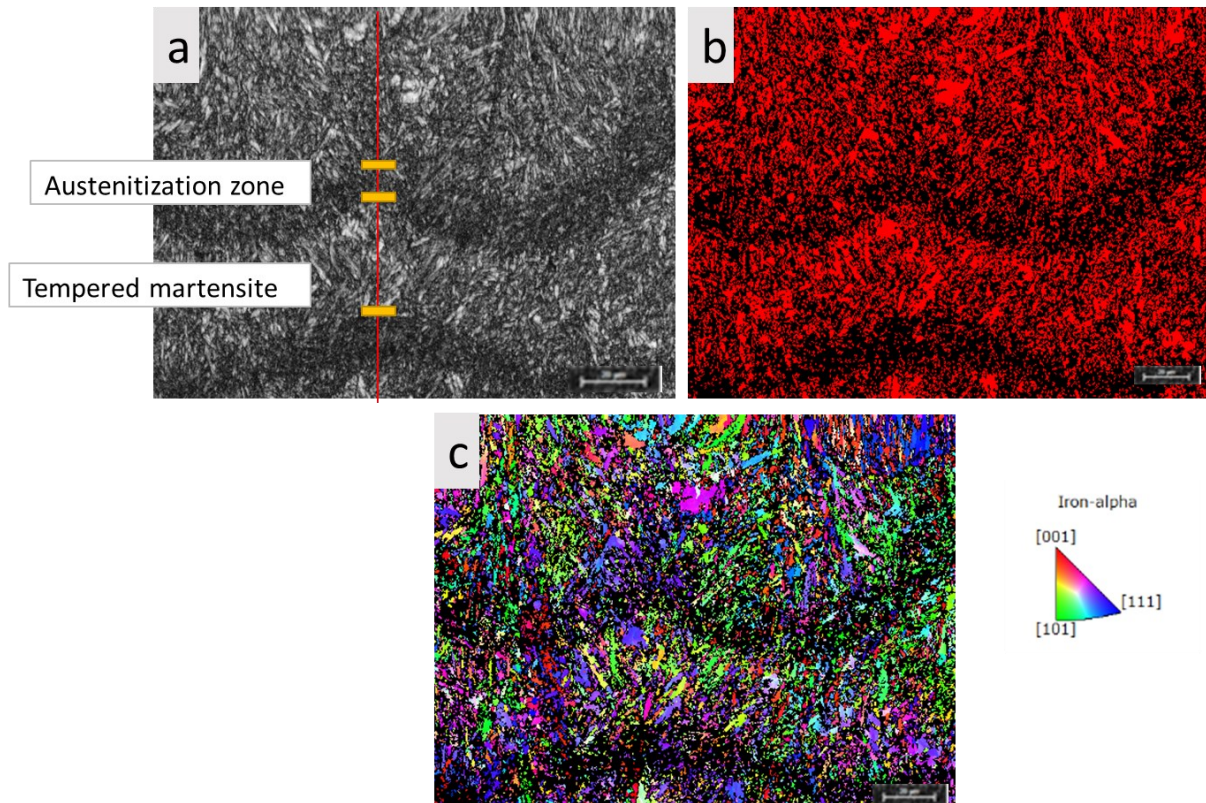


Figure 59: EBSD analysis results of the heat-treated sample until 600°C: a) Pattern Quality, b) Phase Map and c) IPFZ map with its colours legend. In the Phase Map, the red dots correspond to Iron BCC phase.

The third isothermal treatment was held until 900°C. From SEM micrographs it was clear that another microstructure had been formed (Figure 60). This means that austenitization was reached and recrystallization has happened.

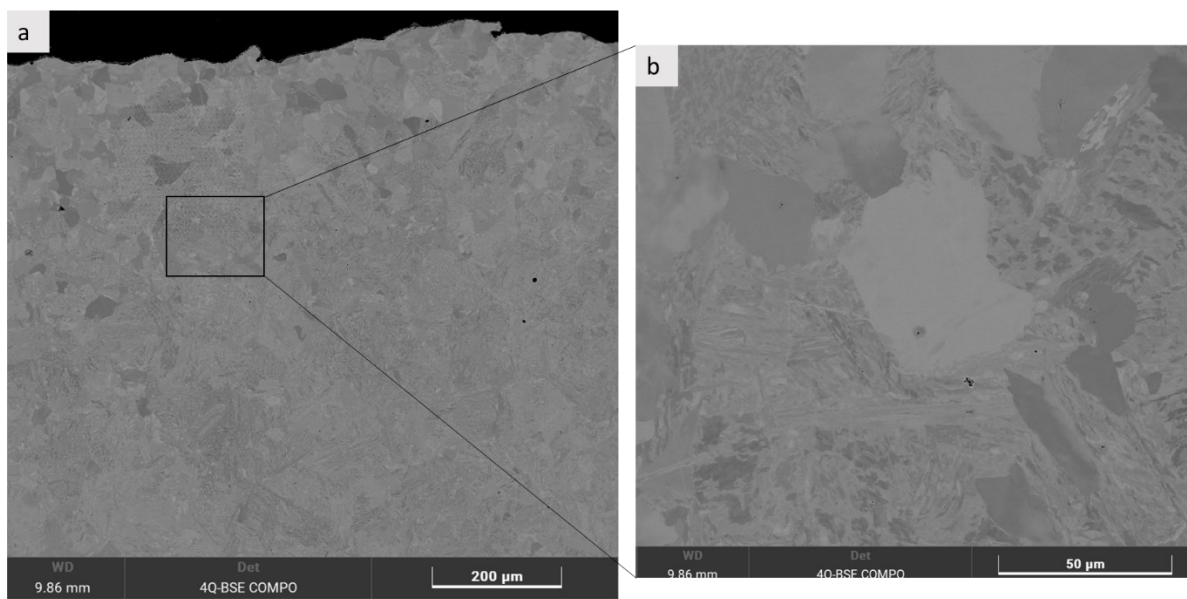


Figure 60: a) SEM micrographs of the cross-sections of the piece after the heat treatment until 900°C; b) zoom-in on the microstructure.

### 4.3.5 Hardness analysis

In order to obtain a deeper understanding of the mechanical properties of the samples, hardness tests were performed, both on macro and nano scale. These tests were made only to the three selected specimens based on the  $E_d$ : 08, 12 and 13.

The outcomes of the macrohardness tests showed no significant differences along the cross-sections of the samples. However, among all of the three tested pieces, a much higher value of Vickers hardness was obtained in the area of the top layer, as it is shown in Figure 61. Moreover, the outcomes of the comparison between the three specimens macrohardness is displayed.

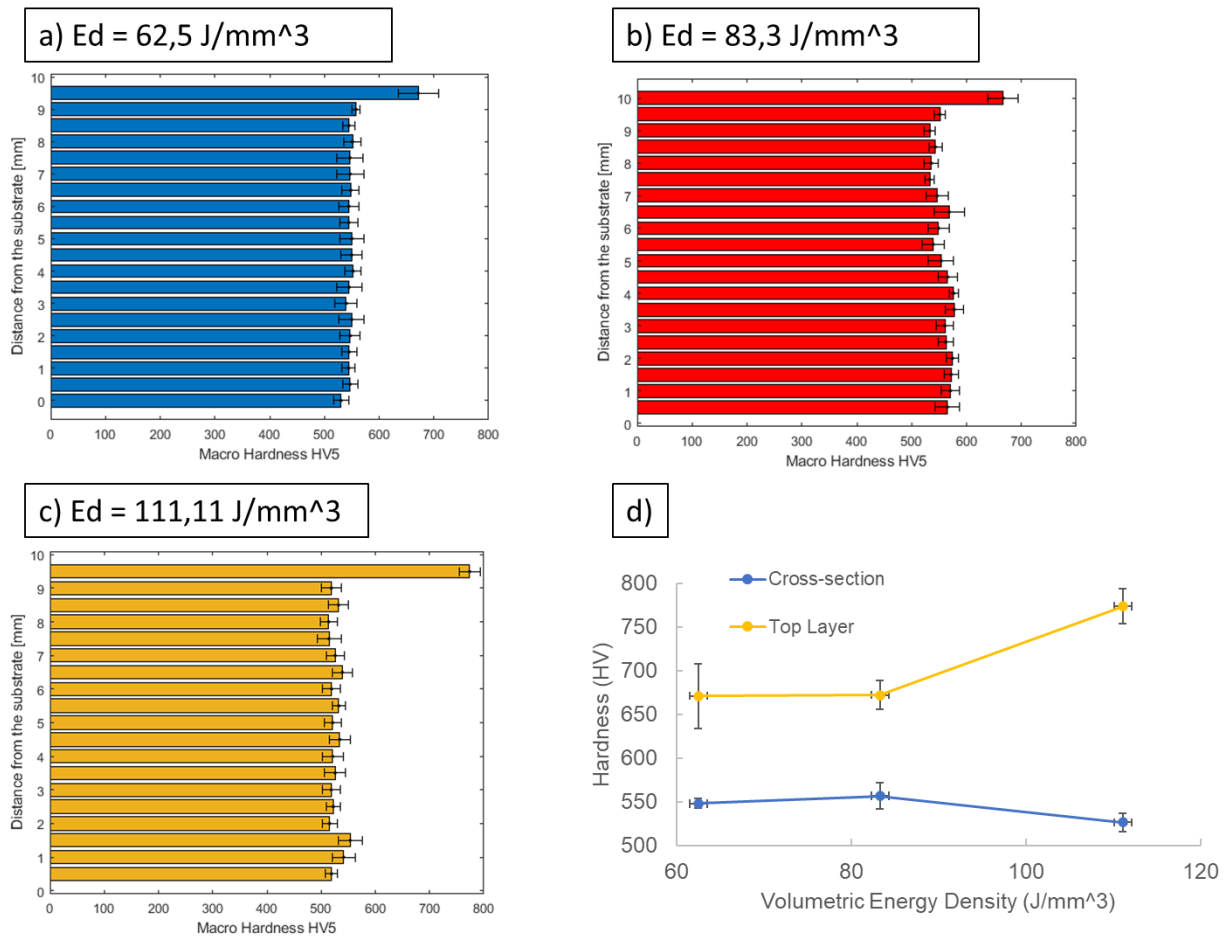


Figure 61: Graphic results of the macrohardness tests on the three selected samples (a,b,c) and graphic comparison between their overall hardness on the cross-section and top layer (d).

Regarding the nanohardness tests, it was held as well to the same three samples (sample 08, 12, 13), one symbolic graph will be shown in Figure 62. In the graph, it was possible to identify four different areas of hardness, which were correlated to four different microstructures, as it has been described in the section 4.2.3.

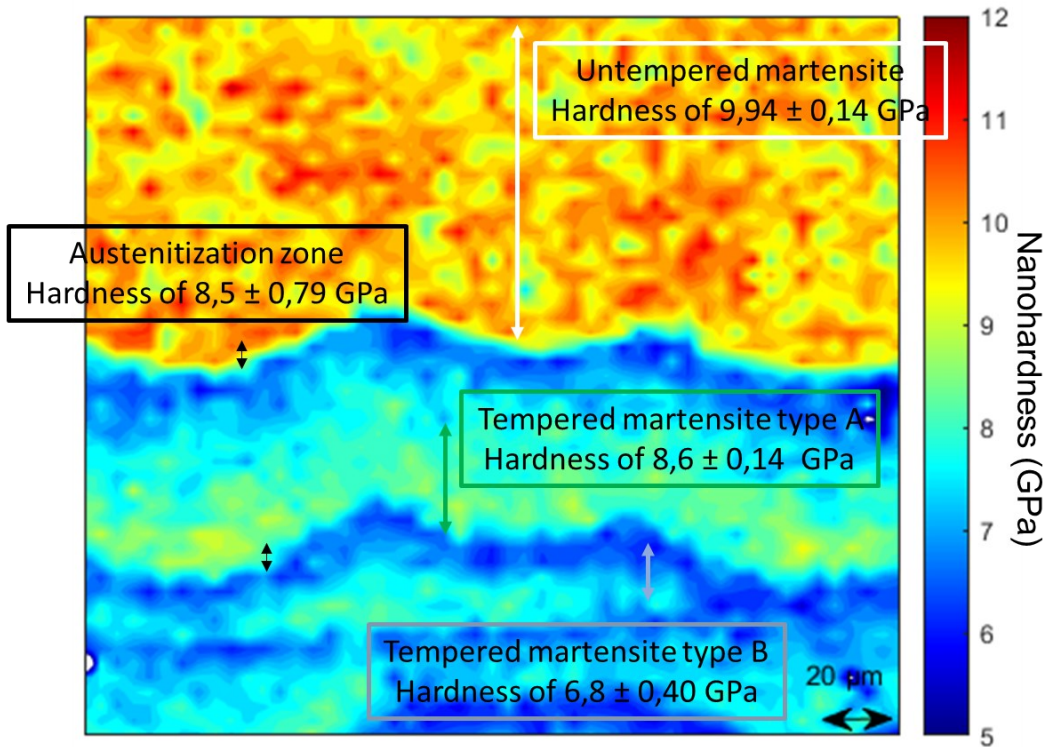


Figure 62: Nanohardness test results on the as-built sample.

However, some little differences of the hardness values of each of the four areas were identified. The latter ones are displayed in the graph of Figure 63.

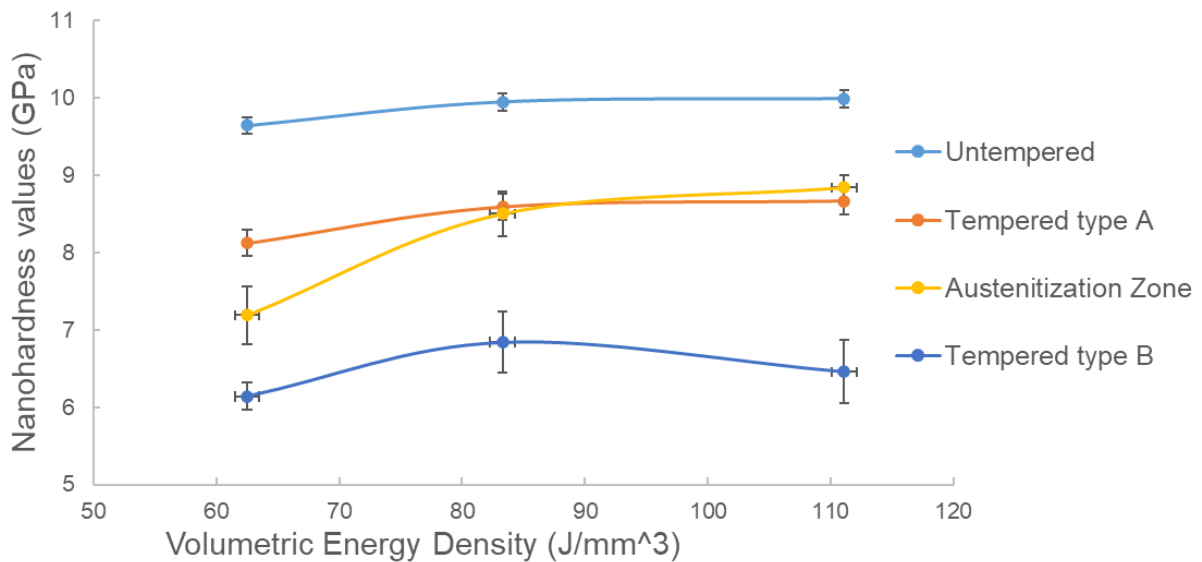


Figure 63: Different values of Nanohardness among the three selected as-built samples.

Furthermore, the nanohardness evaluation was held to the samples which were subject to the isothermal treatment until 600°C (Figure 64a) and 900°C (Figure 64b).

From the results it was possible to see that in both of the cases the heat treatment caused

a reduction on the hardness value. This reduction was higher in the specimen heat treated until 900°C (average of 4,07 GPa) than in the one up to 600° (average of 5,56 GPa). Moreover, from the outcomes it was clear that the different areas which had been detected in the as-built samples (Figure 62) were no longer visible.

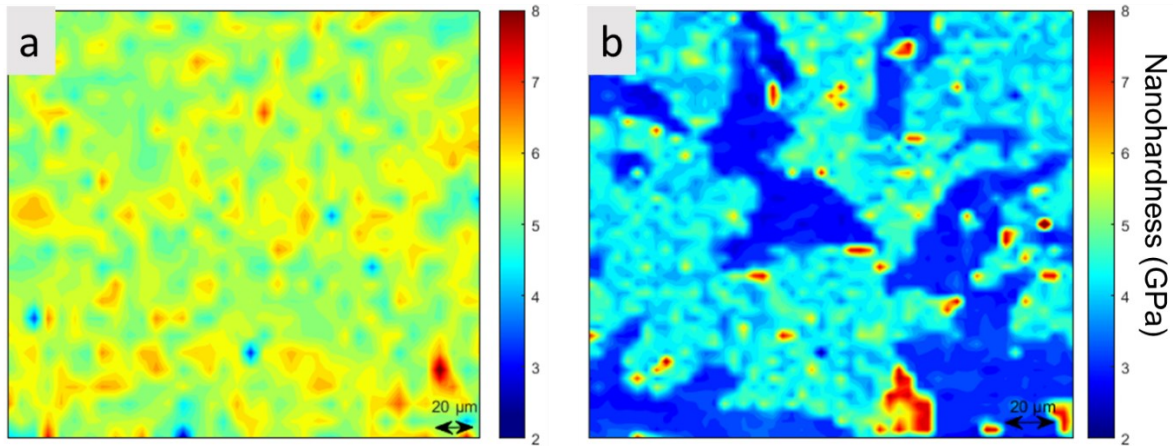


Figure 64: Nanohardness test results on the heat treated samples a) until 600°C b) until 900°C.

#### 4.4 Summary of the results

In order to reach a clearer understanding of the above illustrated results regarding the microstructure, a brief resume will be given in this paragraph.

To begin with, due to the bidirectional laser scan strategy of 90° in the x-y plane, as the analysis on the microstructure of as-fabricated samples showed, a layered appearance of melt pool structures (Figure 48). On the top part of the cross section, the thickest layer was present, containing the original melt pool, which showed a stark contrast with the layers below in all kinds of micrographs (OM, Figure 49 and SEM, Figure 52). The rest of the cross-sections was occupied by layers of melt pools. The different parts were distinguished by the clear different chromaticity they had at the OM and at the SEM, showing bright etched and dark etched areas.

A slender central columnar grain was detected crossing all the layers (Figure 54). Such cell was confined to the centre of the melt pool and being vertical. Moreover, starting with the OM micrographs, it was possible to observe that the grains along the centreline of two subsequent layers kept their epitaxial growth across the two melt pools without changing the growth direction. It is significant that this strong phenomenon was visible through OM analysis even before etching (Figure 54a) and through the IPFZ Map performed with the EBSD analysis (Figure 57c). However, among the two EBSD analysis which had been performed, this phenomenon was visible only in the heat-treated sample up to 300°C. Indeed, in the sample

which underwent isothermal treatment until 600°C, no sign of the slender central columnar grain was detected neither in the OM micrographs nor in the EBSD investigation, as well as for the melt pool boundaries and the top layer (Figure 58a, b).

Furthermore, it was observed that at the sides of the central columnar grain within the melt pools, a side-branching phenomenon occurred (Figure 55b). At the side of two adjacent melt pools it was possible to notice a 90° angulation between the side grains, as visible in Figure 55c. Moreover, it was observed that the dendritic arms did not cross the grain boundaries (Figure 55a).

Furthermore, to deeply investigate on the microstructure of the original state and on the HAZ, hardness tests were used as well. From the macrohardness outcome, a strong dissimilarity between top layer and HAZ was observed (Figure 61). While the nanoindentation tests presented even more interesting details, confirming a higher hardness in the top layer as well as showing three different levels of hardness within every melt pool of the HAZ (Figure 62). Thereby matching with what it was possible to see already from microscope observations. Indeed, the different areas characterized by similar value of nanoindentation corresponded to the different etched parts of the OM and SEM micrographs (Figure 50, Figure 51, Figure 52)

Starting from the top layer region, a spike of 9,9 GPa was observed in the as-printed specimen, which was the highest value that occurred (Figure 62) and can be correlated to martensite phase in an untempered state. The presence of martensite matrix was confirmed by the EBSD analysis, where the phase map indicated that the detection was mainly of Iron BCC (Figure 57b and Figure 59b). The EBSD analysis was not possible to achieve using the as-printed samples because of the supersaturated microstructure with distorted crystallographic lattices, indeed these outcomes were held on the heat-treated samples. The martensitic structure was also confirmed by the solidification sequence held after reverse DTA (Figure 56). It had a distinct needle-like morphology (Figure 52a). The overall matrix resulted as highly supersaturated, therefore only a few segregation were possible to be detected (Figure 53a). Moreover, inside of this untempered region of the as-fabricated samples, it was possible to distinguish the melt pool area and another portion of untempered martensite below the melt pool boundary (Figure 50b).

While further away from the melt pool boundary, alternating layers of various degrees of tempered martensite were observed, showing anisotropic nanoindentation. The two different areas within the melt pool which were distinguished were called “tempered martensite type A” and “tempered martensite type B”. The latter one presented a reduction of hardness of the 30%, while the type A only of the 13% (Figure 62), if compared to the untempered state. The differences between the two tempered areas were also detected in terms of microstructure (Figure 51, Figure

52b). As the EDS analysis proved, in the tempered region white nano-scale precipitates were observed within the laths of martensite, especially in the martensite type A (Figure 53b).



## 5. DISCUSSION

### 5.1 Determination of the Process Map

As previously explained in the section 2.2.1.2, Selective Laser Melting is a technology for which the mechanical properties of printed metal parts are highly dependent on the printing parameters that influence the value of the laser energy density. As a consequence, the tailoring of the proper process framework is very important for the manufacturing, reason why a deep investigation on the quality of the as-fabricated parts was held.

The 20 samples utilized for this study were printed using two variable parameters and two fixed ones (section 3.2.2). Indeed, the power ( $P$ ) and the laser scan speed ( $v_s$ ) were combined differently in each samples. Thus, in total the process had three parameters which varied during the printing procedure:  $P$ ,  $v_s$  and  $E_d$ .

Considering the results obtained, all the 15 fully printed samples were compared in terms of density, presence of defects, pores distribution, tracks overlapping and surface quality. The other 5 specimens could not be processed until the desired height, therefore the causes for such failure were investigated as well.

From the outcomes it was seen that combinations such as low laser scan speed and low laser power (samples 1, 2, 3, 6, 11), were found to generate pieces which could not be fully printed (Figure 23a). Indeed, being both the  $v_s$  and  $P$  very low, the process could not ensure that the melt pool was large enough for receiving and melting the metallic powders [71]. Moreover, in the situation of  $E_d$  higher than  $100 \text{ J/mm}^3$  (samples 1, 6, 11), spattering phenomena becomes crucial for the un-processability of the samples. If the spatters adhere to the surface of the printed parts and are larger than the layer thickness ( $30\mu\text{m}$ ), these particles impede the circulation of the new powders, thus generating an inhomogeneous layer of powders. Therefore, during the subsequent passage of the laser the phenomenon increases until reaching printing-failure since the process cannot go on anymore. In addition, this excessively high energy input was reported to yield increased crack densities due to intensified residual stressed [4], which may also be a cause of the impossible processability. However, considering the whole broad range of  $E_d$  ( $52\text{-}166 \text{ J/mm}^3$ ) this cannot be the unique explanation. The printing process led to failure because of unforeseeable excessive presence of defects such as lack of fusion porosity, cracks, gas porosities and key-holes. Ultimately this situation results in the un-processability through this set of parameters and therefore should not be pursued.

On the other hand, the combinations of low laser power and medium-high laser scan speed, showed the lowest values of density (Table 7, sample 04, 05, 07, 10). The high presence

of defects and porosities is due to a bad overlapping of the track lines (Figure 48a), as consequence of a low  $E_d$ . Especially regarding the realisation of sample 04 and 05, the low  $E_d$  (respectively, 41,67 and 34,72 J/mm<sup>3</sup>), led to a little and unstable melt pool (Figure 49d), resulting in lack of fusion areas. Indeed, the melting ability of the powder decreases with low energy input [10]. Moreover, if together with fast laser scan speed, the cooling rate of the melt pool will be accelerated leading to the realising of gas bubbles which cannot be discharge and therefore will turn into gas porosities [10]. Although among the samples the majority of the porosity had D50 values below 40  $\mu\text{m}$ , they all presented several pores with a D50 above 300  $\mu\text{m}$  as well (Figure 47a). In addition, as low energy input results in poor laser remelting, it can significantly enhance the level of surface roughness present because the un-melted particles are less likely to be re-absorbed [72] (a). All in all, these combinations of process parameters showed unpromising effects in the printed pieces properties.

Furthermore, the combination of high laser power and high laser scan speed revealed a relatively low density too (Table 7, sample 14, 15, 19, 20), according to a quite high level of porosity identified (Table 8, Figure 43). This level of porosity is presumably related to the poor overlap quality between the melt pools in addition to the balling phenomena, which is enhanced by the high laser power input [72]. For the latter reasons, there were detected many microscopical powder balls, leading to the presence of numerous irregularities such as peaks and valleys on the top surfaces. Despite the fact that a couple of bigger pores with a D50 of 100  $\mu\text{m}$  were detected in every piece, their average diameter was around 30  $\mu\text{m}$ . Therefore, this investigated process window brings about a not enough decent level of quality.

The combinations of high laser power and low scan speed resulted as having a high density value (above 99,5%, Table 7). Despite this, especially in sample 16 and 17 due to their very high volumetric energy density input (respectively, 208,33 and 138,89 J/mm<sup>3</sup>), the original melt pool size resulted as very large (Figure 49c) and unstable (Figure 48c). As a consequence, as it has been already explained, the spattering behaviour was found to be extremely stronger (Figure 38e) than in the other pieces. Not only the spattering intensity increased, but also did the number of powder spatters (Figure 45). When the layers are stacked to produce parts, the spattering impurities between layers cannot be removed, therefore, they accumulate and contribute to internal defects within the parts until the top surface is reached [26]. Indeed, the pieces presented all kinds of defects (Figure 43, sample 16, 17, 18). The pores detected had an average D50 of 20  $\mu\text{m}$ , however they presented sizeable pores as well with a D50 up to 500  $\mu\text{m}$  (Figure 47c). Therefore, by using high laser power and low laser scan speed as process parameters, highly dense parts can be printed, however they will present large spatters.

Ultimately, the combination which resulted as having the best properties was characterized by a medium value of  $E_d$  (from 50 to 111,11 J/mm<sup>3</sup>) and limited defect content (Figure 43, sample 08, 09, 12, 13). In this investigated process window, no remarkable issue was identified regarding the cross-section and top surface quality of the pieces (Figure 38 b, c, d). Indeed, only in this situation the scan tracks properly overlapped (Figure 48b), as a consequence a very regular medium-size top layer was analysed (Figure 49b). The porosities which were detected in the cross-sections were only present in the form of gas porosities, indeed the average size of the pores resulted as being 15-20  $\mu\text{m}$  with the biggest pores not exceeding a  $D_{50}$  of 70  $\mu\text{m}$  (Figure 47b). It is important to recall that this kind of porosity, differently from lack of fusion pore or keyholes, do not affect the development of the microstructure [25]. The pieces resulted as basically defect-free, indeed no crack or spatter was detected. However, considering the nature of SLM technology as a layer by layer stacking powders process generated by a fast-moving laser, a minimum amount of surface roughness is always to be found (Figure 38 b, c, d), but it should not represent any concern. All in all, these sets of parameters were therefore considered as optimum for the realisation of AISI S2 metal parts through SLM technology. For the latter reason, these samples were used for the following microstructure investigation and hardness evaluation.

Cracks (Figure 44) on the side of the cross-sections were found in a few samples. The reason might be related to the high carbon content of AISI S2, which guarantees a transformation from austenite to carbon martensite and the latter is of course susceptible to cracking due to its low ductility [4]. However, the presence of cracks might also be caused by the support structure to the base plate, which can trigger cracks because of a notch effect. Another reason can be the force of cutting tool used to prepare the samples, which can cause inner tensions to initiate cracks.

At this point, based on the above mentioned considerations obtained from the macroscopic characterization of 15 samples while considering defects occurrence (within the bulk, or on cross sections), Figure 65 was drawn out. This figure is ascribed to a process map which gives an idea about the optimized parameters used to achieve the realization of fully printed SLM metal parts with high density, low porosity and zero presence of defects.

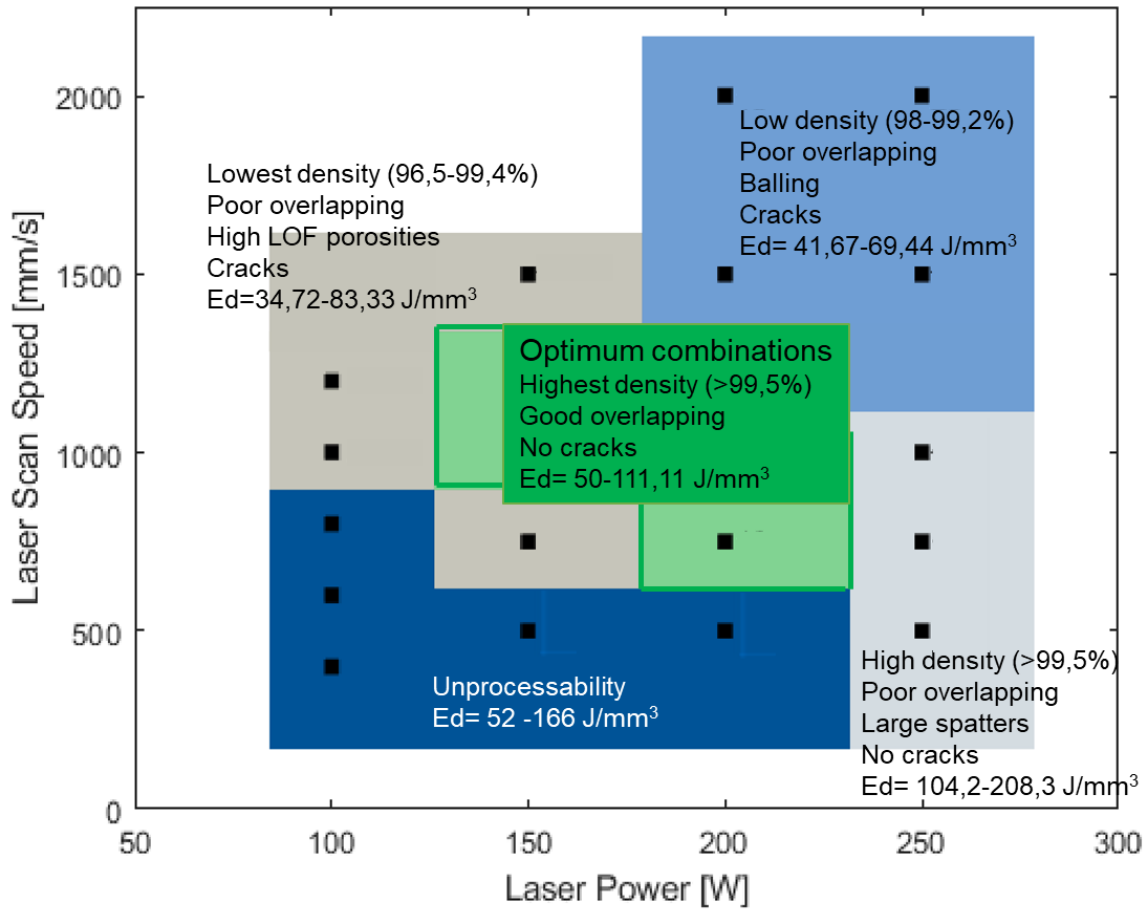


Figure 65: Process map with regards to the printing of AISI S2 metal parts through SLM technology.

The above-shown process map can also be used as an indication for other 3D-printing processes, by simply applying justified shifts.

To begin with, other kinds of alloys printed by SLM seem to present the same kind of defects as the ones found in this work, following a slightly equal attitude towards the values of the process parameters. For instance, in the situation of alloys with a higher content of Carbon, an optimum laser energy density of 70-100 J/mm<sup>3</sup> was found to be pursued [3], [73]. While Fe-rich alloys showed a situation where a volumetric energy density around 60 J/mm<sup>3</sup> was needed [1], [2]. This allows to conclude that by increasing the carbon content, the optimum process area might have to be slightly shifted to the low-right. While by decreasing it, it should be moved to the top/top-left part of the graph. In the different situation of high-silicon alloys, the energy density required was found to be around 40 J/mm<sup>3</sup>, therefore shifting the optimum process window to the top-left [10]. While for stainless steel the process map should be moved towards values closer to 130 J/mm<sup>3</sup> in the bottom-right [74].

Not only the initial powder used, but also the way it was produced might influence the optimum process area location. For instance, if the powders are produced through Water

Atomization (WA) instead of Gas Atomization (GA) as they were in the current work, they will reach an irregular morphology and, even more relevant, they will acquire a higher content of oxygen [51]. As a result, high densification of WA powder requires slightly higher laser power than when processing GA materials. Therefore, the optimum process window will need to be shifted to the right side of the graph.

Meanwhile, the use of a different scan strategy will strongly influence the analysis as well. In this present work a strategy of 90/90° was used for all the samples. However, in literature is more common to find printing processes which make use of a 67° strategy since it brings out a helical growth [25] which is less-likely to encounter cracking. Indeed, scan strategy has an important influential role in controlling texture, residual stresses and cracking behaviour [25]. This feature includes many aspects to be taken into account, however, previous studies found approximately the same optimum process windows as the one developed in this work [2], [75].

All in all, the determination of the process map shown in Figure 65 can give a good indication of what to expect when performing printing procedure by SLM, in terms of density and defects. Moreover, although the map was generated from the analysis of AISI S2 steels with certain fixed conditions, it was demonstrated that the equal can be used for other kinds of processed material or in other printing conditions as well, by simply applying proper shifts.

## **5.2 Microstructure evolution during the SLM process**

Despite the benefits that SLM techniques offers, there is limited use of this process to print low-alloyed steel. One of the reasons is the little understanding of the as-built prior microstructure of the pieces [3]. It is indeed a complex mix of supersaturated phases together with distorted crystallographic lattices that form, which it is not straightforward to deeply characterise. In the situation in which an EBSD analysis was attempted, no clear results were firstly obtainable, due to the complex heterogenous microstructure. Only after a stress-relief heat treatment it was possible to achieve useful results.

The SLM conditions in which the metal parts are fabricated are out-of-equilibrium, with temperatures above the melting point and rapid cooling rates. These conditions provoke a microstructural and chemical inhomogeneity inside the pieces [76]. The characterization of the microstructure aims to establish the nature of the phases present and the possible phase transformations which could have taken place during the fabrication. A wider knowledge might indeed help mitigate the effects of this large anisotropy on the properties of the as-built parts and perhaps enhance the feasibility of using such metal alloys with high carbon content in industrial applications.

Furthermore, being this technology a layer by layer deposition process, numerous cycles of re-heating occur, which induce an intrinsic heat treatment that progressively tempers the material in situ [73]. It is indeed paramount to firstly characterize the original untempered state, since it is the only way to understand how the primary microstructure purely was. These findings will later help to fully understand the tempering phenomenon of such kind of microstructure.

The latter analysis of the induced heat treatment on the as-built pieces is very important for the current study because it can provide the prediction and tailoring of the microstructure [12]. Therefore, it also holds the potentiality to alleviate the need for post-processing of high carbon content alloys and help expand the production capability of SLM [73].

### 5.2.1 Solidification sequence

As in this paragraph will be fully explained, thanks to the analysis of the OM, SEM and EBSD images, it was possible to investigate the solidification structure of the as-built samples.

In the molten region, the original microstructure after solidification is fully austenitic which, upon rapid cooling, transforms completely into martensite. The use of a reverse DTA analysis (Figure 56) allowed to restore the solidification sequence that occurred during the fabrication process and it confirmed the presence of martensitic structure. The analysis showed that the peritectic transformation (1400 – 1500 °C), where  $\delta$  ferrite and liquid transformed into austenite, took place. The peritectic transformation resulted in the nucleation and growth of austenitic grains which grew epitaxially within the melt pool. These grains consist of a cellular dendritic microstructure, due to the high ratio G/R of SLM processes (Figure 15). The reverse DTA curve showed a peak at 760°C which was correlated to the transformation of austenite into martensite, as a consequence of the high cooling rates ( $10^5$ - $10^6$  K/s). Moreover, the high cooling rates led to the formation of distorted lattice due to the presence of more elements within the conventional lattice compared to equilibrium conditions. This means that a supersaturated martensite was formed upon cooling.

The so called ‘epitaxial grain growth’ occurs due to the continuous growth of grains from a previous melt pool to a new melt pool. Indeed, the scan strategy used in this SLM process indicates that columnar growth was favoured and epitaxial growth as with cellular dendritic structure was dominant because of the G/R value [25]. More precisely, the growth develops as columnar grains with different orientations following the building direction and shortly after these grains become very slender and elongated towards the same direction of orientation (Figure 54). Indeed, during the solidification, the grains tend to grow towards the centre of the melt pool in the travel direction of the laser beam, which corresponds with the direction of the maximum temperature gradient and hence maximum heat extraction.

It is significant that among the two EBSD analysis which had been performed, this phenomenon was visible only in the heat-treated sample up to 300°C, because in the case of 600°C the heat treatment caused a new crystallographic arrangement, not only a minor stress relief situation. Indeed, in the sample which underwent isothermal treatment until 600°C, no sign of the slender central columnar grain was detected neither in the OM micrographs nor in the EBSD investigation, as well as for the melt pool boundaries and the top layer (Figure 58a, b). This is due to the temperature reached that resulted in a higher change of the microstructure.

Furthermore, it was observed that at the sides of the central columnar grain within the melt pools, a side-branching phenomenon occurred, as the existing grains followed the direction of thermal gradient. Therefore, while the epitaxial growth is responsible for the slender columnar grains confined to the centreline of melt pools, side-branching enables crystals to follow drastic changes on their orientation at the side of melt pools [25]. Indeed, if the growth direction of existing crystal cells is misaligned to  $G$ , cells are still able to epitaxially grow, but with a change in their growth direction [25]. However, while the building direction does not change across the cross-section,  $G$ , in contrast, gradually changes direction when approaching the sides of the melt pools, not anymore being vertical but instead oblique. The micrographs that were analysed of the as-produced samples (Figure 55b), clearly show the change on the growth direction between the sides and the centre of the melt pools. This confirms the strong relationship between heat flux and growth direction of the grains.

A sketch of the microstructure evolution during the different stages of the process is provided in Figure 66. This aims to highlight how the building direction used, which was perpendicular to the build plate, was able to cause drastic changes on the growth direction of crystal within the melt pools.

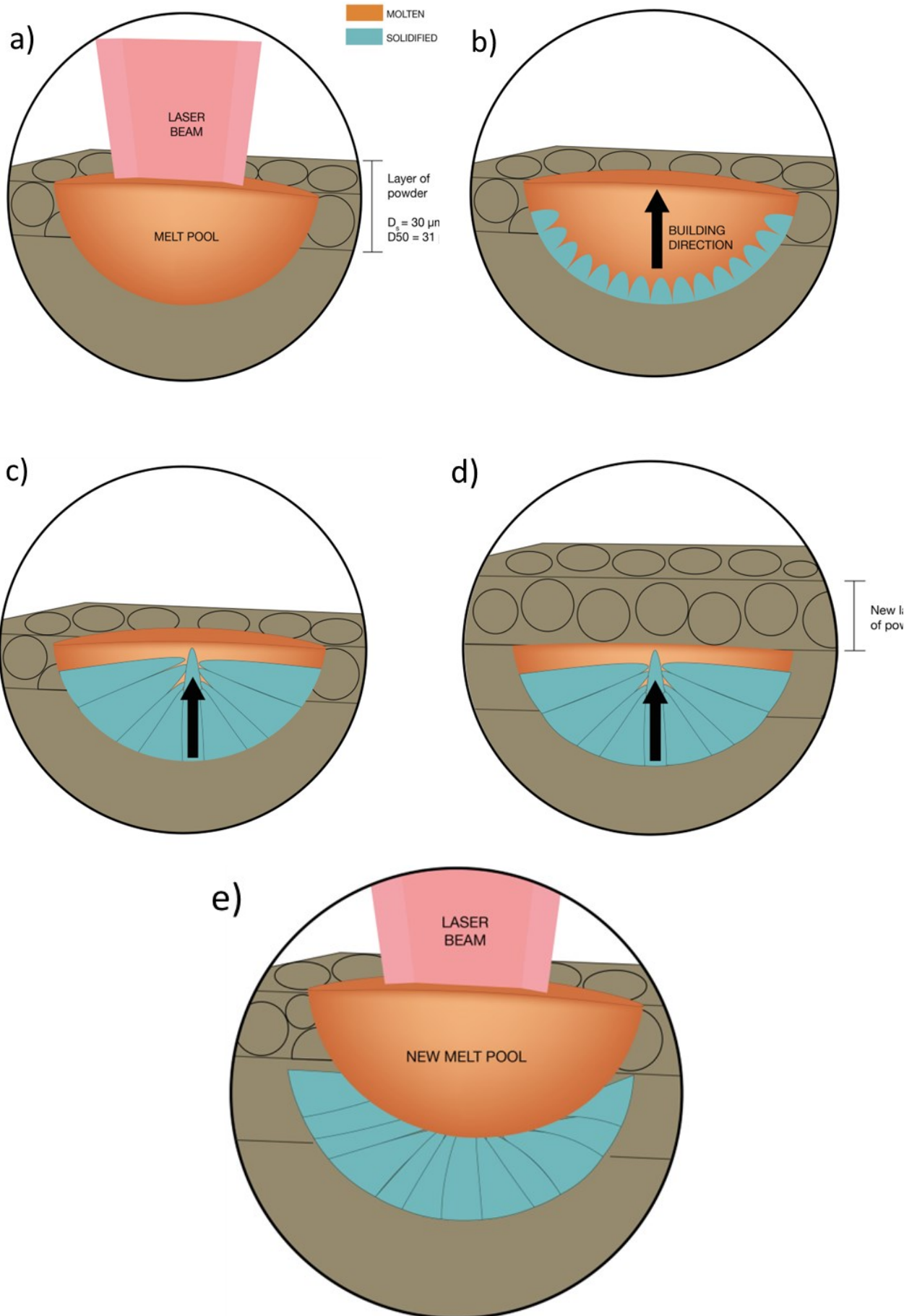




Figure 66: Sketch of the process of melt pool solidification. (a) Melt pool with molten powders after the laser travels by; (b) primary nucleated grains following the orientation of the building direction within the melt pool border (c) epitaxial growth with side-branching phenomenon of the nucleated grains (d) addition of a new powder layer (e) the process new step, which affects the microstructure of the layers below.

Moreover, starting with the OM micrographs (Figure 54), it was possible to observe that the grains along the centreline of two subsequent layers kept their epitaxial growth across the two melt pools without changing the growth direction, as explained above. A sketch of this situation was provided in Figure 67a. Meanwhile, at the side of two adjacent melt pools it was possible to notice a 90° angulation between the side grains, as illustrated in Figure 67b and visible in Figure 55c.

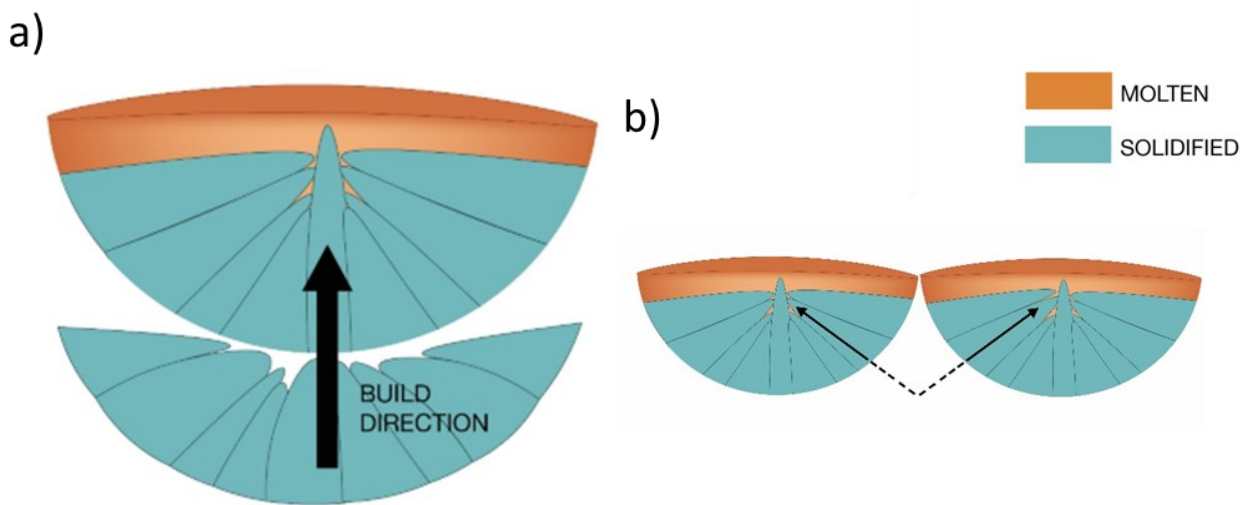


Figure 67: Sketches of two features of epitaxial growth: (a) of columnar grain growth which stays in the same direction along subsequent layers (b) of the side-branching phenomenon between two adjacent melt pools forming a 90° angulation.

Moreover, a post treatment up to 900°C was also performed, as to look for confirmation of the theories which were until this point made. As expected, too high temperatures, above the austenitization peak, led to recrystallization (Figure 60). This outcome demonstrates how SLM process involves out-of-equilibrium conditions which generate a microstructure that is far distant from the conventional methods one. Indeed, the cooling rate strongly influences both undercooling and solute partitioning, therefore a different value turns into much difference microstructure. On the other hand it was relevant to see in the case of future perspectives how the hardness value on the heat-treated samples significantly decreased (Figure 64). This proves that for specific applications, a desired hardness value might be reached by applying straightforward isothermal treatments up to specific temperatures.

### 5.2.2 Effect of in-situ thermal cycle

Due to the layer-wise manner building of SLM, as explained in the previous sketches, parts develop in different directions and present anisotropies in both microstructure and mechanical properties [71]. This is because solidified layers below the new melt pool are affected by the repetitive cyclings of heating and cooling. For the latter reason, the area below the melt pool is called Heat Affected Zone (HAZ). In this work, the prior microstructure present in the top layer area and the HAZ of the optimum samples (sample 08, 12, 13, Figure 65) was investigated.

What the heterogenous microstructure and hardness distribution revealed is a mixture of tempered and untempered martensite bands in the as-printed parts. These bands were attributed to the thermal cycling effects of the layer by layer deposition associated with SLM process, which is characterized by a really complex thermal history. Every time that a new layer is deposited, the out-of-equilibrium conditions strongly affect a certain amount of layers below. Bright and dark regions are observable in the as-built micrographs and represent varying degrees of tempering in the specimen, as the hardness evaluation confirms. Indeed, in the HAZ, metastable phases with mixed compositions formed at high cooling rates dissociate in more stable phases due to local reheating up to the solidus temperature.

Starting from the untempered region, since no layers are deposited above the top layer, tempering does not happen as in the rest of cross sections does. Besides this, another important factor is that certain alloying elements like Cr, W, Mo, C and Co impede precipitation of carbides in martensite by affecting the diffusion rate of carbon in the supersaturated solid solution so that martensite can retain up to 450–500 °C [12]. Although the S2 is a low-alloyed steel, it contains a certain amount of Si, Mo and C. It was therefore assumed that in the upper layers the martensitic structure remained virtually unaffected due to the presence of these alloying elements and the kinetic factor [12].

Moreover, inside of the untempered region of the as-fabricated samples, it was possible to distinguish another portion of untempered martensite below the melt pool boundary (Figure 48b). When this area will be affected by a new layer deposition, it will be exposed to temperatures above the austenization temperature, leading to re-austenization of this part. For the latter reason this section was called “austenization zone”, an area which will later transform back into tempered martensite but experiencing a little reduction of hardness if compared to the other tempered areas.

While further away from the melt pool boundary, alternating layers of various degrees of tempered martensite were observed. Indeed, here the material experienced high temperature but

below the critical point, therefore leading to simple tempering of the existing martensite. Tempering causes softening of martensite owing to the diffusion of carbon out of the martensite lattice, indeed nano-scale precipitates were observed within the laths of martensite. However, because of the short cycle times the diffusion was limited. Apparently, carbon atoms could diffuse short distances and along more defected areas, in this case the cell boundaries [12]. It is also possible that cementite precipitates were present in the as-built condition, due to the thermal cycling and effective tempering, but they were probably too fine to be observed under SEM. Within the tempered region inhomogeneity was again detected resulting also in anisotropic nanohardness. The two different areas within the melt pool which were distinguished were called “tempered martensite type A” (13% hardness reduction) and “tempered martensite type B” (30% hardness reduction). These two areas represent the effect of a solid-state solution transformation. It was assumed that the transformation concerned desaturated martensite phase only, but as the nanohardness values varied a lot it is very likely that bainitic and retained austenite phases were present as well.

Whereas after the isothermal heat treatment up to 600°, the microstructure seemed much more stress-relieved, indicating that the diffusion of carbon from the supersaturated matrix effectively happened (Figure 58c). Indeed, small inclusions were observable as bright white spots. Martensitic laths found in the heat-treated condition were thinner than those observed in as-printed materials, suggesting that grain refinement took place as well. Moreover, it is important to highlight that after the isothermal treatment, the top layer was no longer made of a different microstructure nor a different hardness value, meaning that the treatment effectively affected all the cross-section. This outcome proves that the heat treatment which occurs during the SLM process is a tempering up to 600°C.

Another relevant result was that after the macrohardness test, the HAZ presented a decrease on the level of hardness of the 18% in the conditions of medium-low  $E_d$ , up to the 30% with higher  $E_d$  (Figure 61). The nanohardness of all the four areas seemed to slightly grow its value with increasing input of  $E_d$ . The only exception was the tempered region type B, which seemed to rather vary than simply increasing at different values of  $E_d$  (Figure 63). Similar situation of the type B, was detected in the macrohardness evolution of HAZ (Figure 61d). It is paramount to understand how the properties like hardness change their value at different input parameters, in order to allow not only the microstructure investigation but also the tailoring of the mechanical properties as well.

In the framework of the printing of high carbon steels through the SLM technology, the in situ tempering can allow the reduction of the need for post-processing and therefore enhance

such production capability. Reason for which, a sketch of the solid-state solution detected in the printed samples is provided in Figure 68.

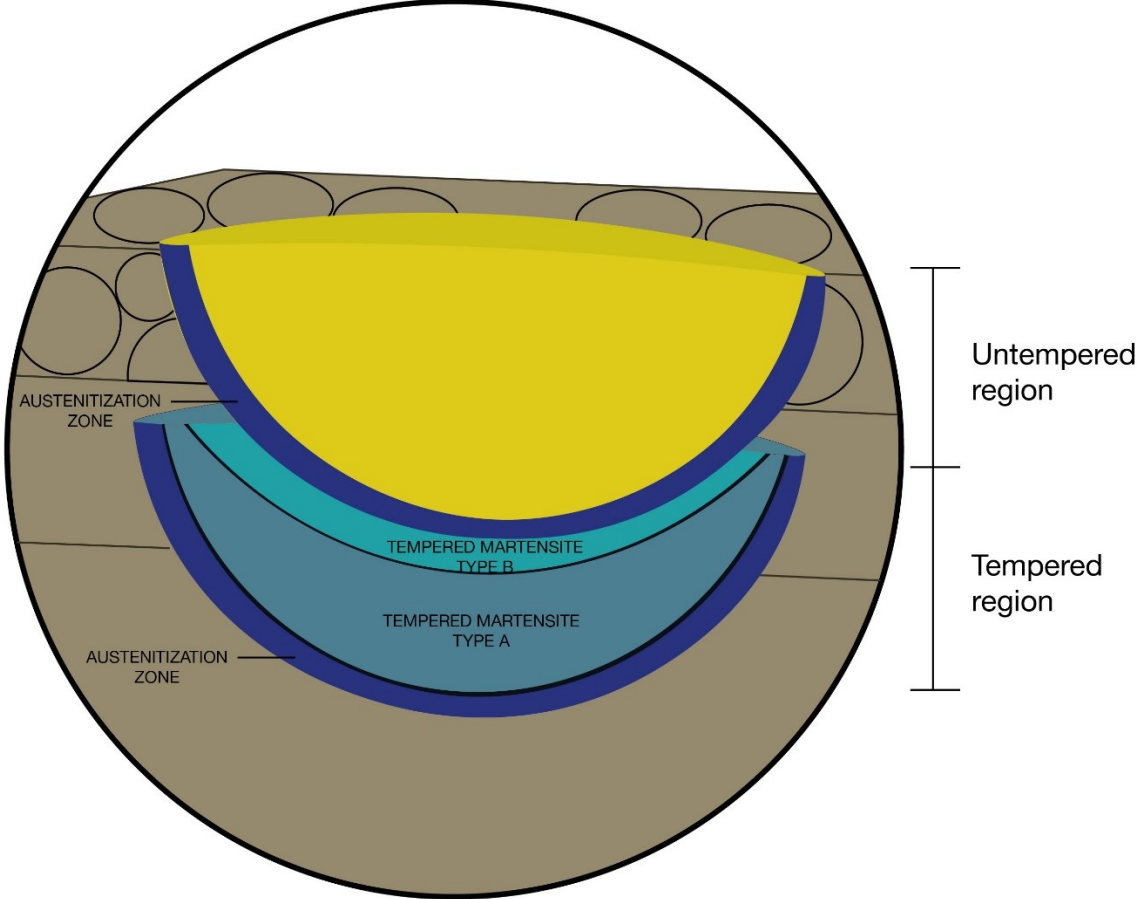


Figure 68: Model of the in-situ tempering effect.

## 6. CONCLUSIONS

In the present study several experiments have been carried out to investigate the properties of the processed AISI S2 parts printed by SLM in the as-built conditions and after post isothermal heat-treatment. From the outcomes of the latter, the following conclusions can be drawn out:

- AISI S2 powders can be successfully printed using SLM process while properly tuning the processing parameters, especially the laser power and laser scan speed.
- Based on the volumetric energy density input, which is the result of the combination of the main processing parameters, a process map can be drawn out. The latter gives an overview of the fields achieved regarding flaws distribution, leading to defect-free or fully dense parts obtained after using optimized processing parameters. The optimum parameters range was between 150 and 200 W for the laser power, and between 750 and 1250 mm/s for the laser speed scan, thus leading to a  $E_d$  of 50-110 J/mm<sup>3</sup>. This outcome provided the ideal process window to produce AISI S2 metal parts through SLM.
- $E_d$  values below 50 J/mm<sup>3</sup> develop severe levels of porosity (lack of fusion, key-holes and gas porosities), while values above 110 J/mm<sup>3</sup> enhance the spattering phenomenon.
- The as-built samples showed a layer-wise microstructure that is due to the scanning strategy. The microstructure is made of columnar epitaxial grains with cellular dendritic structure. There is a variation of the macrostructure depending on the location within the initial melt pool. Grains grew vertically following the thermal gradient direction in the centreline of each melt pool, while at the sides of the centreline, the misalignment of the thermal gradient promoted a side-branching phenomenon.
- The solidification path during SLM processing may involve formation of prior delta ferrite as the first solid prior to a peritectic reaction which leads to austenite that is later transformed into martensite in the solid state. This occurs under high thermal gradients and under out-of-equilibrium conditions. Restoring the solidification sequence has been achieved using the reverse DTA approach.
- The structure observed at a macro scale as regards to Vickers hardness measurements, looks homogeneous. Nevertheless, the same structure when it is

considered at a lower scale level seems heterogeneous, because of the existence of alternative bands of both tempered and untempered martensite. The matrix within the centreline of the melt pool in the as-built conditions is made of a highly supersaturated martensite. This supersaturation is still present within the top layer, while in contrast, HAZ still exhibits martensite, but with a lower nano-hardness compared to that of the centreline and with a more stress-released microstructure.

- Two distinct HAZs are present, the first one been located at melt pool boundaries, and the second one being located beneath each layer/track, on the upper part or the melt pool zone. Those two HAZs have got lower nano-hardness compared to the centreline, the decreasing of the hardness was found to being due to the relative reheating cycle that occurs at a local scale during SLM processing.
- The microstructure achieved within the as-built SLM samples still corresponds to out-of-equilibrium structures, that are different from the close-to-equilibrium ones obtained after conventional post thermal treatments carried out using DTA. This suggests that steep thermal gradients that exist during SLM process strongly influence transformations kinetics.

## 7. PERSPECTIVES

As this Master's thesis consists only in a part of a PhD thesis which aims to fabricate new innovative alloy using the SLM process, surely future following works can be pursued. Here some suggestions will be presented:

- XRD and additional EBSD cross-analysis could be performed in order to investigate deeper in the different phases which generated upon re-heating during the process.
- Significant studies showed the feasibility of compounding SS316L steel with SiC to improve the alloy properties. In these terms, it could be interesting to generate a mix of the same carbide with the S2 instead.
- Wear tests can be performed on the S2 as-printed parts, in order to check if the tribological properties showed could be useful for industrial application.
- To achieve a wider overview of the work, the developing of a finite element model to predict the thermal history and the melt pool dimension evolution of the pieces could be really interesting. Moreover, the numerical results could be later correlated with the experimental outcomes of this work in order to validate them.

## 8. REFERENCES

- [1] J. J. S. Dilip, G. D. J. Ram, T. L. Starr, and B. Stucker, “Selective laser melting of HY100 steel: Process parameters, microstructure and mechanical properties,” *Addit Manuf*, vol. 13, pp. 49–60, Jan. 2017, doi: 10.1016/J.ADDMA.2016.11.003.
- [2] R. Seede *et al.*, “An ultra-high strength martensitic steel fabricated using selective laser melting additive manufacturing: Densification, microstructure, and mechanical properties,” *Acta Mater*, vol. 186, pp. 199–214, Mar. 2020, doi: 10.1016/J.ACTAMAT.2019.12.037.
- [3] J. , G. C. , V. A. et al. Saewe, “ Feasability Investigation for Laser Powder Bed Fusion of High-Speed Steel AISI M50 with Base Preheating System,” *Berg Huettenmaenn Monatsh*, vol. 164, pp. 101–107, 2019.
- [4] J. Platl, H. Leitner, C. Turk, A. G. Demir, B. Previtali, and R. Schnitzer, “Defects in a Laser Powder Bed Fused Tool Steel,” 2020, doi: 10.1002/adem.202000833.
- [5] E. Jelis, M. R. Hespos, and N. M. Ravindra, “Process Evaluation of AISI 4340 Steel Manufactured by Laser Powder Bed Fusion,” *J Mater Eng Perform*, vol. 27, doi: 10.1007/s11665-017-2989-8.
- [6] X. Cui, S. Zhang, C. H. Zhang, J. Chen, J. B. Zhang, and S. Y. Dong, “Additive manufacturing of 24CrNiMo low alloy steel by selective laser melting: Influence of volumetric energy density on densification, microstructure and hardness,” *Materials Science and Engineering: A*, vol. 809, p. 140957, Mar. 2021, doi: 10.1016/J.MSEA.2021.140957.
- [7] W. E. Frazier, “Metal Additive Manufacturing: A Review”, doi: 10.1007/s11665-014-0958-z.
- [8] L. Thijs, F. Verhaeghe, T. Craeghs, J. van Humbeeck, and J. P. Kruth, “A study of the microstructural evolution during selective laser melting of Ti–6Al–4V,” *Acta Mater*, vol. 58, no. 9, pp. 3303–3312, May 2010, doi: 10.1016/J.ACTAMAT.2010.02.004.
- [9] B. Zhang, Y. Li, and Q. Bai, “Defect Formation Mechanisms in Selective Laser Melting: A Review”, doi: 10.1007/s10033-017-0121-5.
- [10] X. Cai *et al.*, “Effect of process parameters on microstructures and properties of Al–42Si alloy fabricated by selective laser melting,” *Heliyon*, vol. 8, no. 6, p. e09680, Jun. 2022, doi: 10.1016/j.heliyon.2022.e09680.
- [11] B. Song, S. Wen, O.C. Yan, Q. Wei, and Y. Shi, “*Introduction and basic principles*,” in *Selective Laser Melting for Metal and Metal Matrix Composites*. Elsevier, 2021.
- [12] P. Krakhmalev, I. Yadroitsava, G. Fredriksson, and I. Yadroitsev, “In situ heat treatment in selective laser melted martensitic AISI 420 stainless steels,” *Mater Des*, vol. 87, pp. 380–385, Dec. 2015, doi: 10.1016/J.MATDES.2015.08.045.
- [13] S. A. Kumar and R. V. S. Prasad, “Basic principles of additive manufacturing: different additive manufacturing technologies,” *Addit Manuf*, pp. 17–35, Jan. 2021, doi: 10.1016/B978-0-12-822056-6.00012-6.
- [14] *Standard Terminology for Additive Manufacturing – General Principles –Terminology*. 2015.
- [15] J. Kranz, D. Herzog, and C. Emmelmann, “Design guidelines for laser additive manufacturing of lightweight structures in TiAl6V4,” *J Laser Appl*, vol. 27, no. S1, p. S14001, Feb. 2015, doi: 10.2351/1.4885235.
- [16] D. Herzog, V. Seyda, E. Wycisk, and C. Emmelmann, “Additive manufacturing of metals,” *Acta Mater*, vol. 117, pp. 371–392, Sep. 2016, doi: 10.1016/J.ACTAMAT.2016.07.019.
- [17] L. E. Murr *et al.*, “Metal Fabrication by Additive Manufacturing Using Laser and Electron Beam Melting Technologies,” 2012.
- [18] A. Mertens, “Personal lesson notes of Techniques de fabrication additive et 3D Printing.” 2018.
- [19] C. Cai and K. Zhou, “Metal additive manufacturing,” *Digital Manufacturing*, pp. 247–298, Jan. 2022, doi: 10.1016/B978-0-323-95062-6.00005-X.
- [20] A. Lawley, *Atomization: The Production of Metal Powders*. Princeton, New Jersey: Metal Powder Industries Federation, 1992.
- [21] <http://www.thermalspraydepot.com/laser-cladding-services/>, “Thermal Spray depot Website (On line 14/07/2022).,” Jul. 14, 2022.
- [22] <http://www.sciaky.com/additive-manufacturing/wire-am-vs-powder-am>, “Sciaky Inc. (On line 23/08/2017).”
- [23] Li C., Liu Z. Y., Fang X. Y., and Guo Y. B, “On the Simulation Scalability of Predicting Residual Stress and Distortion in Selective Laser Melting,” *ASME. J. Manuf. Sci. Eng.*, 2018.



- [24] E. M. Sefene, “State-of-the-art of selective laser melting process: A comprehensive review,” *Journal of Manufacturing Systems*, vol. 63. Elsevier B.V., pp. 250–274, Apr. 01, 2022. doi: 10.1016/j.jmsy.2022.04.002.
- [25] M.-S. Pham, B. Dovggy, P. A. Hooper, C. M. Gourlay, and A. Piglione, “The role of side-branching in microstructure development in laser powder-bed fusion”, doi: 10.1038/s41467-020-14453-3.
- [26] D. Wang *et al.*, “Mechanisms and characteristics of spatter generation in SLM processing and its effect on the properties,” *Mater Des*, vol. 117, pp. 121–130, Mar. 2017, doi: 10.1016/J.MATDES.2016.12.060.
- [27] K. Munir, A. Biesiekierski, C. Wen, and Y. Li, “Selective laser melting in biomedical manufacturing,” *Metallic Biomaterials Processing and Medical Device Manufacturing*, pp. 235–269, Jan. 2020, doi: 10.1016/B978-0-08-102965-7.00007-2.
- [28] “Fraunhofer Institute for Manufacturing Technology and Advanced Materials (IFAM),” <https://www.ifam.fraunhofer.de/en/technologies/laser-beam-melting.html#:~:text=Laser%20beam%20melting%20is%20an%20additive%20manufacturing%20process,to%20melt%20and%20bond%20locally%20at%20these%20points.>, 2022.
- [29] I. Yadroitsev, “Selective laser melting: Direct manufacturing of 3D-objects by selective laser melting of metal powders Quality control and improvement in metal additive manufacturing View project Residual stresses and distortions in selective laser melted parts View project,” 2009. [Online]. Available: <https://www.researchgate.net/publication/259193143>
- [30] J. Kluczyński *et al.*, “The Influence of Exposure Energy Density on Porosity and Microhardness of the SLM Additive Manufactured Elements”, doi: 10.3390/ma11112304.
- [31] J. Wang, S. Liu, Y. Fang, and Z. He, “A short review on selective laser melting of H13 steel”, doi: 10.1007/s00170-020-05584-4/Published.
- [32] T. Kurzynowski, W. Stopyra, K. Gruber, G. Ziólkowski, B. Ku, and E. Chlebus, “materials Effect of Scanning and Support Strategies on Relative Density of SLM-ed H13 Steel in Relation to Specimen Size”, doi: 10.3390/ma12020239.
- [33] S. A. Khairallah, A. T. Anderson, A. Rubenchik, and W. E. King, “Laser powder-bed fusion additive manufacturing: Physics of complex melt flow and formation mechanisms of pores, spatter, and denudation zones,” *Acta Mater*, vol. 108, pp. 36–45, Apr. 2016, doi: 10.1016/j.actamat.2016.02.014.
- [34] Z. Huda, *Strengthening Mechanisms in Metals/Alloys. In: Mechanical Behavior of Materials. Mechanical Engineering Series* Springer, Cham., 2022.
- [35] E. Maleki, S. Bagherifard, M. Bandini, and M. Guagliano, “Surface post-treatments for metal additive manufacturing: Progress, challenges, and opportunities,” *Addit Manuf*, vol. 37, p. 101619, Jan. 2021, doi: 10.1016/J.ADDMA.2020.101619.
- [36] Y. Shi *et al.*, “Overview of additive manufacturing technology and materials,” *Materials for Additive Manufacturing*, pp. 1–8, Jan. 2021, doi: 10.1016/B978-0-12-819302-0.00001-8.
- [37] F. H. Froes and J. R. Pickens, “Powder Metallurgy of light Metal Alloys for Demanding Applications.”
- [38] K. Munir, A. Biesiekierski, C. Wen, and Y. Li, “Powder metallurgy in manufacturing of medical devices,” in *Metallic Biomaterials Processing and Medical Device Manufacturing*, Elsevier, 2020, pp. 159–190. doi: 10.1016/b978-0-08-102965-7.00005-9.
- [39] L. Bayvel and Z. Orzechowski, *Liquid Atomization*, First Edition. Routledge, 1993.
- [40] “Metals – Alloy design and powder production for selective laser melting,” *Advanced Ceramics and Powder Metallurgy*.
- [41] S. Lagutkin, L. Achelis, S. Sheikhaliev, V. Uhlenwinkel, and V. Srivastava, “Atomization process for metal powder,” *Materials Science and Engineering A*, vol. 383, no. 1 SPEC. ISS., pp. 1–6, Oct. 2004, doi: 10.1016/j.msea.2004.02.059.
- [42] W. L. and Y. Biao Z. Z. W. L. and Y. B. Z. Zeng, “Research progress of AM metal materials,” *Shanghai Nonferrous Met.*, vol. 37, no. 1, pp. 57–60, 2016.
- [43] U.S. geological survey, “U.S. Geological Survey, Mineral Commodity summaries 2020,” <https://pubs.usgs.gov/periodicals/mcs2020/mcs2020.pdf>, 2020.
- [44] S. Keeler, M. Kimchi, and M. Peter J., *Advanced High-Strength Steels Application Guidelines*, vol. 06. WorldAutoSteel, 2017.
- [45] I. E. Benrabah, F. Bonnet, B. Denand, A. Deschamps, G. Geandier, and H. P. van Landeghem, “High-throughput compositional mapping of phase transformation kinetics in low-alloy steel,” *Appl Mater Today*, vol. 23, p. 100997, Jun. 2021, doi: 10.1016/J.APMT.2021.100997.

- [46] “‘Steel Purchase’ Website,” <https://steelpurchase.com/low-alloy-steel/>, 2022.
- [47] R. Singh, “Stresses, Shrinkage, and Distortion in Weldments,” *Applied Welding Engineering*, pp. 201–238, Jan. 2016, doi: 10.1016/B978-0-12-804176-5.00017-7.
- [48] Twi-global (Online, “<https://www.twi-global.com/technical-knowledge/faqs/faq-what-are-low-alloy-steels-and-what-precautions-should-i-take-when-welding-them/>,” 2022.
- [49] K. R. Krishna Murthy, F. Akyel, U. Reisgen, and S. Olschok, “Simulation of transient heat transfer and phase transformation in laser beam welding for low alloy steel and studying its influences on the welding residual stresses,” *Journal of Advanced Joining Processes*, vol. 5, p. 100080, Jun. 2022, doi: 10.1016/J.JAJP.2021.100080.
- [50] V. Igwemezie, M. Shamir, A. Mehmanparast, and S. Ganguly, “A review of LTT welding alloys for structural steels: Design, application and results,” *Journal of Advanced Joining Processes*, vol. 5. Elsevier B.V., Jun. 01, 2022. doi: 10.1016/j.jajp.2022.100110.
- [51] T. Fedina, J. Sundqvist, J. Powell, and A. F. H. Kaplan, “A comparative study of water and gas atomized low alloy steel powders for additive manufacturing,” *Addit Manuf*, vol. 36, p. 101675, Dec. 2020, doi: 10.1016/J.ADDMA.2020.101675.
- [52] X. Kang, S. Dong, H. Wang, S. Yan, X. Liu, and H. Ren, “Effect of Thermal Cycle on Microstructure Evolution and Mechanical Properties of Selective Laser Melted Low-Alloy Steel”, doi: 10.3390/ma12213625.
- [53] Y. Lee, M. Nordin, S. S. Babu, and D. F. Farson, “Effect of fluid convection on dendrite arm spacing in laser deposition,” *Metallurgical and Materials Transactions B: Process Metallurgy and Materials Processing Science*, vol. 45, no. 4, pp. 1520–1529, 2014, doi: 10.1007/s11663-014-0054-7.
- [54] F. Liu *et al.*, “Effect of microstructure on the Charpy impact properties of directed energy deposition 300M steel,” *Addit Manuf*, vol. 29, Oct. 2019, doi: 10.1016/j.addma.2019.100795.
- [55] H. K. D. H. Bhadeshia, D. v Edmonds, and D. V. E. Research, “The Bainite Transformation in a Silicon Steel,” 1979.
- [56] H. Kitahara, R. Ueji, N. Tsuji, and Y. Minamino, “Crystallographic features of lath martensite in low-carbon steel,” *Acta Mater*, vol. 54, no. 5, pp. 1279–1288, Mar. 2006, doi: 10.1016/J.ACTAMAT.2005.11.001.
- [57] F. Liu *et al.*, “Effect of isothermal temperature on bainite transformation, microstructure and mechanical properties of LSFed 300M steel,” *Mater Today Commun*, vol. 25, p. 101452, Dec. 2020, doi: 10.1016/J.MTCOMM.2020.101452.
- [58] J. Saewe, N. Carstensen, P. Kürsteiner, E. A. Jäggle, and J. H. Schleifenbaum, “Influence of increased carbon content on the processability of high-speed steel HS6-5-3-8 by laser powder bed fusion,” *Addit Manuf*, vol. 46, p. 102125, Oct. 2021, doi: 10.1016/J.ADDMA.2021.102125.
- [59] T. Maurizi Enrici, A. Mertens, M. Sinnaeve, and J. T. Tchuindjang, “Elucidation of the solidification sequence of a complex graphitic HSS alloy under a combined approach of DTA and EBSD analyses,” *J Therm Anal Calorim*, vol. 141, no. 3, pp. 1075–1089, Aug. 2020, doi: 10.1007/s10973-019-09093-9.
- [60] Aconity Website, “<https://aconity3d.com/products/aconity-midi/>.”
- [61] H. Jia, H. Sun, H. Wang, Y. Wu, and H. Wang, “Scanning strategy in selective laser melting (SLM): a review,” *International Journal of Advanced Manufacturing Technology*, vol. 113, no. 9–10. Springer Science and Business Media Deutschland GmbH, pp. 2413–2435, Apr. 01, 2021. doi: 10.1007/s00170-021-06810-3.
- [62] knowledge and service, Struers. Metallographic products, “<https://www.struers.com/>.”
- [63] Olympus Global Website, “<http://www.olympus-global.com/en/>.”
- [64] Tescan Website, “<https://www.tescan.com/tescan-clara-new-field-free-uhr-sem/>.”
- [65] A. C. R. (2017). Alicona, “Alicona, Alicona Cobots Real3D, (2017).”
- [66] Micromeritics website, “<https://www.micromeritics.com/accupyc-ii>.”
- [67] NETZSCH Website, “[www.https://www.netzsch-thermal-analysis.com/en/](http://www.netzsch-thermal-analysis.com/en/)”.
- [68] M. Boccalini and H. Goldenstein, “Solidification of high speed steels,” *International Materials Reviews*, vol. 46, no. 2. pp. 92–115, 2001. doi: 10.1179/095066001101528411.
- [69] EMCO-TEST Hardness testing machines acc., “<https://www.emcotest.com/en/>.”
- [70] EDEN instruments Website, “[www.eden-instruments.com/en/nanoindentation-platforms/](http://www.eden-instruments.com/en/nanoindentation-platforms/).”
- [71] M. H. Mosallanejad *et al.*, “In-situ alloying of a fine grained fully equiaxed Ti-based alloy via electron beam powder bed fusion additive manufacturing process,” *Addit Manuf*, vol. 56, p. 102878, Aug. 2022, doi: 10.1016/J.ADDMA.2022.102878.

- [72] B. Song *et al.*, “Differences in microstructure and properties between selective laser melting and traditional manufacturing for fabrication of metal parts: A review,” *Front. Mech. Eng*, vol. 10, no. 2, pp. 111–125, 2015, doi: 10.1007/s11465-015-0341-2.
- [73] W. Hearn, K. Lindgren, J. Persson, and E. Hryha, “In situ tempering of martensite during laser powder bed fusion of Fe-0.45C steel,” *Materialia (Oxf)*, vol. 23, p. 101459, Jun. 2022, doi: 10.1016/J.MTLA.2022.101459.
- [74] E. Liverani, S. Toschi, L. Ceschini, and A. Fortunato, “Effect of selective laser melting (SLM) process parameters on microstructure and mechanical properties of 316L austenitic stainless steel,” *J Mater Process Technol*, vol. 249, pp. 255–263, Nov. 2017, doi: 10.1016/J.JMATPROTEC.2017.05.042.
- [75] C. Tan, K. Zhou, M. Kuang, W. Ma, and T. Kuang, “Science and Technology of Advanced Materials Microstructural characterization and properties of selective laser melted maraging steel with different build directions Microstructural characterization and properties of selective laser melted maraging steel with different build directions,” 2018, doi: 10.1080/14686996.2018.1527645.
- [76] R. Seede *et al.*, “Effect of heat treatments on the microstructure and mechanical properties of an ultra-high strength martensitic steel fabricated via laser powder bed fusion additive manufacturing,” *Addit Manuf*, vol. 47, p. 102255, Nov. 2021, doi: 10.1016/J.ADDMA.2021.102255.

# 9. ANNEX



**SANDVIK OSPREY LTD.,**

RED JACKET WORKS,  
MILLAND ROAD,  
NEATH SA11 1NJ,  
UNITED KINGDOM.

Telephone: 01639.634121  
Fax: 01639.630100  
E-Mail: powders.osprey@sandvik.com

S2 (X S2M)



## CERTIFICATE OF ANALYSIS: 32344

Revision: 1

<b>Customer:</b>	LIEGE UNIVERSITE		
<b>Customer Order:</b>	ULG20/1935072/R		
<b>Customer Alloy Name:</b>	S2		
<b>Osprey Order Number:</b>	201127/02	CALL:01	
<b>Osprey Alloy Name:</b>	S2		
<b>Dispatch Number:</b>	21D0265		
<b>Weight:</b>	50.10Kg	(110lb)	
<b>Powder Size:</b>	-45micron +10micron		
<b>Atomise Gas:</b>	Nitrogen		

Physical Test Data				Particle Size Data			Chemical Analysis(wt %)			
	Minimum	Actual	Maximum	Sieve Analysis			El	Minimum	Actual	Maximum
Tap Density, g/cc		5.00		+45µm 1.80%			Si	0.9	1.2 %	1.2
Hall Flow, s/50g		18.0	25.0	-45µm +10µm 98.20%			Mn	0.3	0.6 %	0.5
				-10µm 0.00%			Mo	0.3	0.6 %	0.6
							C	0.40	0.49 %	0.55
				<b>Laser Diffraction Analysis</b> Malvern 2000 Instrument			Ni	0.0	0.0	0.3
				Minimum Actual Maximum			V	0.0	0.0	0.5
				d10 µm	20.6		Fe	<b>BALANCE</b>		
				d50 µm	31.0					
				d90 µm	47.5					
				-10.0 µm = %						

